Breakup of liquid jets: the capillary retraction

Francesco Paolo Contò

PhD thesis

School of Engineering and Materials Science
Queen Mary University of London

Submitted in fulfilment of the requirements
of the Degree of Doctor of Philosophy

2019

To my family: Francesco, Lucia, Giovanni;
my grandparents, my aunt Franca, don Mauro.

«*Examples . . . which might be multiplied ad libitum, show how difficult it often is for an experimenter to interpret his results without the aid of mathematics.*»

John William Strutt, Lord Rayleigh (1842 - 1919)

Acknowledgements

I could not have succeeded in this research work and in my studies without the help and support of many people. I would like to say *thank you* to all of them. First of all, I thank my family for its fundamental and constant support during all the years of my life.

Many thanks go to my supervisor Dr J.Rafael Castrejón-Pita, who allowed me to live one of the most beautiful experiences in my life: three years in London, achieving a PhD at Queen Mary University. Here, I have met people from all over the world, discovering the universe of research and a very challenging and fascinating field. His precious experience and our discussions have been essential for the research management.

I thank my collaborators at Queen Mary, Dr Yi Sui and Dr Fan Wang, and prof. Alfonso Castrejón-Pita, who supervised my experiments at University of Oxford: their contribution was crucial for the success of this work. Thanks to my external tutors during my stay at Sorbonne Université in Paris, prof. Stéphane Popinet and prof. Arnaud Antkowiak: their experience and talent led me to expand my knowledge and skills. Thanks also to Alexis Berny, César Pairetti and Quentin Magdelaine for their help in computational modelling and for their clarifications at my several questions.

I want to thank prof. Leonardo Gordillo with deep gratitude: his continuous and very generous collaboration, during my stay at University of Santiago and not only, has led to the high quality of this work. Next, I would like to thank Dr Juan Marín for his kind cooperation.

Furthermore, I thank all people (colleagues and professors) I have met all over the world during these intense three years. Thanks to all the friends I have met, especially Orest, Dare and Miguel: with them I spent many nice and funny moments, fully enjoying my worldwide experience.

Finally, I want to thank all people I know, that somehow have crossed my path, those who love me. Living with you reminds me that in life there is more than science.

Declaration

I, FRANCESCO PAOLO CONTÒ, confirm that the research included within this thesis is my own work or that where it has been carried out in collaboration with, or supported by others, that this is duly acknowledged below and my contribution indicated. Previously published material is also acknowledged below.
I attest that I have exercised reasonable care to ensure that the work is original, and does not to the best of my knowledge break any UK law, infringe any third party's copyright or other Intellectual Property Right, or contain any confidential material.
I accept that the College has the right to use plagiarism detection software to check the electronic version of the thesis.
I confirm that this thesis has not been previously submitted for the award of a degree by this or any other university.
The copyright of this thesis rests with the author and no quotation from it or information derived from it may be published without the prior written consent of the author.

Details of collaboration and publications:

Dr Yi Sui and Dr Fan Wang performed the numerical simulations and equally contributed to develop the analytical model presented in chapter 3.
Prof. Leonardo Gordillo supervised the work described in chapter 4 in collaboration with Dr Juan Marín, and prof. Arnaud Antkowiak collaborated in the numerical simulations.
The work presented in chapter 3 was published in the "Journal of Fluid Mechanics" [1] and presented at the Special Interest Group "Drop Dynamics" Meeting at University of Oxford on December 14$^{\text{th}}$ 2017 and at the 71$^{\text{st}}$ Annual Meeting of the American Physical Society Division of Fluid Dynamics in Atlanta, GA (USA), on November 19$^{\text{th}}$ 2018 [2].
The work described in chapter 4 has been accepted for publication in "Scientific Reports" [3].
The present thesis was selected as finalist for the 17$^{\text{th}}$ ERCOFTAC "Reynolds Day" and presented at the University of Manchester on July 12$^{\text{th}}$ 2019, at the "UK Fluids Conference 2019" (University of Cambridge, 27-29 August 2019) and at the conference "Droplets 2019" (Durham University, 16-18 September 2019).

Signature: *Francesco Paolo Contò*
Date: *September 30th, 2019*

Publications

Journal articles

- Wang F., Contò F.P., Naz N., Castrejón-Pita J.R., Castrejón-Pita A.A., Bailey C.G., Wang W., Feng J.J., and Sui Y. A fate-alternating transitional regime in contracting liquid filaments. *Journal of Fluid Mechanics*, 860: 640-653, 2019.

- Contò F.P., Marín J.F., Antkowiak A., Castrejón Pita J.R., and Gordillo L. Shape of a recoiling liquid filament. *Scientific Reports*, 2019.

Conference proceedings

- Contò F.P., Wang F., Castrejón Pita J.R., Sui Y., and Castrejón-Pita A.A. A fate-alternating transitional regime in contracting liquid filaments. *Bulletin of the American Physical Society*, 2018.

Abstract

Why and how does a falling stream of fluid break up into droplets? It is well known that the major driving mechanism is the fluid surface tension, but other variables such as viscosity and environmental instabilities are also known to affect the breakup. In this thesis, the capillary retraction of liquid filaments is studied through experimental, theoretical and numerical methods.

Previous works have established that a liquid filament can either recoil into a single sphere or break up into multiple droplets. Its fate depends on the Ohnesorge number Oh, a parameter that measures the relative importance of viscous to capillary forces, and the initial size aspect ratio Γ (length/thickness). According to the state-of-the-art, a critical aspect ratio Γ_c should exist and depend on the Ohnesorge number, such that longer filaments break up and shorter ones collapse into a single drop. The results in this thesis demonstrate that the breakup/no-breakup boundary is complex and not as simple as originally proposed. A transitional regime exists in which there are multiple Γ_c thresholds: breakup and no-breakup behaviours alternate. These observations are explained through a model based on the interaction of capillary waves that originate at both ends of the filament and travel inwards along its surface.

Additionally, an asymptotic analysis is used to derive a long-time steady state expansion for the retracting filament profile. This analysis results in three distinct regions with different characteristic length and time scales: a growing spherical rim, a cylindrical section and an intermediate matching zone. The analytical model shows that capillary waves escape from the rim travelling on the fluid interface. The key critical values of the problem are discussed: conditions to form a neck between the rim and the cylindrical filament, its minimal thickness, the waves' asymptotic wavelength and decay length. Interestingly, the wavelength of the capillary ripples is found to be approximately 3.6 times the filament's radius at the inviscid limit. Finally, the theoretical model is verified by numerical simulations and past works obtaining a good agreement.

List of Figures

List of Symbols

A	wave amplitude
b	linearly superposed amplitude of two colliding waves
b_c	critical superposed trough amplitude
c	Taylor-Culick velocity
d	droplet diameter
g	gravitational acceleration
h	local filament radius
h_{min}	filament neck thickness
H	local mean curvature of a fluid interface
J_n	Bessel function of n^{th} order
k	capillary wavenumber
L	initial half-length of a liquid filament
p	pressure
P_i	i^{th} peak on a capillary wave
Q	flow rate
r	instantaneous local radius of a liquid filament
r_d	density ratio
r_v	viscosity ratio
R	initial radius of a liquid filament
R_d	tail droplet radius at the merging instant
R_b	spherical rim radius
R_1	local radius of axial curvature of a fluid interface
R_2	local radius of azimuthal curvature of a fluid interface
T	temperature
T_i	i^{th} trough on a capillary wave
t	time
t_b	breakup time scale
t_c	inertial-capillary time scale
t_m	merging time scale
t_v	viscous time scale

u_c	capillary velocity scale
u_r	radial velocity
u_z	axial velocity
w	distance between two consecutive droplets
z	axial position
Δu_g	velocity variation due to gravity
δ_s	Dirac delta function
ϵ	initial perturbation amplitude
Γ	initial aspect ratio of a liquid filament
Γ_c	critical initial aspect ratio of a liquid filament
κ	dimensionless wavenumber of a varicose perturbation
κ_{max}	dimensionless wavenumber of the fastest growing mode
ℓ	spatial decay length
λ	wavelength
μ	dynamic viscosity
ν	liquid kinematic viscosity
ϕ	velocity potential
ψ	stream function
ρ	density
σ	surface tension coefficient
ω	growth rate of the perturbation amplitude
ω_{max}	growth rate of the fastest growing mode
Bo	Bond number
Oh	Ohnesorge number
Re	Reynolds number
We	Weber number
$\boldsymbol{n}$	local unit normal vector
$\boldsymbol{t}$	local unit tangent vector
$\boldsymbol{u}$	velocity field
$\boldsymbol{\tau}$	fluid stress tensor

Contents

Chapter 1

Introduction

1.1 Motivation and aims

This thesis takes inspiration from an experimental apparatus developed to study the breakup of a liquid jet (the rig is presented in section 2.4).

In this work, a jet is defined as a collimated stream of matter having more or less columnar shape [4]. The science of liquid jets is an extremely active area in fluid dynamics research: jets have attracted our attention not only for their several practical aspects, but for their theoretical interest too. In fact, they are encountered in nature, in a large number of situations, spreading over a wide range of physical length scales, from subatomic to universe-size phenomena. Moreover, they are considered a typical paradigm for some key topics of physics and applied mathematics: for instance, liquid jets serve as a model for free-surface motion, hydrodynamic instabilities and singularity formation.

Drop formation arising from breakup of liquid jets is a very important process in a large variety of applications. Ink jet printing [5], nuclear fission [16] [17], DNA arraying [18], medical diagnostics [19], sprays [20], deposition of reagents on diagnostic strips [21] [22], automatic pipetting of fluids [23], manufacture of particles [24] and microcapsules [25] are just some examples of industrial processes and biological systems that rely on the formation of liquid drops from jet breakup [26]. However, beyond their practicality, jets are also extremely useful as a test to determine liquid physical properties, such as surface tension, density, viscosity or non-Newtonian rheology.

For all applications or academic studies, the recurrent questions are: will the jet break, and if so, how long will it take? How sensitive is the jet to the background physics? How do liquid properties affect the breakup process stages (separation between two droplets)? After breakup, how disperse in size will the fragments be? How can the size distribution be modified and controlled? [4]

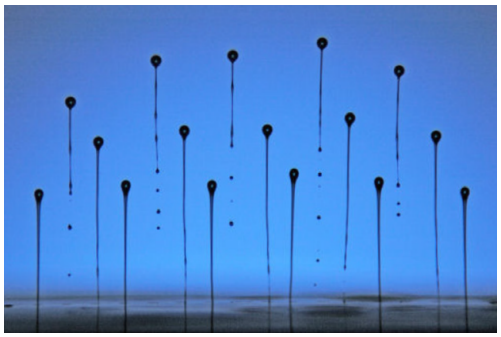

Figure 1.1: *Drops emerging from a bank of ink-jet nozzles. The image is about 2.3 mm across, the drop heads are 50 μm across and the tails are less than 10 μm wide. Picture taken from [4].*

Figure 1.2: *Left: A viscous thread (honey) falling downwards by its own weight. Right: a tap water jet falling into a sink. Photographs by Celeste Villermaux / Eggers-Villermaux (2008).*

Apart from these practical applications, drop breakup is of great theoretical as well as numerical interest due to the richness of the underlying physics and mathematics. The main challenge in the study of jets is to solve the phenomena governing equation, i.e. the full Navier-Stokes equation in the time-dependent fluid domain, subject to boundary conditions. Currently, one of the most important aims of this research area is to find an accurate mathematical model to describe the fluid boundary evolution.

The next section outlines the structure of the present thesis.

1.2 Thesis structure

The main contents of each chapter are presented below.

Chapter 2 provides a general overview of the field. After a historical summary of scientific developments, the current state-of-the-art is analysed from both theoretical and experimental perspectives: the main methods, techniques and challenges are described. The experimental apparatus that inspired all this research work is then presented together with a global work overview.

In chapter 3, the first important scientific contribution of this work is presented: an experimental and numerical investigation of an unexplored regime of capillary retracting liquid filaments. A simple analytical model is derived to validate our observations: travelling capillary waves are found to be responsible for the observed physical mechanisms.

Chapter 4 investigates the capillary recoiling of liquid filaments through mathematical modeling, by using stability and local asymptotic analysis techniques. The analytical model formally describes the evolving shape of the retracting liquid body in a long-time asymptotic steady regime, and it is validated against numerical simulations.

In chapter 5, the results of the whole study are summarised and ideas on possible further developments are highlighted.

Chapter 2

Background

2.1 History

The study of liquid jets likely started with Leonardo Da Vinci in the fifteenth century. His works represent the earliest stages in the exploration of jets behavior and breakup. In his *Codex Leicester* [27] Leonardo investigated the cohesion of fluids and its role for drops generation. He wrote:

"How water has tenacity in itself and cohesion between its particles. This is seen in the process of a drop becoming detached from the remainder, this remainder being stretched out as far as it can through the weight of the drop which is extending it; and after the drop has been severed from this mass the mass returns upwards with a movement contrary to the nature of heavy things".

Leonardo made a correct deduction: a drop falling from a tap detaches when gravity overcomes the cohesive (surface tension) forces of the liquid. However, he also incorrectly assumed that this same condition is necessary for the drop itself to separate.

The same problem was approached and further explored in the following years by other scientists. Mariotte [28] stated that gravity causes drop breakup, concluding that an upward jet cannot break up. He performed a quantitative analysis: assuming initial condition of zero speed, a falling jet reaches the free fall velocity $v = \sqrt{2gh}$ at a distance h from the nozzle. If Q is the flow rate, and considering a jet with a circular section, according to mass conservation, the radius r of the jet becomes increasingly thin as it falls (it decreases with h) [4]:

$$r = \left[\frac{Q}{\pi\sqrt{2gh}}\right]^{1/2} \tag{2.1}$$

Mariotte claimed (not very accurately) that breakup occurs when the fluid

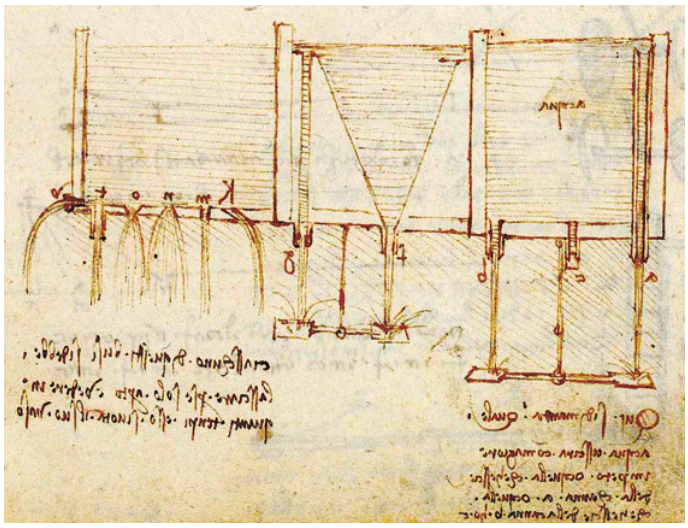

Figure 2.1: *"What water will pour with the greatest violence, that from the nozzle a, b, or c?". Leonardo da Vinci's question and the drawing reproduced from the Codex. - National Library of Spain.*

thread has become as "thin as a hair".

In summary, both Leonardo and Mariotte noted a certain tensile strength σ on the surface of water. They asserted that this is provided by cohesive forces, and the breakup condition for a jet is that the tensile strength has to be overcome by gravity. However, this simple model did not reflect the real physics, giving completely unrealistic predictions.

The solution of this problem appeared in the scientific community the following century: in 1805-1806 Laplace and Young published their famous works [29] [30], establishing the Young-Laplace equation:

$$\Delta p = 2\sigma H = \sigma \left(\frac{1}{R_1} + \frac{1}{R_2} \right), \tag{2.2}$$

where Δp is the pressure difference across the fluid interface, σ is the surface tension, H is the mean curvature, and R_1 and R_2 are the principal radii of curvature. The equation describes the capillary pressure difference sustained across the interface between two static fluids (such as water and air) due to the surface tension.

With their work, Young and Laplace exhibited the crucial role of the *mean curvature*. They stated that the curvature of the fluid interface consists of two different contributions, one axial and the other radial. Thus, surface tension can act in two different ways. This is the subtle and key point which explains the failure of previous theories and clarifies the breakup dynamics. For a hanging drop, the axial curvature makes surface tension act like an elastic membrane; but

once a cylindrical shape is reached, the radial curvature promotes the breakup. The system tends to the configuration with the smallest surface area, i.e. a smaller jet radius that goes to zero in the final pinch-off point. Hence, paradoxically, the greater the cohesion between the particles (and thus the surface tension σ), the faster breakup occurs [4].

Neglecting the fluid viscosity, dimensional analysis (see Buckingham theorem or Rayleigh's method) provides us with a characteristic timescale of the motion:

$$t_c = \left[\frac{\rho r_0^3}{\sigma}\right]^{1/2}, \tag{2.3}$$

where r_0 is the initial radius of the cylinder of liquid. As r_0 decreases, the motion accelerates (the characteristic timescale decreases). Moreover, it can be estimated that the jet radius r decreases in time according to the proportionality $\frac{dr}{dt} \propto r^{-1/2}$. Integrating this differential equation, it can be proved that the radius r goes to zero in a finite time with a characteristic exponent of $2/3$. The time t_c is the estimate of the total time for breakup to occur [4].

After Laplace and Young's fundamental contributions to the field, a further step was needed to achieve a complete mathematical description of jet breakup: combining the understood and fixed effects of surface tension with the classical laws of fluid dynamics. The first (experimental) progress was performed by Savart [31]. He noted that breakup occurs spontaneously, regardless of any external forces acting on the fluid or the jet motion direction. These observations established that breakup is an intrinsic feature of jet dynamics. The main finding of Savart's experiments was the detection of a smaller "satellite" drop between two main ones in the jet. This feature can be explained with the non-linear stages of jet breakup dynamics, as confirmed by later theoretical studies.

The first attempts to formally understand the dynamics of the breakup of continuous liquid jets were made by Rayleigh [32] [33] [34] and Plateau [35] in the nineteenth century. Plateau's work eventually gave surface energy (or surface tension) a key importance in terms of jet breakup process [4]: a jet is proved to be unstable to any perturbation which reduces its surface area. He experimentally observed the decay of columns of fluid in density-matched surroundings (then named "Plateau tank"). His main effort was focused on the unstable modes of breakup: he proved the existence of a characteristic perturbation *wavelength*, λ_{opt}, corresponding to a resonance frequency. In particular, Plateau stated that perturbations are unstable if their wavelength, λ, is greater than a critical threshold, λ_{cr}, whose value equals $\lambda_{cr} = 2\pi r_0 \approx 6.28 r_0$, and this was demonstrated explicitly and rigorously. However, this "optimal" wavelength, λ_{opt}, was deduced from Savart's measurements to be $\lambda_{opt} = 8.76 r_0$, relatively much higher than his "perfectly rigorous" $2\pi r_0$.

Later, Rayleigh was able to explain this "overestimation" [4] by considering that the jet physics chooses only the wavelength with the fastest growth rate among all the unstable ones ($\lambda > \lambda_{cr}$). Neglecting the jet viscosity, this estimate provides $\lambda_{opt} = 9.01 r_0$: a result that matches very well Savart's observations (occurred about 50 years earlier). The main Rayleigh's contribution was to consider the real jet dynamics. In fact, he can be considered the father of linear stability analysis in jet breakup theory, an extremely powerful analytical method that is still used nowadays.

When perturbations are no longer small, non-linear effects become dominant, and they lead to the jet breakup. These final nonlinear stages of jet dynamics were further explored by other scientists in new experiments, more and more sophisticated (Savart in 1833, then Magnus [36] and Lenard [37]).

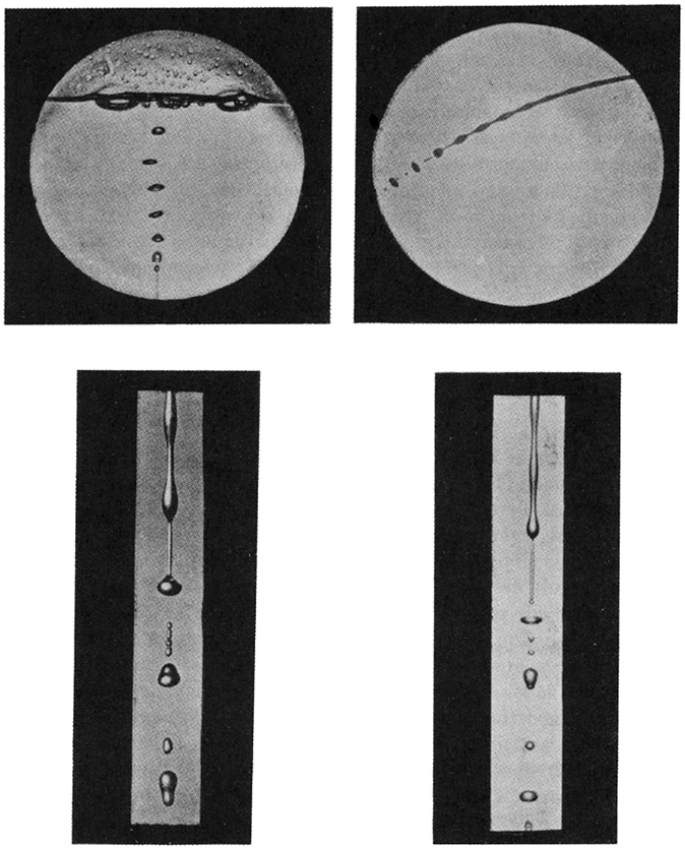

Figure 2.2: *Rayleigh's "some applications of photography" (1891) in the destabilization of a jet of air into water (top left) and of a water jet in air (top right). Bottom images: Details of the breakup process and the contraction of "ligaments" between the drops, sometimes breaking up before recoiling. Picture taken from [4].*

Later studies and experiments outlined this key feature of the breakup process: the profile has a standard shape, which is very asymmetric in most conditions. The breakup behavior has a universal nature independently on the boundary and initial conditions (such as the characteristic length scale - i.e. nozzle diameter - and the particular stimulation of the jet) [38]. Approaching the breakup condition, the jet profiles have been observed to be self-similar, regardless of any characteristic length scale of the phenomenon. Universal laws and features have been developed (from studies based on dimensional analysis) or simply observed to describe some characteristic jet parameters. A common example is the conically shaped neck: in case of low viscosity, it is predicted to have an opening half-angle of 18.1° [39]. Another typical result is the power law describing the temporal evolution of the minimum thread radius: $r_{min} = 0.7(\sigma(t_0 - t)^2/\rho)^{1/3}$ [39]. Here, t_0 represents the breakup time, ρ and σ being the density and the surface tension of the fluid, respectively. In general, self-similarity is often observed in experiments. For this reason, many works have tried to establish the complex features of drop breakup within a theoretical description based on scaling/universal laws, aimed at describing especially the non-linear aspects of free-surface flows.

Recently, many groups have continued to develop theories and to conduct experimental investigations to study the process of breakup of liquids and the creation of droplets. However, jet and droplet dynamics are still very open topics: the majority of predictive models are not fully validated yet or they are not precise. Because of this inaccuracy, industrial companies can do only a limited use of most numerical methods. Experimentally, several techniques (for instance, high-speed digital cinematography) have facilitated the study of jets. Thanks to current technology, microscopic fluid dynamics details of the breakup phenomenon can be detected in real time: this is extremely important as it provides us with a reliable source of data for comparison with theoretical studies [4]. However, these experimental efforts have been seriously limited by the global technological level, as well as numerical simulations have been hampered by computational power, time and cost [6]. In summary, although many studies have contributed to the understanding of droplet creation and evolution, unsolved problems (both theoretical and experimental) still remain, most of them surrounding the breakup regime which is widely used in the production of droplets for industrial and biological applications as well as for academic interests.

In the next sections, an overview of the state-of-the-art is provided from both theoretical and experimental perspectives.

2.2 Theoretical framework

Several analytical and numerical studies describing free-surface flows have been developed by scientists: a comprehensive review of these methods can be found for instance in [40]. As already mentioned in the introduction, the physics of liquid jets offers a large variety of mathematical aspects to investigate: singularities, instabilities, asymptotics, non-linearity, self-similarity.

A key feature of a liquid jet is its mean curvature: indeed, it determines the strength of the boundary force acting on the fluid domain. The most important driving force of jet dynamics is the Laplace pressure, i.e. the pressure jump across a curved interface, producing an increased pressure inside a convex surface. When the jet radius goes to zero (approaching the breakup), its curvature (and forcing) goes to infinity: this is a typical example that exhibits occurrence of mathematical singularities in jet breakup modeling [4]. In particular, this is known as the "pinch-off" singularity of free-surface flows (flows with an exposed surface) and it is the main complication when dealing with the dynamics of fluid surfaces [39]. The singularity appears in the Navier-Stokes equation as the jet diameter vanishes asymptotically at the pinch-off point. Up to the point of breakup, the dynamics of fluids are described as a continuous medium (standard N-S equation), but, theoretically, the breakup is described as a singularity. As a consequence, most of the theoretical models only study asymptotic behaviors, usually disregarding transitional aspects [6].

Another interesting mathematical aspect arising from the study of liquid jets and breakup is self-similarity. The dynamics both spatially and temporally exhibits self-similar behavior due to the large (orders of magnitude) disparity between local and corresponding global scales.

From an analytical perspective, a basic tool used in the study of liquid jets is the linear stability analysis around the cylindrical base state. However, the breakup process is characterized by some key stages in which non-linear effects are dominant and drive the dynamics. In particular, the final steps of breakup are extremely non-linear and are often tackled by using scale invariance. Numerically, there are still very hard and unsolved issues: current simulation codes are not able to reproduce the complex geometry of a jet because of its many degrees of freedom. Thus, studies are usually focused on very small and detailed individual breakup phenomena. Consequently, very high resolutions are often required [4].

2.3 Experimental framework

Recently, industrial and commercial interest on non-contact deposition techniques of liquids have caused an important rise in studies of jets dynamics and drop generation mechanisms [41]. In this field, the most widespread application is in inkjet printing technology. The current state-of-the-art promotes research in droplets' physics aiming to get important technological improvements: a typical example is in the control of the size, position, number, and motion of drops and their satellites [42]. In fact, the dynamics (speed, direction) of main drops and satellite droplets are crucial factors for printing quality and efficiency. Because of this industrial demand from inkjet companies and its business implications, the study of droplets arising from jets breakup is currently a topic of considerable relevance.

Improving the understanding of droplet dynamics and jet breakup through simulations (required to be more and more precise) is a fundamental condition to reach higher standards in terms of resolution, quality, speed and materials. Because of their accuracy, numerical and theoretical models are usually exploited to investigate in detail ink fluid properties, nozzle design, actuation mechanisms and their complex interactions. However, experimental validation is always the further necessary step [41].

It is very complicated to run experiments in commercial inkjet printers since droplets have very small size ($d \approx 50$ μm) and high speeds ($v \approx$ 5-20 m/s). Moreover, in most cases commercial systems are designed to work only within a limited range of jetting parameters, not allowing the user to tune them. Furthermore, the nozzle design and its geometry are usually fixed. The size of the drops depends on the nozzle diameter, that is often on a scale of tens of micrometers; for this reason it is extremely difficult or even impossible to modify its geometry to explore the shape influence. In this perspective (parametric study of jet and drops dynamics), a large-scale model system can be a valid solution as it overcomes many of these disadvantages. The millimeter length scale allows to easily alter the nozzle design, achieving excellent accuracy in geometry; the driving signals can be adapted or altered as well. Finally, the system can be tuned to work in the same fluid-mechanical regime as real inkjet printers by properly choosing the fluid properties. In summary, a proper use of the experimental setup (in terms of parameters' values) makes it possible to get comparable results not only with other large-scale systems, but also with commercial micrometer-scale inkjet printers, which typically operate in the same fluid-dynamics regimes [42].

To provide with a more precise and comprehensive definition, experimental studies of jet breakup can be classified into three different categories [41]:

- micrometer-scale experiments performed with commercial devices;
- millimeter-scale experiments operating in the same fluid-dynamics regime of commercial jet actuators (fluid properties are chosen to get the same dimensionless parameters);
- experiments run in different fluid-dynamical regimes with respect to commercial printers.

The first set is usually very complicated to run as in this case the user cannot measure directly many of the involved jetting parameters. Generally, the characteristics of commercial droplet actuators (physical dimensions, speed and size of their jets) do not allow the use of pressure transducers, thermocouples, and velocimetry techniques such as Laser Doppler Anemometry (LDA) or Particle Image Velocimetry (PIV). Hence, these experiments are carried out just to analyze "macroscopic" measurements (i.e. externally observable parameters such as droplet size, speed, breakup lengths). On the contrary, millimeter-scale systems can involve the direct measurement of the flow, pressure, and even velocity profiles; however, they may be unable to reproduce exactly the same dimensionless parameters of their commercial counterparts (e.g., gravity plays a major role in the millimeter-scale systems because of longer characteristic times). Finally, the last category of experiments may provide ideal conditions for further analysis of the involved variables. These studies may be relevant not only for scientific purposes (understanding of jets behavior and their breakup), but also for industrial reasons: indeed, they may be used to investigate possible new and unexplored jetting regions [41].

In the next subsections, the experimental state-of-the-art is analysed in detail: different techniques of jets generation, visualization and measurement are presented.

2.3.1 Jets generation

Fluid jets can be produced by a variety of actuation mechanisms. Droplets are usually jetted through an electric signal driving a piezoelectric or a heating element inside a printhead. These actuators can either produce the jetting pressure, or promote the breakup of a continuous jet. Progress in the understanding of jetting and drop formation phenomena has mostly focused on the driving electric signal. This is usually identified by an applied voltage as a function of time. The shape of its graph is often referred as "wave form" and is characterized by some key-properties such as amplitude and frequency. However, few efforts have been made in the investigation of the more fundamental drivers of these processes, i.e. the pressure and velocity waves [41].

Two different groups of techniques are commonly used in the printing industry, depending on the particular purpose. The main difference consists of the periodicity in droplets generation. ***Drop on demand DoD*** technology produces drops intermittently in response to a digital signal; while ***continuous jetting CIJ*** technique breaks up a liquid jet into a continuous stream of drops, then steered electrostatically for specific purposes (to achieve desired printing effects). As already mentioned, these techniques produce drops through different methods. *DoD* printing usually exploits a discrete pressure pulse to eject drops from a nozzle (a piezoelectric actuator is often used to generate the pulse). On the other hand, a continuous inkjet *CIJ* process typically applies a harmonic modulating disturbance to the flowing jet. *DOD* printers are mainly used for multiple-color printing, often for office and domestic purposes. In contrast, *CIJ* printing is generally intended for industrial production, i.e. date coding and labeling [41].

CIJ printing is commonly intended for uniform-sized droplets production. In these systems, an oscillating pressure modulation is applied to the fluid: this stimulation excites instabilities and makes the continuous liquid jet break up into a series of droplets. In this process, the liquid properties, the modulation frequency, the nozzle size, and the pressure at the nozzle plane are crucial parameters for the dynamics: in fact, they affect the position, velocity, size, and mutual distance of the drops (given a steady breakup condition). Two different methods are used for the breakup induction: a piezoelectric actuator is commonly adopted to produce the breakup of flows jetted from nozzles with diameters of tens of micrometers, whereas vibrating bellows play this role for larger applications [41] [42]. When applications require large amounts of monocolored prints, commercial CIJ systems are the typical solution. Moreover, continuous jets are ideal for high speed printing applications as drops production takes place at higher frequencies compared to drop-on-demand tools with the same size. Continuous inkjet technology is constantly evolving, and printing processes based on this method are currently used in several applications: the most common one is the expiration date printed on food and drink packaging [42]. A CIJ printer usually consists of three main components: a single nozzle, a periodic actuator, and a deflection system for jetted droplets. From the commercial point of view, a CIJ system is characterized by the breakup curve, which provides the distance from the nozzle to the appearance of the discontinuity in the liquid column [43] as a function of the excitation voltage at a given excitation frequency. This curve determines the industrial efficiency of the commercial setup. Nowadays, CIJ predictive modeling is mainly focused on the jet breakup length in order to optimize the dynamics of droplets and their satellites. Most studies in this field aim to increase quality, resolution and adaptability of printing processes. On

the other hand, some efforts are being made to develop innovative and advanced applications in different sectors such as biotechnology and electronics. However, the common ground for all such studies lies in seeking to better understand the governing laws behind the formation, evolution, and breakup of continuous jets into droplets [41].

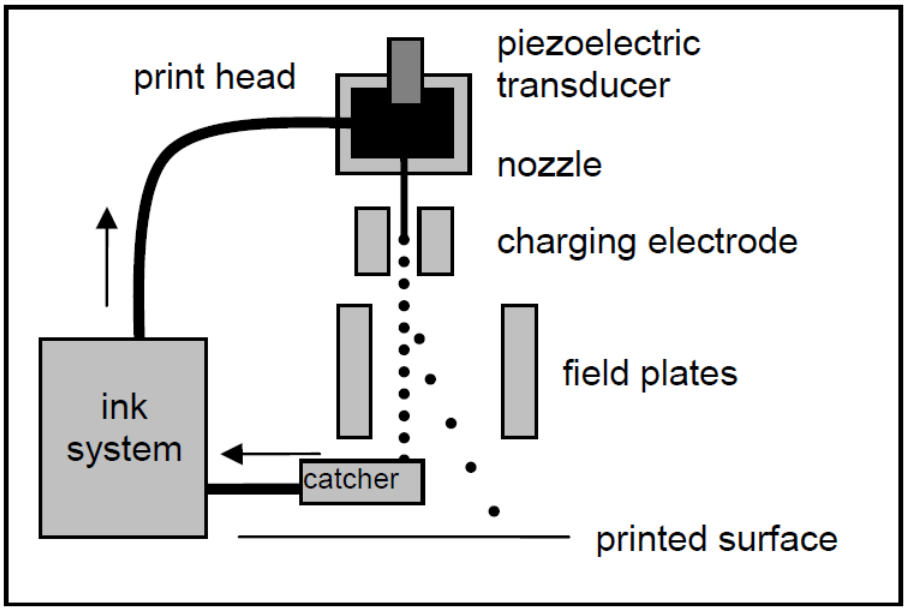

Figure 2.3: *Schematic diagram of a continuous inkjet printing system, taken from [5].*

Drop on demand generators are commonly used with piezoelectric ceramics, but some alternatives have been developed using pneumatic DoD generators running with fast-acting solenoid valves [42]. In order to satisfy scientific and industrial requirements, DoD systems must run a safe and reproducible droplets generation. They must include an actuator for a quick and reliable production of pressure pulses in order to generate controlled liquid jets. Moreover, they need a control system for controlling the liquid meniscus level with respect to the nozzle position. Further devices are required for additional functions affecting the system performance: for instance, the actuator generating an arbitrary number of pressure pulses to control the number and size of satellite drops. Depending on the particular application, commercial inkjet printers adopt several different methods of droplets production. However, only two general types of waveform are used: single peak and double peak. Rise-fall times and pulses durations are mostly determined empirically, matching the specific fluid and the desired jetting parameters. Regardless of the particular way to produce the pressure pulse, its duration and amplitude (together with the number of

generated pulses) determine the droplet velocity and its volume [41] [42].

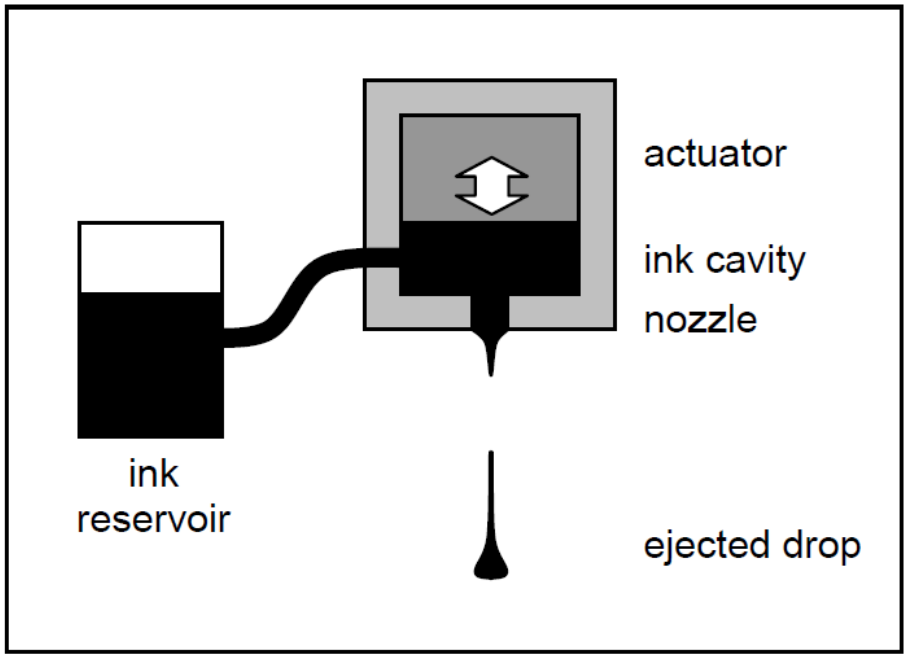

Figure 2.4: *Schematic diagram of a drop-on-demand printing system, taken from [5].*

Finally, it is evident that CIJ and DoD technologies face different problems: DoD systems are often focused on the control of the meniscus level, whereas CIJ mode deals with challenges regarding the way to maintain the liquid pressure as uniform as possible. Generally, CIJ systems work over a wider region of jetting parameters because drops can reach faster speeds than in DoD. Moreover, CIJ printing is more flexible as it has a simpler actuator driver, the meniscus control is not required, and it consists of fewer components. These advantages make its operating range wider than DoD prototypes' [42].

2.3.2 Visualization and measurement

To overcome the difficulties arising from theoretical and numerical modelling, the majority of research studies on liquid jets and droplets have recently focused their efforts on developing experimental systems able to visualize and measure the following physical processes: drop generation, pinch-off, breakup, coalescence, mixing and splashing. This approach aims to build a solid experimental platform as a validation of both numerical and theoretical methods [6].

Nowadays, many experiments make use of high-speed imaging. This technique has an intrinsic limitation: spatial and temporal resolutions are inversely

proportional to each other. This means that high-speed cameras can either visualize high resolutions at low speeds or vice versa (very fast but low resolution). However, the study of droplets dynamics often requires both high-temporal and high-spatial resolutions (study of very small features at very high speeds) to be fully analyzed: this is a fundamental issue in experimental studies [6]. Technological advances in visualization are trying to overcome this limitation, allowing better observations and more accurate measurements: new generation sensors, faster computational power, higher speeds of processing are just some examples of the recent experimental modeling evolution in the field of droplet dynamics; however, a substantial validation work is still required [6]. Current studies make use of a large set of technologies in this subject. In fact, traditional photography, high-speed imaging, holography and other several experimental techniques may all be adopted to study droplets and jets dynamics.

It is important to underline that these techniques are just visualization methods, thus they are often not enough to provide the user with quantitative values. For measurement purposes they need to be coupled with **image analysis** or similar tools in order to get measurable data. Only this approach can lead to appropriate scientific analysis and proper comparisons with theoretical/numerical models [6].

A basic visualization strategy is ***shadowgraphy***. This technology has been pioneering and has strongly influenced the research in drop dynamics. This method has been used in the present work. The basic architecture of a shadowgraph setup is represented in the scheme of figure 2.5. Shadowgraphy technique places the object of study between a light source and a detection tool, that is usually a camera or a charge-coupled device (CCD). As regards illumination, the system is usually composed of two elements: an optical diffuser and a light condenser. The latter works as a collector: it captures most of the light emitted by the source and forwards it to the diffuser in order to generate a background that is uniform. Indeed, in image analysis, a sharp contrast of colors is required between the objects under investigation and the background. For this reason, optical distances between the components (condenser and diffuser) are extremely crucial for the system efficiency and the quality of post-analysis process [6].

Like every existing technology, shadowgraphy has pros and cons for any particular application. A positive aspect is that it uses most of the light produced by the source and the quite definite contrast obtained between objects and the background. A high contrast is a fundamental requirement in image analysis as it allows to precisely identify fluid and/or object boundaries. Moreover, lightening efficiency is often a key parameter for such systems, especially with low-sensitivity detectors and cameras. In contrast, shadowgraphy offers a significant disadvantage as it can detect only objects' "shadows", thus it cannot

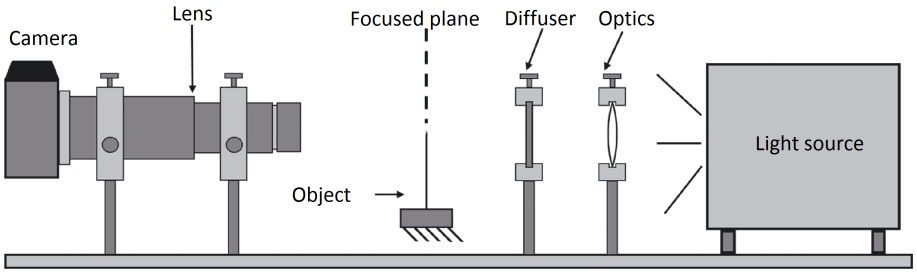

Figure 2.5: *Basic scheme of a shadowgraph setup [6].*

differentiate multiple colors and/or small optical properties or different fluids. Hence, this technique does not allow the study of chemical-fluid dynamics phenomena in which multiple fluids are involved (for instance, droplet mixing). In fact, the no distinction between different liquids implies the exclusion of important physical information and represents the main problem of shadowgraphy [6]. As a result, shadowgraphy should be ideal to use under these conditions: rapid phenomena requiring high recording speeds (i.e. low characteristic timescales, short exposure times, low light conditions, low-sensitivity sensors); multi-phase systems with substantial differences in refractive indexes and optical properties. A typical example is the study of drops dynamics in the air [6].

Some other applications require the use of color imaging. In experiments, to differentiate colours, the light source is located at the front of the object under investigation, and not at its back as in shadowgraphy. In such systems, the condenser and/or diffuser reflect the light emitted by the source, not dissipating it away. However, this arrangement allows to exploit just a portion of the global light because of the capacity of color cameras. Indeed, colour studies commonly have a lower sensitivity (usually one third) compared to the correspondent monochrome devices. That is the reason why scientists make use of color imaging technique only when illumination is extremely intense and/or with long exposure time conditions. Despite this main disadvantage, color imaging method is very powerful and widely used: its typical application lies in the field of reactive inkjet. In such context, droplet experiments are run to monitor the progress of a chemical reaction: for this purpose, indicators or reactive inks are often injected into the fluid [6].

In general, high-speed and single-frame imaging techniques need to be paired with very specialized tools; in fact, such applications often require high-intensity light sources or fast flashes. Of course there are several alternative possibilities to investigate drop dynamics; obviously, each method has advantages and disadvantages depending on the specific purpose [6]. Some of these options are briefly presented below.

- ***Strobe illumination***: This method allows to perform a detailed physical analysis of the jetting dynamics as it can acquire accurate droplet images. Its main advantage is that the implementation of droplet and jet visualization is quite inexpensive; moreover, image analysis can be performed through a real-time process. On the other hand, the method has also a disadvantage related to the speed of the imaging process: in contrast to high-speed imaging systems, this technology cannot detect phenomena characterized by very fast time scales (drop by drop variations in the jet behavior is a typical example) [6].

- ***Holography***: It is a valid alternative option which can deal with some of the problems arising from conventional methods, such as: two-dimensionality, very small field of view and depth of field, inaccuracy, optical distorsions. In particular, this technique is very suitable for a simultaneous detection of many drops: if matched with appropriate tools and imaging processes, it can provide with very high accuracy (order of submicron) in position and size measurements, even over a field of view of the order of centimeters [6].

- ***Confocal microscopy***: This technique is typically suited to the analysis of drop generation in a fast moving jet. Such systems require the synchronization between a pulsing illumination and the drop formation (frequency of modulation). Nowadays technological progress is providing this method with important advances and improvements in both sensors and cameras, as well as in the imaging process (in terms of speed and resolution). It has been proved that a confocal microscope has a lateral resolution 30% better than a conventional one; the objective lens usually reaches a submicron resolution. Currently, confocal microscopy is being widely adopted in the study of liquid microjet instability [6].

Above, only some general features have been listed; major details about these visualization techniques and their architectures can be found in [6].

As regards the quantitative measurement process of droplet dynamics phenomena visualized through the above techniques, a commonly used method (adopted in this work) is the ***binary image analysis***. This is explained below.

Most of the research in droplet dynamics makes use of image analysis in order to visualize and compute droplets' positions, profiles, sizes and motion. This information is often extracted from binary images recorded by a CCD camera. Such images have eight-bit format pixels and are numerically characterized by a gray-scale value (intensity): this can lay from 0 to 255 and represents the

image brightness. In shadowgraphy conditions, a fluid droplet is visualized as a dark object on a lighter background: then in binary images, in terms of detection purposes, the pixels belonging to the fluid area should have a value of 1 and the background pixels should have a value of 0. Accordingly, the binary image conversion works as follows: the values greater than the threshold parameter (preset by the user) are turned into 0; similarly, the values lower than the threshold are turned into 1. It is evident that the choice of the threshold value is a key-step to get proper binary images and to obtain exact measurements (quantitative data on droplets). The threshold selection is based on the particular illumination conditions, so it is variable from case to case. Moreover, binary image conversion has an important advantage: when external objects are detected, or in presence of image noise, a morphology function can remove the undesired noise and suitably modify the image for a proper analysis [6].

The binary imaging process allows to detect and compute droplets' profiles and trajectories, as well as the jet speed. Hypothetically, also droplets' volumes might be estimated considering them as axisymmetric bodies; actually, the real physics seldom respects this assumption as fluid droplets often have irregular geometries characterized by extended filaments. Other crucial aspects related to the droplet volume detection regard some technical limits of the CCD camera. In fact, an accurate measurement is usually arduous because of its limited pixel resolution. Consequently, image sizes are often widely affected by critical parameters such as the system illumination features and the threshold value for the image conversion (gray-scale to binary) [6].

In the next section, the experimental setup and visualization techniques used for the present thesis work are presented.

2.4 Experiment

This section describes the experimental setup and the visualization and measurement techniques used in the present work.

2.4.1 Rig

The experimental apparatus, illustrated in figure 2.6, is a millimeter-scale system of a continuous inkjet printer. The flow is activated by a liquid pump; the jet flow rate is controllable and measurable by adjusting the pump operating voltage. The jet generator consists of a cylindrical chamber: its top side is closed by a flexible rubber membrane which is mechanically coupled to an electromagnetic actuator (permanent magnet shaker LDS V201); its lower side contains a nozzle ranging in diameter from 1 to 2 mm from which fluid is ejected. The electromagnetic actuator is used to modulate the jet through a periodical harmonic waveform which is controlled by a function generator. The pressure within the chamber is monitored by a transducer mounted on its side. The oscillating pressure modulation induces Rayleigh-Plateau instability along the jet surface and drives its breakup into a string of equally spaced droplets. Liquid ligaments are originated between droplets, as a secondary product of breakup.

Pure water and water-glycerol mixtures are used as fluid in order to analyze a wide range of Oh numbers: glycerol-water mixtures provide a good model system for Newtonian fluids as their viscosities can move in a wide range with only small variations in surface tension. Experiments are run at room temperature.

The jet is imaged by a high-speed camera Phantom V711 in shadowgraph mode: images are recorded after the jet emersion from the nozzle at a frame rate in the order of 10^5 frames per second with an exposure time in the order of 10 μs. The region of interest is illuminated from behind with a light consisting of a compact series of eight 10 W LEDs vertically aligned in the flow direction. Then the light passes through an optical diffuser that is interposed between the light source and the liquid jet. The camera is used with a Tamron AF90 macro lens or a Navitar 12x microscope head to cover an appropriate field of view. In general, very large fields of view and high framing speeds are needed to "follow" the jet dynamics. Recording parameters are fully controllable through the imaging software from Phantom: in this work, the image resolutions of the camera system are ranged from 10^1 to 10^2 pixels/mm.

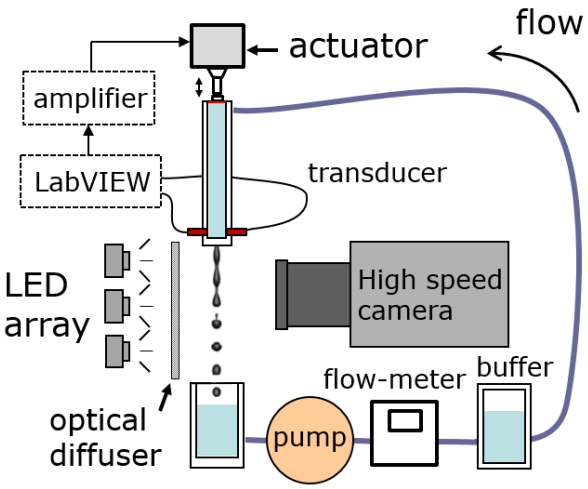

(a) *Scheme of the experimental setup.*

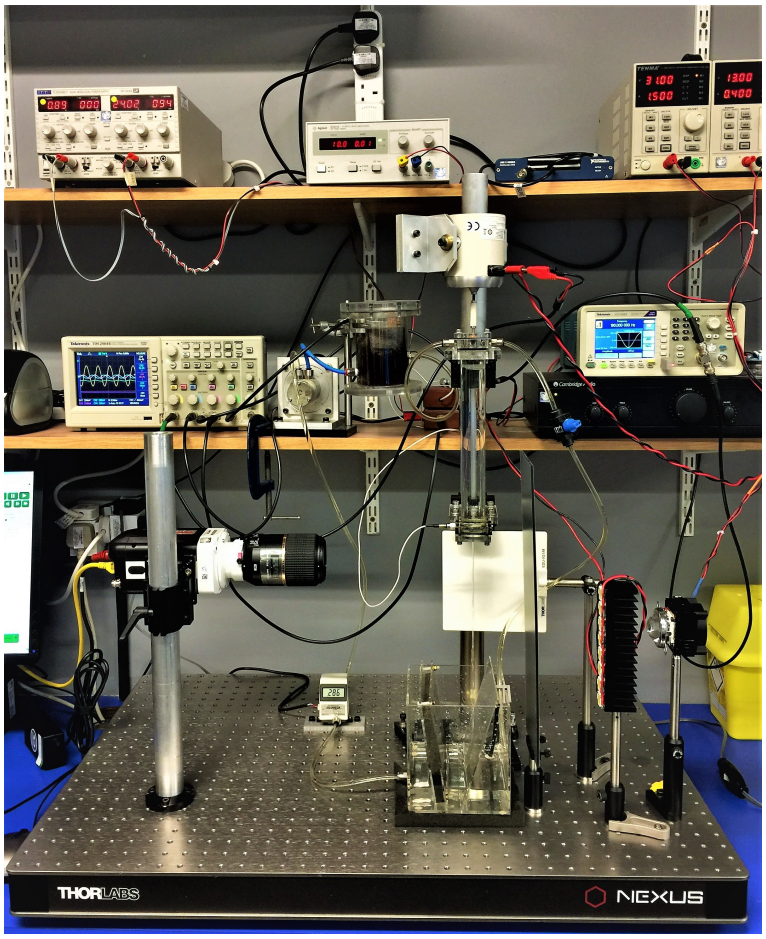

(b) *Photo of the rig.*

Figure 2.6: *The experimental apparatus.*

2.4.2 Post-analysis

As previously outlined, high speed imaging technique by itself does not provide measurable values, so it is usually coupled with a post-processing such as **image analysis** or other techniques to obtain quantitative data. This method permits appropriate comparisons and validations between experimental results and numerical/theoretical models. This is the approach followed in the present work.

Data analysis is performed through a binary imaging method with the software MATLAB®. This technique performs edge detection of elements (liquids or objects boundaries) through a threshold system in combination with high-speed imaging [6]. The first step of the algorithm consists in the digital scan of the picture acquired by the high-speed camera. MATLAB reads the raw picture and converts it into a gray-scale intensity image. Then a background subtraction is performed on the resulting image: the subtracted background image is a picture of the system without any object such as filaments, drops, liquid jets (also this image is previously turned from a true color RGB file into a gray-scale card). This operation between the two intensity maps aims to improve the analysis precision as it deletes intensity gradients in the background (due to the non-uniform lighting) and persistent and undesired elements (features unrelated to the physics being investigated). Once the gray-scale background-free image is obtained, it is then converted into a Black and White binary image. The intensity threshold for this conversion is the most crucial parameter of the whole image analysis process: it should be chosen with extreme caution (depending on the specific lighting and visualization conditions) in order to get a true representation of the observed object in the Black and White format [6]. Sometimes this algorithm requires a further step to remove image noise that can be detected as an actual boundary by the MATLAB script. This is the typical case of "bright spots": these "false" objects are generated by the reflections of the background light onto the camera sensors. This phenomenon is very common in observations of curved objects (drops, liquid filaments and jets). For this reason, an elimination of false objects is often needed. After its execution, the code extracts the boundary of the remaining object [6]. Once the code has effectively detected the boundaries of the object of interest, it is possible to process and analyze quantitative data that are necessary for the study of the physical phenomenon under consideration. Some of the key features are filament's diameter and length.

The next section clarifies the scientific insights provided by the experiment and outlines the objects of study of the present thesis.

2.5 Work outline

The overall aim of this work was to study the breakup of liquids as this mechanism drives droplet formation. As explained in chapter 1, several industrial techniques rely on the pinch-off of liquids to produce droplets, and from them, graphics and prints. In particular, inkjet printing drives a lot of fundamental research as industry constantly seeks ways to print faster or more reliably [5]. In fact, while exploring the existing literature, several open questions were identified, many of which within the field of CIJ. Specifically, the breakup dynamics seems to be related to challenging and unexplored problems. Firstly, we observed the so-called "reversal" effect. In a CIJ system, the dependence of the breakup length, i.e. the distance between the ejection section (nozzle) and the breakup point (the section at which the jet gets singular and breaks), on the jet-modulation amplitude is not fully understood yet. According to theory [43], the breakup length should decrease monotonically with the modulation amplitude (in terms of voltage, equivalent to pressure) applied to the capillary jet. However, experiments do not seem to match this prediction: they show that the breakup length decreases until a minimum stationary point corresponding to a critical amplitude, and then it goes through oscillations, as seen in figure 2.7. Nowadays, no accurate model exists to explain this trend and formally correlate the modulation signal to the jet dynamics. This is definitely a study worthy of further developments: it would be extremely interesting to investigate more deeply the underlying physics.

However, the present thesis is focused on the capillary retraction of the liquid filaments generated through the jet breakup. This is a classic fundamental problem extensively analyzed in the literature. The standard theoretical approach is to study the contraction dynamics of a free axisymmetric liquid body, a cylinder with two hemispherical caps with the same radius of the cylindrical section, initially at rest. These initial conditions, both geometric and kinematic, are very difficult to reproduce experimentally. Ideally, in order to originate such a filament from a continuous jet breakup, a symmetric and simultaneous detachment from the liquid column is needed at both caps of the body. Practically, this is not trivial at all: only some particular combinations of modulation parameters lead to this condition. In this regard, the so-called "inversion" phenomenon has been observed, that consists in different breakup dynamics depending on the signal modulating the jet. In particular, under certain conditions, the jet breaks up at the front of the filament being generated (this is called "front-pinching"); in other conditions, the jet breaks at the back of the filament ("back-pinching"). A qualitative trend of this dynamics is known in industry: the main tuning responsible is the jet modulation amplitude. Other conditions being equal, low

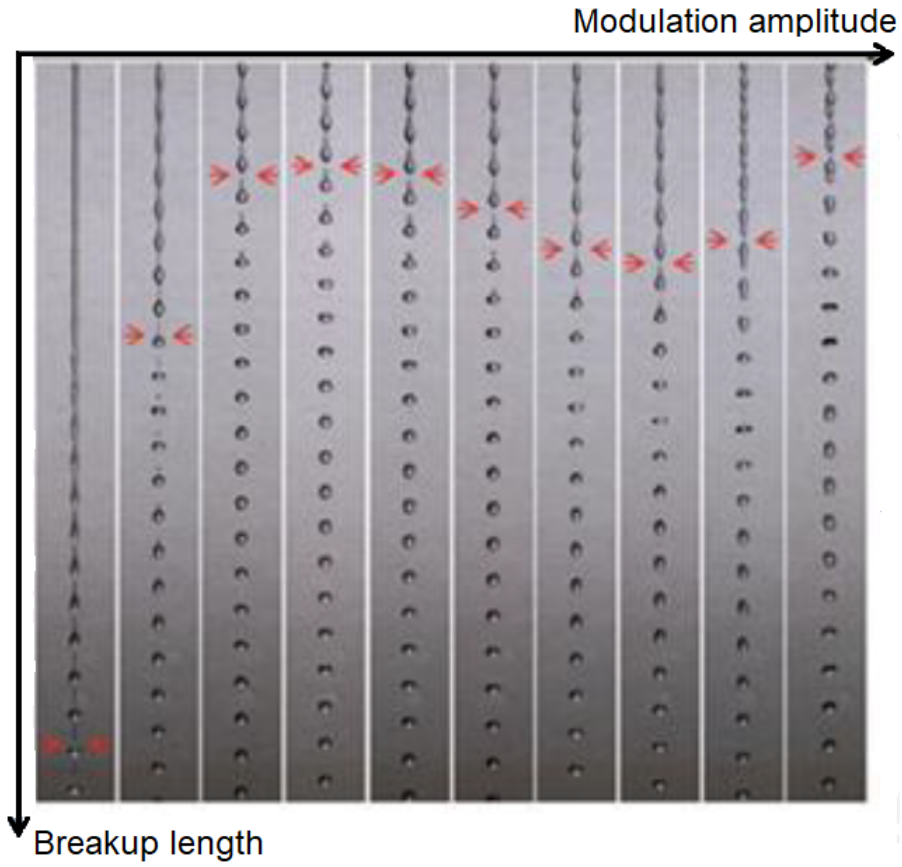

Figure 2.7: *Breakup length vs jet modulation amplitude.*

modulation amplitudes lead to front-pinching; on the contrary, large modulation amplitudes induce back-pinching. This phenomenon will be further discussed in the description of the adopted experimental method, in section 3.2 (see figure 3.7).

Our work specifically investigates the capillary retraction dynamics of liquid filaments, once they are free-standing in an outer gas (air). The space-time evolution of the filament is determined by the simultaneity of an axial shortening and a radial necking due to the surface tension of the fluid. The majority of published research on this topic shows through numerical simulations that the axial contraction is consistent with the Taylor-Culick model [44] [45]: the retraction speed seems to be constant and approximately equal to the value derived by Taylor and Culick, $u_c = \sqrt{\frac{\sigma}{\rho R}}$ (where σ is the surface tension of the fluid, ρ its density, and R the filament radius). Despite the complexity of the radial collapse, especially towards the pinch-off stage, Hoath *et al.* [46] use a simple model considering this process driven by viscous and surface forces.

According to them, the overall retraction is simply governed by independent rates of axial contraction and radial pinching: the resulting dynamics is the sum of these two separate "motions".

The present work exploits the accuracy of the experimental system capabilities, analytical and numerical tools to formally and fully investigate the retraction dynamics, going beyond the classic Taylor-Culick analysis and the simplistic models presented in the literature, such as the one described in [46]. The main purpose is to analyse in detail the surface-tension driven flows within the filament and along its surface. This study has led to two major achievements: a predictive model for the retracting filament fate (breakup in multiple droplets or collapse into a single drop), and an analytical description of the long-time asymptotic relaxation of the filament interface.

The next chapter is focused on the first important result of our research: the discovery of a transitional regime in capillary retracting liquid filaments.

Chapter 3

A fate-alternating transitional regime in contracting liquid filaments

It is well established that the fate of a contracting liquid filament depends on the Ohnesorge number (Oh) and the initial aspect ratio (Γ), apart from the initial surface perturbation. According to the state-of-the-art, there exists a critical aspect ratio $\Gamma_c(Oh)$ such that longer filaments break up and shorter ones recoil into a single drop [7].

In this chapter a transitional regime is reported after a computational and experimental analysis: our results show that in a broad window of intermediate aspect ratios, multiple Γ_c thresholds exist at which a novel breakup mode alternates with no-breakup. A very simple but effective model is developed considering the superposition of capillary waves travelling on the surface of the retracting filament. According to our model, the breakup results from the constructive interference between the capillary ripples that originate from both caps of the filament. The model can be used to produce a phase diagram showing the different fates of the filament within a detailed set of conditions.

3.1 Introduction

As discussed in chapter 2, paradoxically, cohesive forces of liquids (surface tension) are responsible for their breakup. A thread of liquid recoils also because of the action of surface tension [9] [10]. The physical explanation of the contracting motion is that surface tension forces act to minimize the surface energy, thus the fluid tends to a spherical body (the geometrical shape with lowest surface, given a certain volume). However, this simple contraction motion to a sphere does not always occur: in fact, liquid filaments may either recoil to one sphere or break into several pieces which will then recoil to spheres. This is the most common experiment in the study of liquid volumes relaxation. In fact, there is a wide set of experimental observations which shows filaments breaking up into separate parts while contracting [7].

Surface tension aims to reduce the total free surface of the fluid, thus it is the responsible for the evolution of a liquid volume with a given initial shape. The reason of the filament segmentation into several spheres is that surface tension time scale is very fast, and the decrease of the global surface by cutting the filament may be quicker than by compacting. Reducing area locally rather than globally may require to move less mass [10]. Even in the case of contraction with no breakup, the filament motion is a complex hydrodynamical process.

The dynamics of a capillary retracting liquid filament in another ambient fluid is a classic problem which has been widely analyzed throughout the years ([47], [48], [49], [9], [8], [10], [50]) because of its both fundamental and practical interest. In fact, it is involved in a broad variety of physical phenomena, both in nature and in industrial applications: ink-jet printing, spraying, microfluidics, particle technology are just some examples.

Several experimental, analytical and computational studies have focused on Newtonian cylindrical liquid filaments initially at rest, surrounded by a much less viscous ambient fluid: for this reason they are usually referred as "free filaments" [9]. The filament is considered as a cylinder of length $2L$ and radius R with two semi-spherical caps of radius R at both ends (see figure 3.1).

Following basic principles of dimensional analysis, all previous studies conclude that the fate of the filament is mainly controlled by two dimensionless parameters: the initial aspect ratio between the filament length and its diameter ($\Gamma = L/R$), and the Ohnesorge number $Oh = \frac{\mu}{\sqrt{\rho\sigma R}}$ (where μ and ρ represent the viscosity and density of the liquid, respectively, and σ is the liquid-gas surface tension coefficient), which measures the relative importance of viscous to capillary forces, i.e. the ratio between the viscous time scale $t_v = \frac{\mu R}{\sigma}$ and the inertial-capillary time scale $t_c = \sqrt{\frac{\rho R^3}{\sigma}}$. Rigorously, the filament dynamics depends also on any initial perturbation (shape and amplitude) on the filament

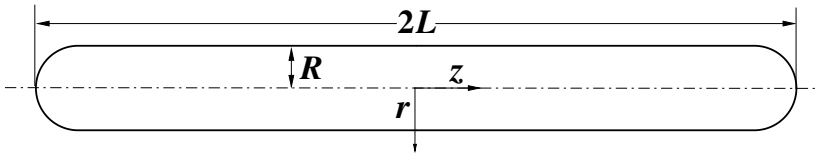

Figure 3.1: *Sketch of the initial geometry of a cylindrical liquid filament. The length of the filament is 2L and the radii of both the cylindrical section and the hemispherical caps are R. For analytical purposes, a cylindrical reference frame is defined with origin at the center of the filament.*

surface. Two surface tension competing processes occur at the same time: an axial shortening and a radial necking of the filament. The filament fate results into two possible behaviours: the breakup within the filament or the collapse into a single drop. In the literature, this phenomenon is typically analysed through the parametric plane $Oh - \Gamma$ (see figure 3.2). As a result, this space is divided in two main regions, breakup and no-breakup regimes. The border is a curve representing the critical aspect ratio as a function of the Ohnesorge number. In fact, previous studies have concluded that for each Ohnesorge number a critical initial aspect ratio value exists, below which the filament collapses into one drop, and above which it breaks in two or more droplets [7] [51].

Based on these results, it has been established that different viscosity regimes exist, with different characteristic times, speeds, scaling laws and breakup mechanisms. Very viscous filaments ($Oh \geq 1$) are always stable since viscosity effects are dominant; they collapse into a single drop regardless of the initial aspect ratio [9].

3.1.1 Rayleigh-Plateau instability

The stability of viscous long filaments ($Oh \geq 0.1$) is completely governed by the Rayleigh-Plateau theory [52] [32] [33] [51]: they break up mainly through the Rayleigh-Plateau mechanism. Liquid filaments can be considered as finite liquid jets, thus their dynamics can be described by the fluid columns of Savart [31]. In this study, Savart investigated the stability of liquid jets and he was the first one to observe the breakup of jets into multiple droplets. Plateau [52] claimed that breakup could be reached only with an unstable varicose perturbation acting on the jet surface: this is verified when the perturbation wavelength is larger than the jet diameter. Afterwards, Rayleigh [32] [33] analytically derived a dispersion relation for infinite inviscid jets. Rayleigh found out that the most unstable perturbation wavelength is approximately equal to $9R$, wavelength

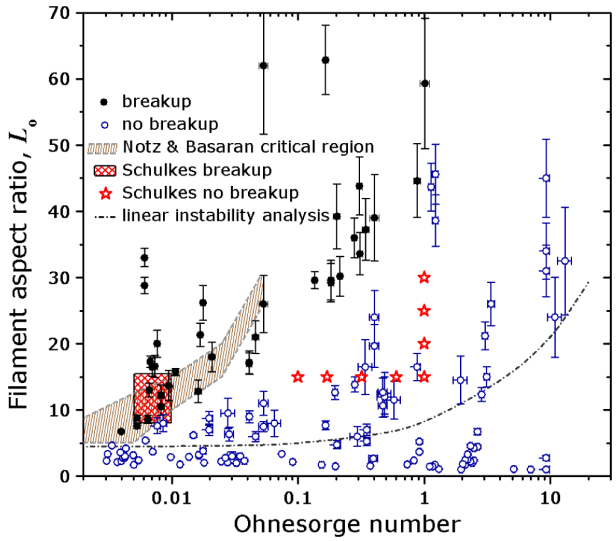

Figure 3.2: *Taken from [7]: filament fates plotted in the $Oh - \Gamma$ plane. Solid symbols represent filaments breaking up, and open symbols are filaments contracting into a single drop. The shaded area shows the predictions of the model of [8]. The hatched region represents the range of critical Oh predicted by [9]. Stars represent the points explored by Schulkes in which breakup does not occur. The broken line corresponds to the prediction of the linear instability analysis.*

corresponding to the perturbation which grows the fastest on a fluid column.

According to the classic Rayleigh-Plateau theory, a sinusoidal perturbation with a time dependent amplitude is assumed to act on the liquid interface. Thus, the local time-dependent filament radius can be expressed by:

$$r(z,t) = R + A(t)\cos\left(\kappa\frac{z}{R}\right), \tag{3.1}$$

where R is the unperturbed filament radius and $\kappa = \frac{2\pi R}{\lambda}$ is the dimensionless wavenumber of the varicose perturbation on the fluid cylinder (λ being the corresponding wavelength). In a linear perspective, the perturbation amplitude $A(t)$ has an exponential growth with respect to time of the form:

$$A(t) = \epsilon e^{\omega(t-t_0)}, \tag{3.2}$$

where ϵ is the perturbation amplitude at $t = t_0$ (i.e. the instant at which the filament pinches off from the jet and starts to retract), and ω is the growth rate of the perturbation amplitude. In this work we always assume $t_0 = 0$ s.

However, Savart [31] and Rayleigh [32] [33] studies had a major limitation: they only considered the asymptotic limit of inviscid liquids. After some years, Rayleigh [34] performed a complete analysis considering the effect of viscosity,

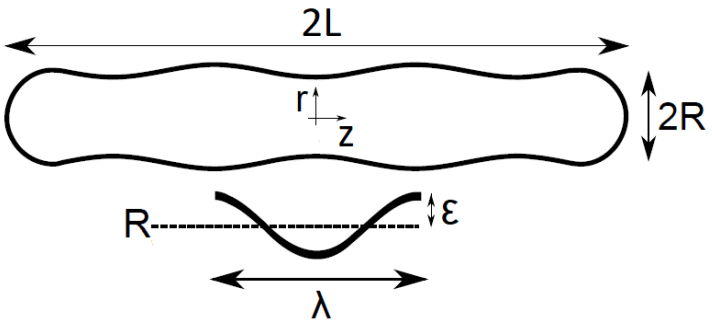

Figure 3.3: *Shape of the filament at $t = t_0$. The surface perturbation is assumed to be sinusoidal with wavelength λ and amplitude ϵ. The filament is considered axisymmetric with respect to the z axis.*

and derived the full dispersion relation for viscous jets. Its linearization, studied also by Weber [53], leads to the following growth rate of the viscous Rayleigh-Plateau instability:

$$\omega = \frac{\sqrt{\frac{1}{2}(\kappa^2 - \kappa^4) + \frac{9}{4}\mathrm{Oh}^2\kappa^4} - \frac{3}{2}\mathrm{Oh}\kappa^2}{t_c}, \tag{3.3}$$

where Oh is the Ohnesorge number, and t_c is the capillary time. The most unstable wavenumber (corresponding to the highest growth rate ω_{max}) results to be a function of the Ohnesorge number, this is:

$$\kappa_{max} = \frac{1}{\sqrt{2 + 3\sqrt{2}\mathrm{Oh}}}. \tag{3.4}$$

Therefore, the Rayleigh-Plateau instability is dominated by κ_{max}. By plugging its value in the dispersion relation 3.3, we can obtain the growth rate of the fastest growing mode ω_{max}. Analogously, this is a function of the Ohnesorge number. Consequently, the filament breaks when the growing perturbation reaches the value of the unperturbed jet radius: $A(t) = R$. Replacing the latter and $\omega = \omega_{max}$ in equation 3.2 (assuming $t_0 = 0$), the breakup time is derived as:

$$t_b = \frac{1}{\omega_{max}} \ln\left(\frac{R}{\epsilon}\right). \tag{3.5}$$

The critical aspect ratio (i.e. the aspect ratio above which the filament fragments due to the Rayleigh-Plateau instability) can be determined by comparing the Rayleigh-Plateau instability breakup time (equation 3.5) with the contraction time needed by the filament to collapse into a single drop. The retraction time depends on the retraction speed, which is derived through a momentum

balance. During filament retraction, blobs known as "tail droplets" originate at both tips of the filament. They grow in size by collecting the liquid mass from the cylinder, which stays stationary. Their typical velocity is analytically derived by balancing the momentum flux into the tail droplet and the capillary force acting on it (this derivation is formally provided in section 4.1). This is a classic result in the literature, obtained for the first time and independently by Taylor [44] and Culick [45] for liquid films: it is known as "capillary velocity", $u_c = \sqrt{\frac{\sigma}{\rho R}}$. The time needed by the filament tips to merge is called "merge time" [51]:

$$t_m = \frac{L - 2R_d}{u_c}, \tag{3.6}$$

where R_d is the tail droplet radius at the merging instant t_m.

The Rayleigh-Plateau instability produces a breakup of the filament only if $t_b < t_m$. In fact, the critical aspect ratio Γ_c is obtained by balancing the breakup time due to the Rayleigh-Plateau instability t_b (equation 3.5) and the merging time t_m (equation 3.6), and considering the filament mass conservation ($2\pi R^2 L = 2 \cdot \frac{4}{3}\pi R_d^3$) [51]:

$$\Gamma_c - (6\Gamma_c)^{1/3} - \frac{\ln(R/\epsilon)}{t_c \omega_{max}} = 0. \tag{3.7}$$

Thus, the critical aspect ratio Γ_c results to be a function of the only Ohnesorge number Oh (for a given initial perturbation amplitude ϵ).

3.1.2 End-pinching

The dynamics of low-viscosity ($Oh < 0.001$) filaments is basically inviscid. When breakup occurs, they usually fragment through the so-called end-pinching mechanism, which is a detachment of two bulbous ends from the filament tips. This dynamics is well described by Stone [48], Bentley and Leal [49] and Hoepffner [10]. In this regime, the action of surface tension forms a neck in the region connecting the tip to the central portion. The bulbous end eventually pinches off the cylindrical steady section. In inviscid filaments the radial necking is direct, i.e. the neck originates and its radius decreases monotonically towards the singularity, causing the breakup of the blob from the filament.

For slightly higher viscosities ($Oh \sim 0.01$), both viscosity and capillarity influence the filament dynamics. In this regime, the neck is formed, starts to decrease and then reopens escaping the breakup because of the formation of a vortex ring, a viscous effect. Eventually, this leads to end-pinching. The number of times the neck reopens before the breakup increases with the Ohnesorge number (see [10] and figure 3.4).

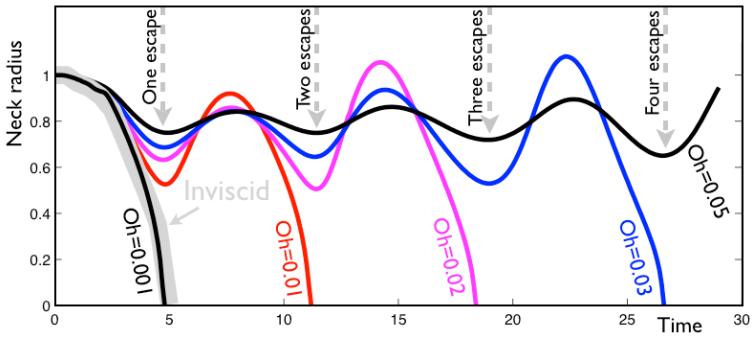

Figure 3.4: *Taken from [10]. Neck radius versus time for different Ohnesorge numbers (numerical simulations performed with the Gerris flow solver [11] [12]). At* $Oh = 0.001$ *the necking is direct [9]. At* $Oh = 0.01$ *one escape from pinching is observed; at* $Oh = 0.02$ *two escapes, and so on.*

Figure 3.5 reports a sketch of the filament end-pinching mechanism, which is well illustrated in [49] and [10]. In this figure, (a) the hemispherical shape of the filament tip with its convex curvature (curvature centre located inside the filament) produces a higher pressure than the steady cylindrical section because of the surface tension action (see Young-Laplace law, equation 2.2). The generated capillary pressure gradient induces a liquid mass flow from the tip towards the cylindrical region. (b) The retracting bulbous cap collects fluid mass from the cylinder, thus it grows in size developing a spherical shape. The interface connecting the rim and the cylindrical region forms a concave curvature (curvature centre located out of the filament). This corresponds to a pressure decrease at the minimum pressure P_{min} section. The negative pressure gradient induces a local backflow from the cylindrical section towards the rim. Therefore a neck is generated because of the local mass loss. (c) Just after the neck section, the interface curvature increases generating a positive capillary pressure gradient. A maximum pressure P_{max} is induced at the section connecting with the steady fluid cylinder. From this section a fluid flow generates towards both the spherical rim and the cylindrical region. (d) If the mass flow rate through the neck is sufficient, the necking reaches the singularity causing the direct breakup of the blob from the filament [49]; otherwise the neck escapes the pinch-off and reopens [10]. In the latter case, the necking process (b) and (c) will be repeated until end-pinching occurs (figure 3.4).

As mentioned in chapter 2, previous studies have effectively reported that for low-viscous filaments ($Oh < 0.1$) a critical initial aspect ratio Γ_c exists below which a filament fully contracts into a single drop and above which it fragments through end-pinching mode [8]. Even in this regime Γ_c is a function of the Ohnesorge number Oh, and is significantly smaller than the critical aspect ratio

related to Rayleigh-Plateau instability in the viscous regime [51]. Experiments performed by Castrejón-Pita *et al.* in 2012 [7] validated all previous studies on the critical aspect ratio Γ_c in an extended Oh range: in fact, figure 3.2 gathers all numerical and experimental data on this problem from the literature.

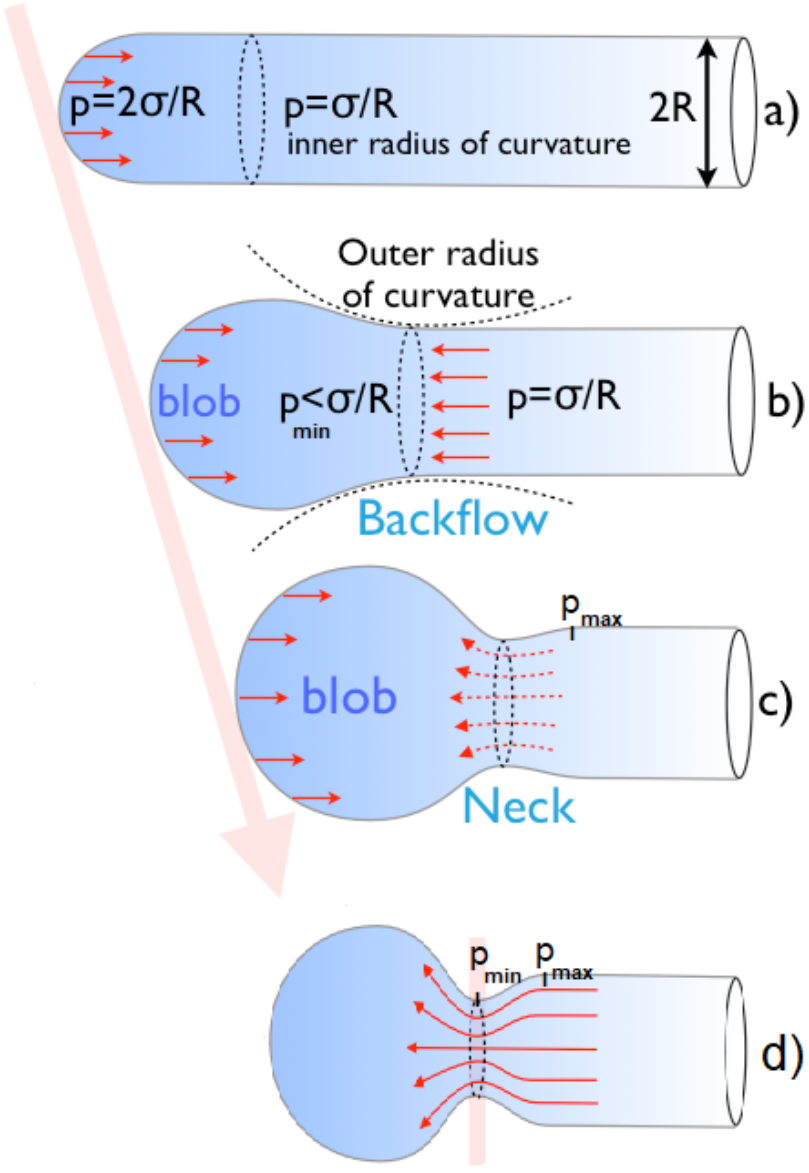

Figure 3.5: *Schematic time sequence of end-pinching dynamics [10].*

3.1.3 Restabilisation

However, Notz and Basaran [8] observed a so-defined "critical region" in the $Oh - \Gamma$ plane, located in the low-viscosity regime for a certain range of intermediate aspect ratios (see figure 3.2). In this region, filaments dynamics was not fully understood and just qualitatively explained. Some filaments, longer than the predicted critical length, do not breakup, undergoing through a stable full contraction. Also Tong and Wang in 2007 observed filaments breaking up into two or three droplets together with a transitional no-breakup mode (stable collapse into a single drop) for lengths larger than the critical one. This observation was reported in their numerical study [54]: by increasing the initial aspect ratio of low-viscous filaments, they detected different and undefined behaviors.

The no-breakup phenomenon occurring at $\Gamma > \Gamma_c$ is called "restabilisation". Indeed, it was first observed in 2001 in an experimental work by Ha and Leal [55], in which they analysed contracting liquid filaments suspended in a high-viscous outer liquid (polydimethylsiloxane). Afterwards, in 2007 Beaucourt et al. [56] reproduced numerically Ha and Leal's [55] experiment, detecting the previously observed "restabilisation". However, this phenomenon was not mentioned in recent classical works on the capillary retraction of liquid free filaments [8] [51]. Therefore, it is still unknown whether this dynamics is universal or only found in specific geometrical or physical conditions (cylindrical filaments with semi-spherical caps [54] or high-viscosity outer fluids [55], for instance). Ultimately, the underlying physics of "restabilised" liquid filaments has never been reported.

In the present work, we computationally and experimentally investigate the classic capillary retraction of Newtonian liquid filaments suspended in an inviscid ambient fluid. The main purpose of this study is to deeply analyze the "critical region" seen in figure 3.2, i.e. finite-length filaments ($4 \leq \Gamma \leq 50$) with low viscosity ($0.003 \leq Oh \leq 0.04$). In particular, we aim to understand and model the physical mechanisms that govern filaments dynamics in this particular critical domain. Our final target is to build a comprehensive phase diagram $Oh - \Gamma$ detecting all possible filament fates and pointing out the corresponding underlying physics.

3.2 Experimental method

The experimental setup has already been described in chapter 2, section 2.4 (see figure 2.6). Liquid filaments are generated between droplets pinching-off from a jet, as shown in figure 3.6.

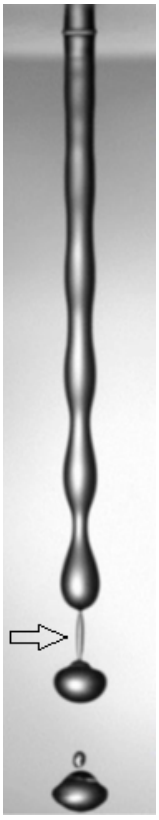

Figure 3.6: *The liquid jet is modulated by an electromagnetic actuator, driven by a harmonic waveform. The harmonic modulation breaks the jet by driving Rayleigh-Plateau instability on its surface. A filament (indicated by the arrow) is formed between two consecutive droplets.*

In the present work the jet speed u ranges from 1.1 to 1.9 m/s. Given a jet speed, the length of the filament is controlled through the actuation frequency ν of the harmonic modulation. In fact, the distance between two consecutive droplets, w, is given by: $w = u/\nu$.

The production of "ideal" filaments presents experimental difficulties known in industry. Inducing a simultaneous filament pinch-off from the jet at both caps is not trivial: only some particular combinations of modulation parameters lead to this condition. In this regard, the major control is given by the modulation amplitude of the waveform sent by the actuator. A qualitative trend of this dy-

namics is shown in figure 3.7. Low modulation amplitudes lead the jet to break up at the front of the filament first: this is normally called "front-pinching". In contrast, large modulation amplitudes break the jet at the back of the filament first, and this is known as "back- pinching". Symmetric filaments are obtained by carefully adjusting the modulation amplitude of the waveform in order to induce pinch-off at both ends simultaneously.

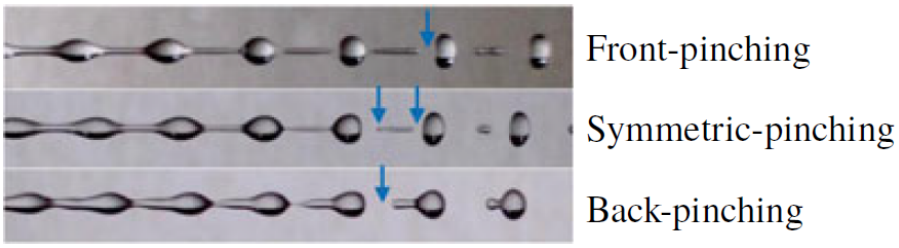

Figure 3.7: *Three different pinching modes in filaments formation.*

Figure 3.8 shows an example of such a symmetric pinching.

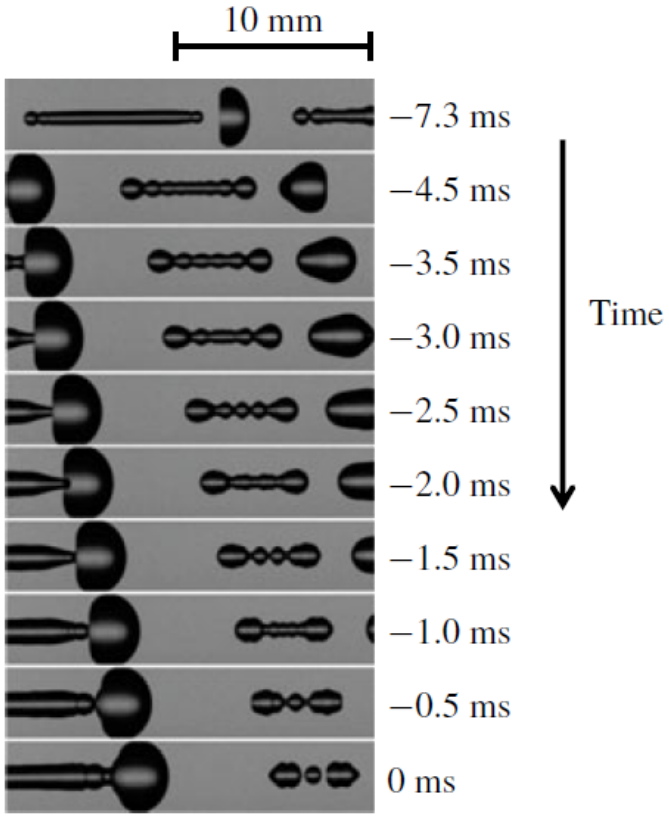

Figure 3.8: *Symmetric pinching: jet and filament evolution in time.*

The radius of the filament is hardly controllable: generally, it depends on the modulation frequency (i.e. filament length), however it is also clearly affected by the amplitude of the modulation signal. This control is complex: desired radii are usually obtained through "trial and error" experimental adjustments.

This work contains experiments run at room temperature using pure water as fluid. The filament radius R ranges from 0.15 mm to 0.75 mm (data are obtained through direct measurements on experimental high-speed images). This range corresponds to $0.004 < Oh < 0.01$. The experimental recording speed is of 20,000 frames per second, and the exposure time of the camera system equals 30 μs. The lens image resolution ranges from 12 to 32 pixels/mm.

Like all experimental data, these results are affected by error. First, the measurements of the fluid properties (density, viscosity, surface tension) provided by our devices are affected by the inaccuracy and imprecision of the tools themselves and by the errors of the measuring process. However, neglecting the influence of such (almost irrelevant) experimental uncertainties, our data mainly contain uncertainties arising from the measurements carried out on the imaging system. In fact, the parameters Oh and Γ are computed from the manually measured initial filament length and diameter (clearly smaller than the nozzle diameter). Uncertainties in these two measurements are responsible for the largest error contributions to the Oh and Γ.

In general, given a function f that depends on n uncertain variables x_i, and being these variables uncorrelated (like in our case, as $2L$ and $D = 2R$ are independent on each other), the function f will be affected by an error depending on the errors Δx_i of the n variables. In particular:
If $f = f(x_1, x_2, ..., x_n)$ with $x_1 = \bar{x_1} \pm \Delta x_1, x_2 = \bar{x_2} \pm \Delta x_2, ..., x_n = \bar{x_n} \pm \Delta x_n$ n uncertain uncorrelated variables (where $\bar{x_n}$ is the mean and Δx_n is the uncertainty associated with the variable x_n), then: $f = \bar{f} \pm \Delta f$, where $\bar{f} = f(\bar{x_1}, \bar{x_2}, ..., \bar{x_n})$ and the error $\Delta f = \left(\sum_{i=1}^{n} \left(\frac{\partial f}{\partial x_i} \Delta x_i \right)^2 \right)^{1/2}$.
In our particular case, the involved functions are the aspect ratio $\Gamma = \frac{2L}{D}$ and the Ohnesorge number $Oh = \frac{\mu}{\sqrt{\rho \sigma R}}$, where $2L$ and D are affected by uncertainty.
$\Gamma = \frac{2L}{D}$, where $2L = \bar{2L} \pm \Delta(2L)$ and $D = \bar{D} \pm \Delta D$. Thus $\Gamma = \bar{\Gamma} \pm \Delta\Gamma$, where $\bar{\Gamma} = \frac{\bar{2L}}{\bar{D}}$ and $\Delta\Gamma = \sqrt{\left(\frac{\partial \Gamma}{\partial (2L)} \Delta(2L) \right)^2 + \left(\frac{\partial \Gamma}{\partial D} \Delta D \right)^2} = \sqrt{\left(\frac{\Delta(2L)}{\bar{D}} \right)^2 + \left(\bar{\Gamma} \frac{\Delta D}{\bar{D}} \right)^2}$.
In the same way, $Oh = \frac{\mu}{\sqrt{\rho \sigma R}}$, where $R = \bar{R} \pm \Delta R$ with $\bar{R} = \frac{\bar{D}}{2}$ and $\Delta R = \frac{\Delta D}{2}$.
Thus $Oh = \bar{Oh} \pm \Delta Oh$, where $\bar{Oh} = \frac{\mu}{\sqrt{\rho \sigma \bar{R}}}$ and $\Delta Oh = \sqrt{\left(\frac{\partial Oh}{\partial R} \Delta R \right)^2} = \frac{1}{2} \bar{Oh} \frac{\Delta R}{\bar{R}}$.

The uncertainties $\Delta(2L)$ and ΔD arise from the manual measurements taken on the images captured by the high speed camera, thus they depend on the

particular picture. They always equal ± 1 pixel (the minimum measurable length unit in a picture), that corresponds to a specific metric length according to the image resolution. In general they are of $\mathcal{O}(10^{-2})$, giving rise to uncertainties $\Delta\Gamma$ and ΔOh not exceeding that order of magnitude.

Regardless of this quantitative analysis of the error, it is worth pointing out that every experiment in the $Oh - \Gamma$ plane is not a single point, but rather a range, a point centered on error bars, arising from uncertainties in the filament size measurements.

3.3 Computational method

Our numerical simulations consider free axisymmetric filaments consisting of a cylinder with two hemispherical caps, as illustrated in the scheme 3.1. The longitudinal length of the filament is $2L$ and the radii of both the cylindrical section and the semi-spherical tips are R. The initial aspect ratio Γ of the filament is defined as the ratio of half its length L to its initial radius R: $\Gamma = L/R$. The same geometry has been applied as initial condition in recent classical numerical studies of retracting liquid filaments [8] [9] [51]. A cylindrical reference frame is defined: its origin is set at the centre of mass of the filament. The computational domain is a rectangular box centered in the origin and containing the whole fluid interface. The problem is assumed to be axisymmetric (independent on the azimuthal coordinate) with respect to both z and r axes. Thus only a quarter of the filament is simulated: symmetric boundary conditions are imposed at $r = 0$ and $z = 0$. Moreover, on the other two boundaries of the box, a zero normal gradient of the velocity is set as boundary condition. The filament is surrounded by a quiescent and isothermal fluid domain whose density and viscosity are constant and negligible. Both the filament liquid (with constant density ρ_L and viscosity μ_L) and the surrounding gas (with density ρ_G and viscosity μ_G) are defined as Newtonian and incompressible, so the Navier-Stokes equations govern their dynamics. The surface tension coefficient is σ. As regards the setting of initial conditions, both the filament and the ambient fluids are assumed initially at rest: the velocity field is set zero in the whole domain. The used numerical code is non-dimensional: the inertial-capillary time $t_c = \sqrt{\frac{\rho_L R^3}{\sigma}}$ and the radius R are set as characteristic time and length scales. Therefore, the characteristic velocity can be derived as $v = R/t_c$: this is the capillary velocity $u_c = \sqrt{\frac{\sigma}{\rho_L R}}$. Input parameters of the numerical simulations are: the filament geometry (initial aspect ratio Γ); its Ohnesorge number $Oh = \frac{\mu_L}{\sqrt{\rho_L \sigma R}}$ (which results to be the reciprocal of the Reynolds number $Re = \frac{\rho_L v R}{\mu_L}$, given the characteristic capillary velocity - $Oh = Re^{-1}$); the viscosity and density ratios between the filament

liquid and the ambient fluid, $r_v = \mu_L/\mu_G$ and $r_d = \rho_L/\rho_G$ respectively. Our numerical simulations do not consider gravity (see section 3.4).

A level-set method by Sussman *et al.* [57] and Russo & Smereka [58] is used to capture the fluid interface. This method has been well established and its validity has been well tested by Spelt [59] and Ding & Spelt [60]. The code used in the present study was developed by Sui & Spelt [61] [62]. Our numerical simulations solve the Navier-Stokes equations by the standard projection procedure using a finite volume method on a staggered grid, the marker-and-cell (MAC) mesh. Velocity components are defined at cell faces whereas scalar variables such as pressure and volume fraction are defined at the cell centres. A fifth-order weighted essentially non-oscillatory (WENO) scheme [63] is employed for the level-set function using the local flow velocity as the upwinding direction. A structured and block-based adaptive mesh refinement (AMR) tool developed for parallel computing is adopted. The computational domain is covered with a hierarchy of grid blocks having the identical logical structure ($m \times n$ mesh). The refining and coarsening of the grid blocks are based on a simple check: if the maximum distance of the grid block to the interface is smaller than a critical value, a block is cut into two in all directions, respectively, producing eight (in our 3D axisymmetric configuration) children at a higher refinement level. Each of these has an identical logical structure, but the grid spacing in each direction is half that of its parent. All mesh blocks have the same logic structure at all levels of refinement. More details regarding the numerical method and performance test can be found in [59] and [64].

Mesh resolution and domain size effects on the solution have been checked in order to ensure that the reported results are independent on any possible increase of the mesh density or modification of the computational domain extent. In particular, different mesh refinements have been adopted for several Ohnesorge numbers to monitor mass conservation and solution convergence. A mesh resolution of $R/32$ results to be sufficient to fully detect the retracting filament dynamics. Therefore, this mesh size is used in the present study. After a study of the solution dependence on the domain size, the side of the rectangular domain in the z direction has been set to $4L$ (twice the filament length). The optimal domain height (rectangle side along r-axis) is dependent on the initial aspect ratio of the filament: $4R$ has been employed in the range $\Gamma \leq 16$, $5R$ for $16 < \Gamma \leq 22$, and $6R$ for $22 < \Gamma \leq 50$. The performed tests ensure that by increasing the domain size in both directions the simulation results remain substantially unchanged. The presented numerical method has been validated against simulations of retracting filaments available in the literature in terms of profiles time evolution. In particular, data from Notz and Basaran [8] were taken as a reference.

Our analysis is limited to nearly inviscid filaments (i.e. the range $0.003 < Oh < 0.02$) due to limitations on the numerical model. Numerical solutions get increasingly unstable by decreasing the Ohnesorge number in the range $Oh < 0.003$. On the other hand, for $Oh > 0.02$, very high aspect ratios (typically $\Gamma \gg 50$) are required to reach the breakup. This would correspond to much longer computational times; and it is worth pointing out that in the viscous regime also the computational time increases considerably with the Ohnesorge number. All the simulations performed for the present thesis are characterized by a run time ranging from 10 to 100 hours on a standard processor.

3.4 Validation

Among all the performed experimental tests and numerical simulations, two cases have been chosen to show the comparison between experimental and numerical results. These are shown in figures 3.9 and 3.10.

In the first experiment, the liquid is pure water at temperature $T = 22°C$; the viscosity is $\mu_L = 0.9$ mPa·s, the density is $\rho_L = 998$ Kg/m^3 and the surface tension equals $\sigma = 0.0718$ N/m. The outer fluid is air at room temperature. The viscosity and density ratios are set to $r_v = 50$ and $r_d = 1000$, resembling a liquid water filament suspended in air. A filament with $Oh = 0.01$ and initial aspect ratio $\Gamma = 8.6$ is chosen. Figure 3.9 shows the time evolution of the retracting filament profile. Dimensionless times (with respect to the inertial-capillary time scale t_c) for the snapshots are: $t = 4$, $t = 9$ and $t = 13$ in sequence. The red line is the extracted interface from high-speed experimental images, whereas the yellow contour is derived from the corresponding numerical simulation. Taking into account the experimental measurement error due to the images resolution and the inevitable asymmetries in the geometry of the real generated filament, a good agreement can be noticed between experiment and simulation.

The second test case reproduces the capillary retraction of a liquid filament with $Oh = 0.013$ and initial aspect ratio $\Gamma = 9.6$. The used liquid is a water-glycerol mixture (with a very low glycerol concentration) whose temperature equals $T = 23.5°C$; the viscosity is $\mu_L = 1.90$ mPa·s, the density is $\rho_L = 1057$ Kg/m^3, and the surface tension is $\sigma = 0.071$ N/m. Figure 3.10 shows the filament retraction motion: dimensionless times (with respect to the inertial-capillary time scale t_c) for the snapshots are $t = 0.796$, $t = 1.989$, $t = 3.183$ and $t = 5.17$ in sequence. The red boundary is extracted from experimental snapshots, while the green line is the interface contour obtained from the corresponding numerical simulation. Given the aforementioned inevitable discrepancies between experimental and numerical conditions, also in this case a good matching is achieved.

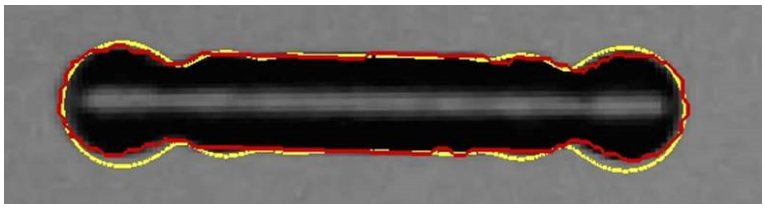

(a) $t = 4$

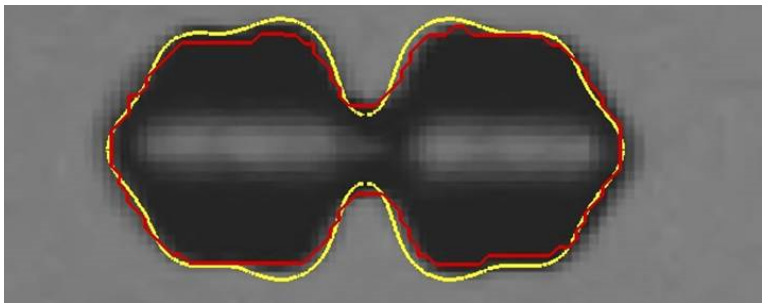

(b) $t = 9$

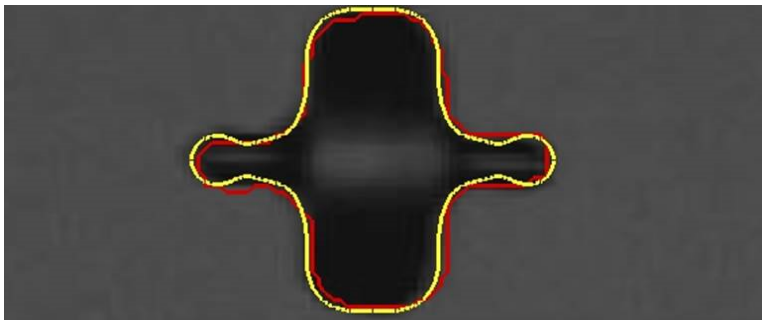

(c) $t = 13$

Figure 3.9: *Temporal evolution of a retracting filament profile with* $Oh = 0.01$ *and initial aspect ratio* $\Gamma = 8.6$*. The red boundary is taken from the experiment, the yellow one arises from the corresponding numerical simulation.*

Both figures 3.9 and 3.10 show the importance of an accurate edge detection from high-speed images. As already explained in the previous chapter, the key-step of this process is the conversion from a grey-scale into a black and white binary format. This operation crucially depends on the intensity threshold, which is manually set by the user in the present work. The adopted value arises from a "trial and error" adjustment aimed at minimizing the discrepancy (in terms of the total number of pixels) between the area bounded by the edges of the raw photo and the one enclosed in the binary image borders. The accuracy of this process depends on the lighting conditions and the imaging system resolution: ideal illuminations and resolutions would allow to obtain an intense

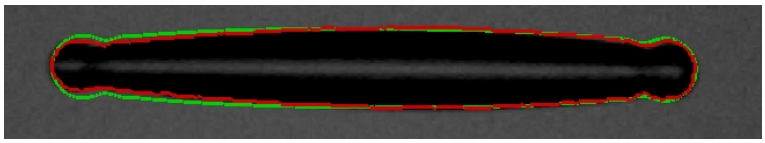

(a) $t = 0.796$

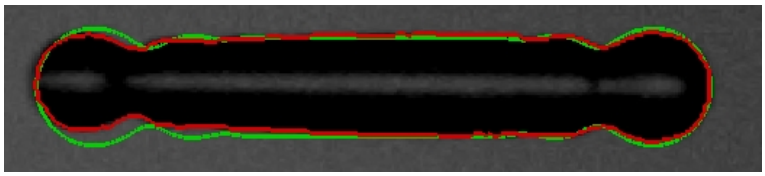

(b) $t = 1.989$

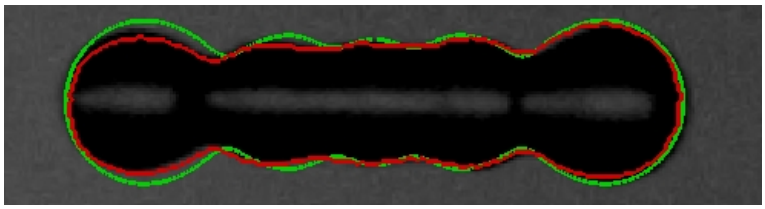

(c) $t = 3.183$

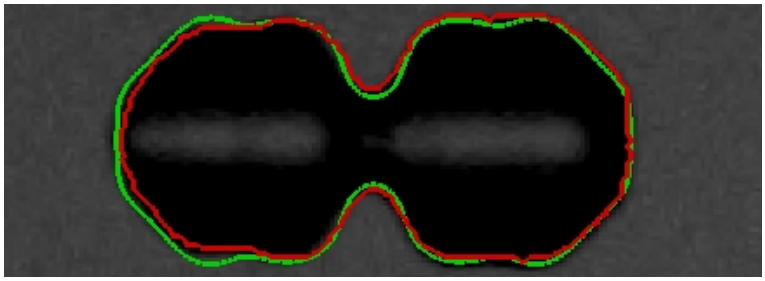

(d) $t = 5.17$

Figure 3.10: *Temporal evolution of a retracting filament profile with* $Oh = 0.013$ *and initial aspect ratio* $\Gamma = 9.6$. *The red boundary is taken from the experiment, the green one arises from the corresponding numerical simulation.*

and sharp contrast between the object and the background, avoiding the typical intermediate area of "grey shadow". However, this inconvenience is unavoidable in real experimental conditions (see figures 3.9 and 3.10), in which the lighting uniformity and the image resolution arise from a compromise with the field of view and the framing speed required to analyze the physical dynamics.

It should be noted that numerical and experimental data are in agreement although our simulations have omitted the effect of gravity: of course, this is present in real experiments. In fact, it can be proved that capillary retraction of our free liquid filaments is not affected by the gravitational field or even by the surrounding air. In the experimental conditions, liquid filaments in free fall

retract under the action of surface tension. The relative importance of gravity effects to capillary ones can be easily estimated: this is done by evaluating the ratio between the filament velocity variation due to gravity during one acoustic period, Δu_g, and the capillary velocity u_c. A good approximation of Δu_g is gw/u; on the other hand, the capillary velocity equals $u_c = R/t_c$, where $t_c = \sqrt{\frac{\rho R^3}{\sigma}}$ is the inertial-capillary time. As an indicative benchmark, we consider typical experimental values of $R = 0.5$ mm, $u = 1$ m/s and $w = 0.01$ m: the ratio $\Delta u_g/u_c$ results to be ~ 0.25. Moreover, the ratio of gravitational to capillary forces can be more classically calculated through the Bond number, $Bo = \frac{\Delta\rho g R^2}{\sigma}$ (here, $\Delta\rho$ is the difference in density of the two phases, g the gravitational acceleration, R the characteristic length, and σ the surface tension coefficient). By considering our typical water filaments ($R = 0.5$ mm) retracting in air at room temperature, we obtain $Bo \sim 0.035$. These small values reasonably suggest that gravity may not significantly affect the retracting filament dynamics and its fate. In fact, the good matching between computational and experimental results in terms of temporal evolution of the filament interface and its fate seems to confirm this conclusion.

Moreover, Chen *et al.* [65] have shown that the air viscous drag becomes significant only for filaments whose radius is smaller than $\frac{R\mu_{air}\mathrm{Oh}^2}{\mu}$. In our case, this critical threshold is always much smaller than the high-speed imaging system resolution.

Finally, as stated by Van Hoeve *et al.* [66], inertial effects arising from the surrounding air influence the liquid filament dynamics only when the air Weber number, $\mathrm{We}_{air} = \frac{\rho_{air} u^2 R}{\sigma}$, is larger than 0.2. In the tests of the present work, We_{air} is always far below this critical threshold (it never exceeds 0.07).

3.5 Results and discussion

3.5.1 Phase diagram

Figure 3.11 summarizes the main results of this section. The phase diagram $Oh - \Gamma$ focuses on the low-viscosity "critical region" ($Oh < 0.02$): it represents the filament fates in function of the Ohnesorge number Oh and the initial aspect ratio Γ. It is known that in this region of the phase space, the dominant mechanism for filaments breakup is end-pinching, a detachment of two retracting tip bulges from the central cylindrical region. According to the current state-of-the-art, for each Ohnesorge number Oh one critical aspect ratio Γ_c exists which represents the border between stable and unstable regimes, i.e. full contraction into a single drop (no-breakup) and segmentation into more droplets (breakup).

The novelty of this study is evident from the detailed phase diagram arising from our computational and experimental results. Unlike past results, figure 3.11 shows a clear intermediate transitional regime for a central window of aspect ratios Γ, in which the filaments undergo through an alternation of fates. There are multiple thresholds Γ_c at which filaments alternate between no-breakup and a newly discovered breakup mechanism, i.e. a "cut in two" at the filament middle section. We define this new breakup mode as "middle-breakup": the resulting two parts can be spherical droplets (insets *c*, *e*) or elongated filaments (inset *b*).

As stated in section 3.1.3, in their numerical simulations, Notz & Basaran [8] already noticed a third critical regime between no-breakup and end-pinching, in which they observed filaments' restabilisation and new breakup mechanisms (shape oscillations). However, they did not explain neither detect the fate alternation and the middle-breakup mode.

Our phase diagram presents three different regions: in figure 3.11, two red solid lines separate the three distinct regimes. The *end-pinching regime* characterizes long filaments (large Γ, above the upper line): filaments break through the end-pinching mechanism, i.e. the two retracting bulbous ends pinch-off from the cylindrical filament. The size of the central portion of the filament between the two separated droplets increases with the initial aspect ratio Γ. Photo inset *a* in figure 3.11 represents a case just above the lower border of end-pinching regime ($\Gamma = 15$, $Oh = 0.006$). The last stages of its contraction dynamics are depicted in figure 3.12.

The *short-filament regime* is located under the lower line: typically, it concerns filaments with $\Gamma < 5$. For such short filaments, the time needed for a full retraction is too short for any capillary instability to develop and reach a singularity (pinch-off). Therefore, in this regime filaments contraction is stable:

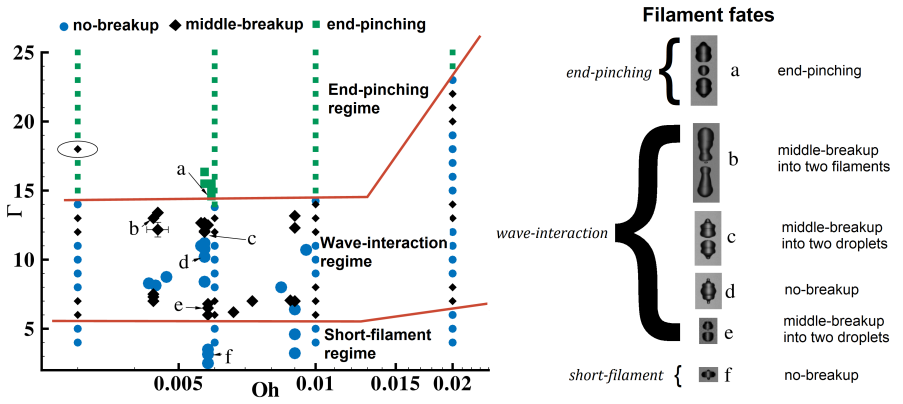

Figure 3.11: *Phase diagram $Oh - \Gamma$ focused on the critical region $Oh < 0.02$. Small solid symbols represent numerical simulations, whereas large solid symbols are experimental results. Different fates of filaments are identified by different colours. Typical experimental error bars are shown near photo inset b: within error bars, the agreement between experiments and numerical simulations is very good. On the right hand side, the main fates of the filaments are shown in photo insets (experimental high-speed images). The phase space is divided into three main regimes by two indicative red solid lines. Above the upper line, filaments break into three parts through end-pinching mode (photo inset a); a special case for $Oh = 0.003$ and $\Gamma = 18$ is highlighted by an oval and will be explained in section 3.5.2. Between the two lines, filaments alternate their fates between middle-breakup (photo insets b, c, e) and no-breakup (photo inset d). Below the lower line, filaments do not break undergoing through a stable contraction into a single drop (photo inset f).*

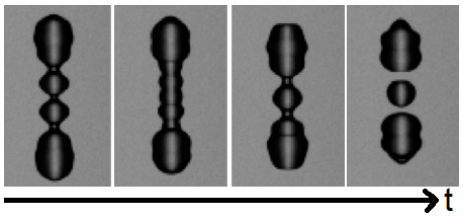

Figure 3.12: *Last stages of the capillary retraction of the filament (a) of figure 3.11. This case lies in the end-pinching regime: the filament breaks through the characteristic end-pinching mechanism, i.e. two receding blobs detach from the central cylinder.*

they collapse into a single drop. Figure 3.13 shows the last retraction steps of the filament denoted by the photo inset *f* in figure 3.11.

Both of the above filaments behaviors have been already widely studied through different methodological approaches, and they are well documented in the literature [7] [8] [9] [48] [49].

Between the two red solid lines, we introduce a new region representing

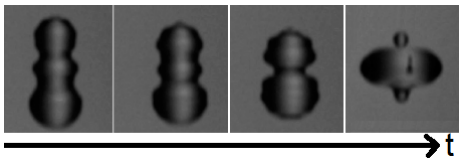

Figure 3.13: *Last motion stages of the filament (f) of figure 3.11. This mode belongs to the short-filament regime: the filament fully contracts into a single droplet.*

the fate-alternating transitional regime located between end-pinching and no-breakup mechanisms. We define it as *wave-interaction regime* since here the filament fate is determined by capillary waves interactions on its surface during the retraction. The different dynamics observed in this region are shown in the next figures 3.14-3.17. Moving from high towards low aspect ratios, we come across the following alternation of fates: middle-breakup into two filaments (inset *b*), middle-breakup into two droplets (inset *c*), stable collapse into a single drop (inset *d*), middle-breakup into two droplets (inset *e*).

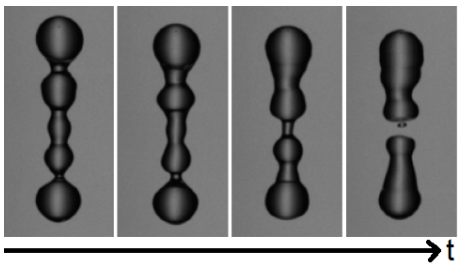

Figure 3.14: *Final contraction stages of the filament (b) of figure 3.11: it fragments into two shorter filaments.*

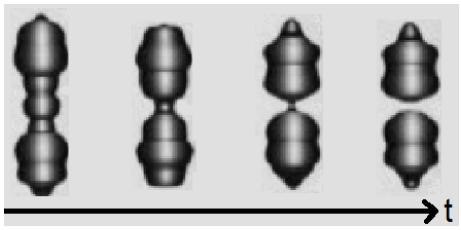

Figure 3.15: *Fate of the filament (c) of figure 3.11: it breaks at the middle section into two droplets.*

The underlying physics of this novel regime will be explained in detail in the next section 3.5.2.

In summary, the photo insets *a-f* of figure 3.11 represent all the different filament fates observed: each of their dynamics will be described and illustrated

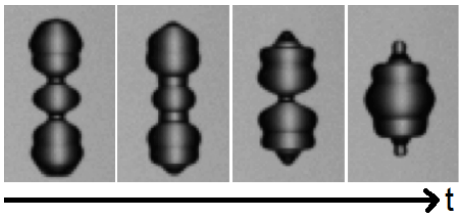

Figure 3.16: *Final retraction steps of the filament (d) of figure 3.11: it does not break up.*

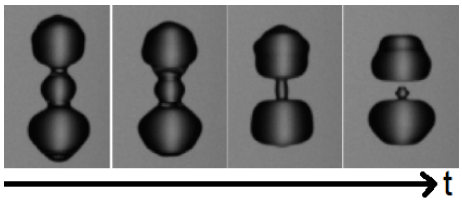

Figure 3.17: *Fate of the filament (e) of figure 3.11: middle-breakup into two droplets.*

in figures 3.23-3.28.

From figure 3.11, it should be noted the highlighted peculiar case of a filament with $Oh = 0.003$ and $\Gamma = 18$. Although it lies within the end-pinching regime where filaments break from the bulbous ends into (at least) three fragments, it breaks at its middle section into two shorter filaments. This particular dynamics will be well explained at the end of section 3.5.2.

Figure 3.18 reports the capillary retraction of a filament with $Oh = 0.0057$ and $\Gamma = 12$. Both instantaneous numerical profiles and corresponding experimental images are shown. This case belongs to the wave-interaction regime and corresponds to the photo inset *c* of figure 3.11: the filament breaks into two droplets through the middle-breakup mode. This analysis is taken as an indicative benchmark of the comparison between simulations and experiments. In this regard, the most important consideration concerns the main difference between numerical and experimental initial conditions. In experiments, liquid filaments are produced by means of a continuous jet breakup, and they are formed pinching off between two droplets. It is well known that in such cases breakup of inviscid fluids is characterized by a conically shaped neck with an opening half-angle of 18.1° [38] [67]. Therefore, when the filament pinches from the jet, it is not a perfect cylinder and its tips are not semi-spherical. While retracting, the free filament will evolve into a cylindrical shape and both ends will get hemispherical. By that time, the liquid flow field is not null neither stationary: the filament has already a non-negligible retraction speed. On the contrary, in numerical simulations the liquid filament is initially set at rest. This

discrepancy can be noted in figure 3.18 at $t = 2.0$ (time is made dimensionless by the inertial-capillary time t_c), for instance: at the early stage, the experimental filament retraction and its capillary surface-waves are already developed, compared with the corresponding numerical profile. However, the overall filament dynamics does not seem to be affected by these initial differences: especially at later stages, when a steady state is reached, the agreement between the numerical simulation and the experiment is very good. In the present example, for $t > 5.0$ (dimensionless experimental time), taking into account a time shift of 0.6 (due to the above-mentioned initial differences), the matching is qualitatively perfect. This consideration holds for all the cases reported in the present work.

Figure 3.18 shows that capillary waves originate at both bulbous ends and travel inwards on the filament surface; once they reach the middle section, they interact with each other. We can see the first significant interaction occurring at the middle plane between the secondary troughs at $t = 6.0$ (dimensionless experimental time). This leads to a neck formation: however, the neck is too weak to break the filament. Then, we can notice a neck reopening before a new superposition of the two thinner primary troughs at $t = 8.6$ (dimensionless experimental time). This time the originated neck is deep enough to trigger the thinning which eventually causes the filament breakup.

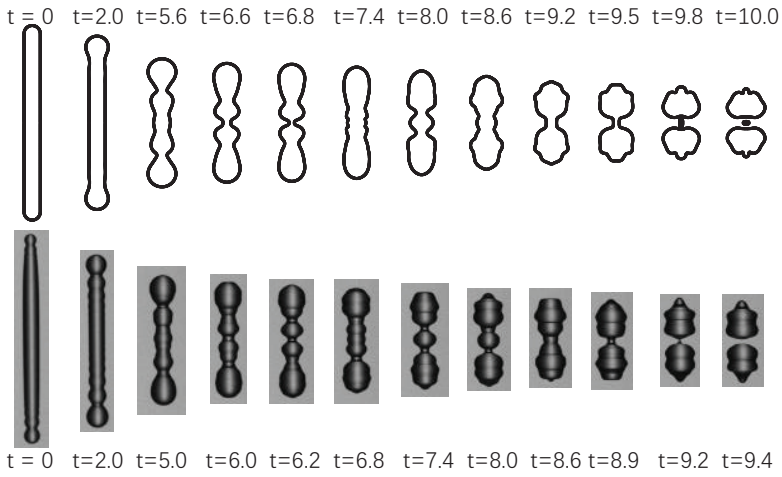

Figure 3.18: *Capillary retraction of a liquid filament with* $Oh = 0.0057$ *and* $\Gamma = 12$. *Instantaneous interface profiles from numerical simulation (upper side) and experimental photos (lower side).*

3.5.2 The capillary wave superposition model

Our main observation arising from both experiments and numerical simulations is that the fate of a filament with intermediate aspect ratio Γ is determined by the superposition of capillary waves originated at both tips that travel inwards along the free surface. We assume that the waves interaction is the responsible for the novel middle-breakup mechanism and the alternation of fates. However, since capillary ripples reach each other and interact very quickly, we find very hard to observe and study the waves directly on filaments with intermediate Γ: in fact, it is impossible to track and analyze them individually on such filaments. Therefore, we make a fundamental hypothesis: the evolution of such capillary waves is independent on the filament length. Thus, we first (computationally) investigate their propagation on semi-infinite or very long filaments; this way, we avoid waves' interactions and have enough time to track their individual paths. Afterwards, we report the obtained waves' space-time evolution onto filaments with intermediate Γ: interaction effects and potential breakup causes can be identified. We also assume that meeting capillary waves pass each other unchanged, unless their interaction is "fatal" (thinning neck leading to the filament breakup).

This is exemplified by figure 3.19, that shows capillary waves on a liquid filament with $Oh = 0.01$ and $\Gamma = 25$. Its final fate is breakup through end-pinching. The filament is long enough to observe the waves evolution before any interaction can occur. Part (a) of the figure defines troughs (T) and peaks (P) of the waves travelling from the retracting bulbous rim towards the middle plane $z = 0$: they are numbered in ascending order from the tip towards the center of the filament.

Song & Tryggvason [68] investigated the underlying physics of capillary waves generation for a retracting two-dimensional liquid sheet. The mechanism is analogous for cylindrical filaments, and it can be studied by analysing the vorticity field in the fluid domain. Figure 3.20 reports the vorticity contours (numerical results) near the wavy surface of the same filament of figure 3.19. From part (a) of figure 3.20 it can be noted that the sign variation of the axial curvature of the fluid interface near the rim and the neck T1 generates positive vorticity near the bulbous tip and negative vorticity at the neck section. The same explanation holds for the following peaks and troughs (figure 3.20(b)): the low viscous diffusion is responsible for the change of surface curvature, therefore positive vorticity near bulbous regions (positive curvature) and negative vorticity near necking sections (negative curvature). Figure 3.20(c) shows that this process is continuous and generates a series of capillary ripples towards the central cross section $z = 0$.

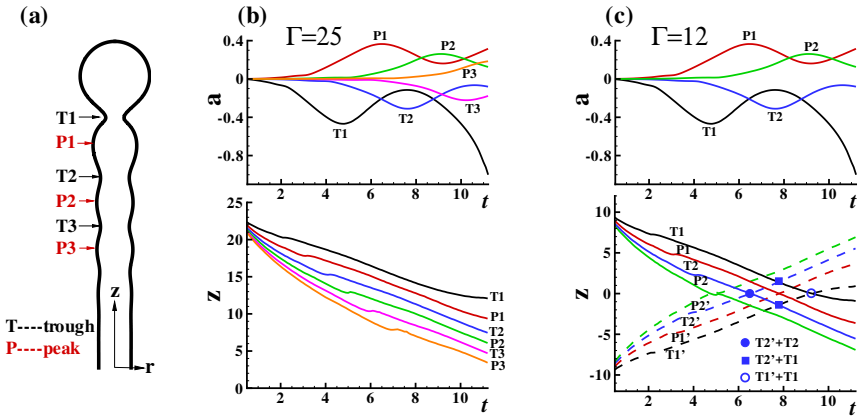

Figure 3.19: *(a) Notations of troughs (T) and peaks (P) of capillary waves on a retracting filament. (b) Time evolution of amplitude (upper) and axial position (lower) of wave troughs and peaks on a retracting filament with* $Oh = 0.01$ *and* $\Gamma = 25$ *(numerical simulation). (c) Waves' evolutions obtained in (b) mapped on a retracting filament with* $\Gamma = 12$ *and same Ohnesorge number (they are shifted towards* $z = 0$ *by the aspect ratio difference* $\Gamma_b - \Gamma_c$*); dashed lines represent the paths of the capillary waves propagating from the opposite filament tip. The waves evolution of (b) and (c) is assumed to be exactly the same: the only difference is that on the shorter filament (c) they start travelling closer. Unlike in the long filament dynamics (b), the retraction time in (c) is enough for waves to superimpose. This may result in a different filament fate [1].*

We define the instantaneous amplitude of waves peaks and troughs as $a(t) = r(t) - R$, where $r(t)$ is the instantaneous radius of the considered section and R is the initial unperturbed filament radius. In the graphs of figure 3.19, temporal evolutions of the waves' amplitudes and their z-coordinate are plotted: these quantities are made dimensionless by the length scale R. It should be noted that troughs and peaks amplitudes oscillate in time: the filament neck T1 starts to thin before a reopening, and eventually it decreases to -1 (singularity, i.e. end-pinching), for instance. As reported by Hoepffner & Paré [10], this end-pinching is indirect since the neck escapes the pinch-off (reopening) before breakup occurs. On the contrary, inviscid filaments ($Oh \leq 0.001$) are characterized by direct end-pinching: T1 decreases monotonically up to the singularity. In general, waves' temporal evolutions are function of the Ohnesorge number Oh.

Plot 3.19(b) (numerical simulations) clearly shows that troughs and peaks axial positions evolve linearly in time, except at the very early stage of retraction

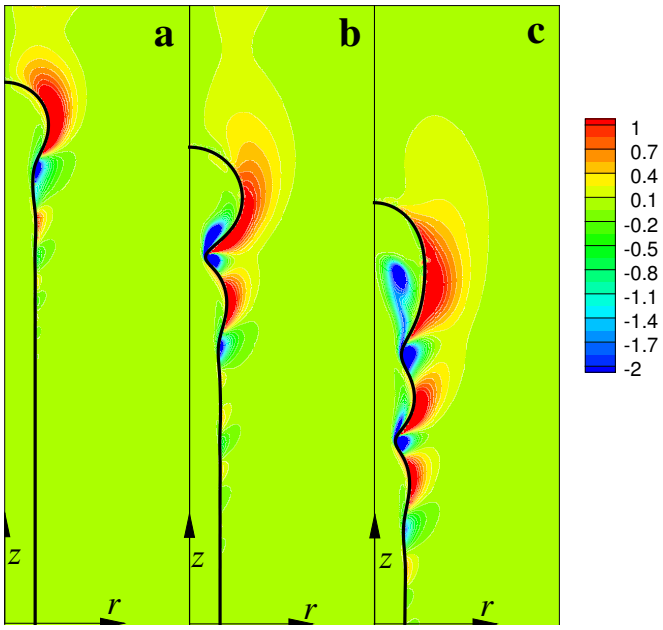

Figure 3.20: *Time evolution of the vorticity contours near the capillary retracting rim of a liquid filament with* $Oh = 0.01$ *and* $\Gamma = 25$ *(numerical simulation).*

when ripples are being formed. This means that the waves phase velocity is almost constant. Making the waves speed dimensionless by the Taylor-Culick capillary speed R/t_c ([47], [69]), for all present cases it results to be ~ 1.05. Also the wavelength λ (relative distance between adjacent peaks or troughs) is almost constant and approximately equal to $3R$ (in the next chapter, it will be shown that this value is characteristic of the explored quasi-inviscid regime). Hence, the waves phases are stationary with respect to the retracting rim.

Our simple but effective model is based on linear superposition of colliding capillary waves propagating from both filament tips, and it is able to predict the fate of filaments with intermediate initial aspect ratios. In particular, we assume that when two troughs T_i and T_j meet, they will interact forming a deeper trough of amplitude $b = a_{T_i} + a_{T_j}$.

Figure 3.19(c) plots the trajectories of the first two troughs and peaks travelling inwards from each bulb of a retracting filament with $Oh = 0.01$ and $\Gamma = 12$. According to the adopted notation, T_i' (P_i') represents the homologous trough (peak) of T_i (P_i), coming from the opposite tip of the filament. T1, P1,

T2, P2, T1', P1', T2' and P2' are usually sufficient to determine the filament fate in the transitional wave-interaction regime since higher order waves are already very damped and their perturbations are not relevant. The circular and square symbols represent the space-time coordinates of a collision between two troughs T_i and T_j, thus a deeper trough formation. According to the model, if the "superposed" amplitude $b = a_{T_i} + a_{T_j}$ exceeds a critical threshold, a capillary instability will break the filament. This critical amplitude is estimated through a simple scaling argument. Whether two approaching waves break up the filament after superposition or not depends on two competing time scales: the breakup time associated to the superposed wave amplitude, and the time needed for the following wave collision to occur at the same filament section.

The present model estimates the breakup time t_b through the Rayleigh-Plateau instability theory. The breakup time of the fastest growing mode is given by $t_b = -\frac{\ln|b|}{\omega_{max}}$, where $b = a_{T_i} + a_{T_j}$ is the superposed trough amplitude (its value is set as initial perturbation amplitude) and ω_{max} is the fastest wave growth rate (from [53]). The meeting time t_m can be easily evaluated knowing the observed (from present simulations) wavelength $\lambda \simeq 3R$ and the constant travelling waves speed $v_c \simeq 1.05R/t_c$. Then $t_m = \frac{\lambda}{2v_c}$. According to the model, the filament breaks up when $t_b < t_m$. This leads to the critical superposed trough amplitude $|b_c| = \exp\left(-\frac{\lambda\omega_{max}}{2v_c}\right)$. When $|b| > |b_c|$, the filament will break at the wave collision section due to capillary instability. In the range of interest $0.003 < Oh < 0.02$, $|b_c|$ lies between 0.605 ($|b_c|_{Oh=0.003}$) and 0.616 ($|b_c|_{Oh=0.02}$). These values are calculated assuming the observed wavelength ($3R$) and retraction speed ($1.05R/t_c$), and the maximum growth rate ω_{max} provided by the coupling of equations 3.3 and 3.4. For simplicity, $|b_c| = 0.61$ is set in the present work.

It should be noted that the above reported model applies linear superposition to finite-amplitude waves: this estimation violates mass conservation by an amount that is proportional to the square of amplitude.

Figure 3.21 is a comprehensive phase space in which filament fates predicted by the capillary wave superposition model are plotted together with the results arising from the run numerical simulations and experiments. The solid lines mark the boundaries between the three main different regimes; the dashed lines separate middle-breakup and no-breakup fates in the wave-interaction regime. The proposed model is able to well define the whole phase diagram and correctly predict almost all the filament behaviors.

The model predictive capability is now explained in detail. Figures 3.22-3.28 show capillary waves collisions on six liquid filaments of the same viscous regime ($Oh = 0.01$ in numerical simulations, $\mathcal{O}(Oh) = 10^{-2}$ in the corresponding experiments, which reproduce the same dynamics) and different initial aspect

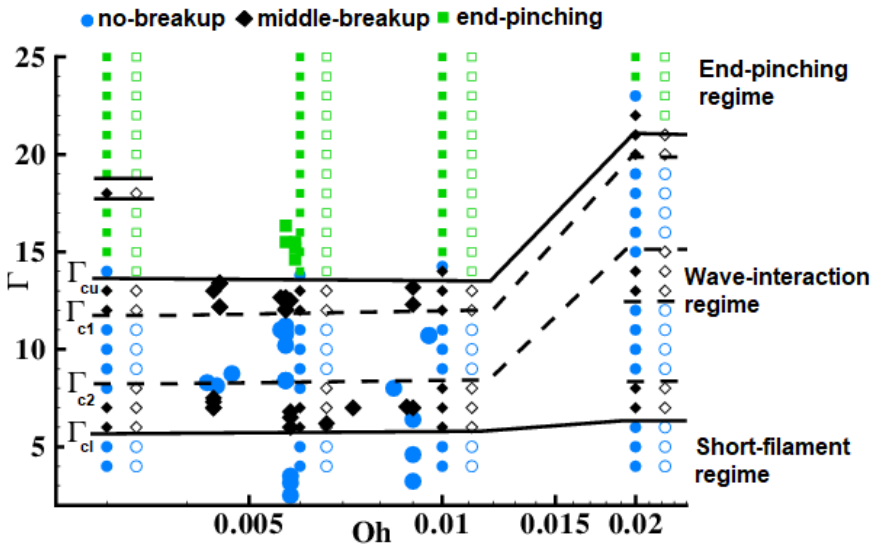

Figure 3.21: *The same $Oh - \Gamma$ phase diagram as in figure 3.11 with the capillary wave superposition model predictions. Open symbols represent the model predictions and refer to the same Oh of numerical simulations results on their left, denoted by small solid symbols; large solid symbols are experimental data. The solid and dashed lines mark fates boundaries predicted by the model. Solid lines divide the main three regimes; dashed lines separate middle-breakup and no-breakup modes in the wave-interaction regime.*

ratios Γ. Each of the shown cases corresponds to distinct fates and breakup modes illustrated in the phase diagram 3.11. As already stated, the considered examples only involve the first two troughs (i.e. T1 and T2) as higher order waves (very damped by viscosity) do not affect the filament fate. In figure 3.22 the (numerical) capillary retraction of a filament with $\Gamma = 25$ is represented. It undergoes through the classical end-pinching dynamics: the main trough T1, i.e. the neck connecting the bulbous rim and the cylinder, fully develops the singularity reaching $a = -1$ before any significant wave superposition can occur. Therefore, the filament breaks up into three parts as shown in the inset.

Figure 3.23 shows an experiment reproducing the same dynamics, but in this case the initial aspect ratio of the filament is different. From a practical point of view, it is very difficult to generate very long liquid filaments. Consequently, experimentally we were able to produce a filament with $\Gamma = 15$. In this case, no wave collision is strong enough to generate a trough leading the filament to breakup within the retraction time. Thus the neck T1 fully develops and reaches the singularity at $t = 9.7$ (experimental dimensionless time): the filament breaks in three fragments through the end-pinching mechanism.

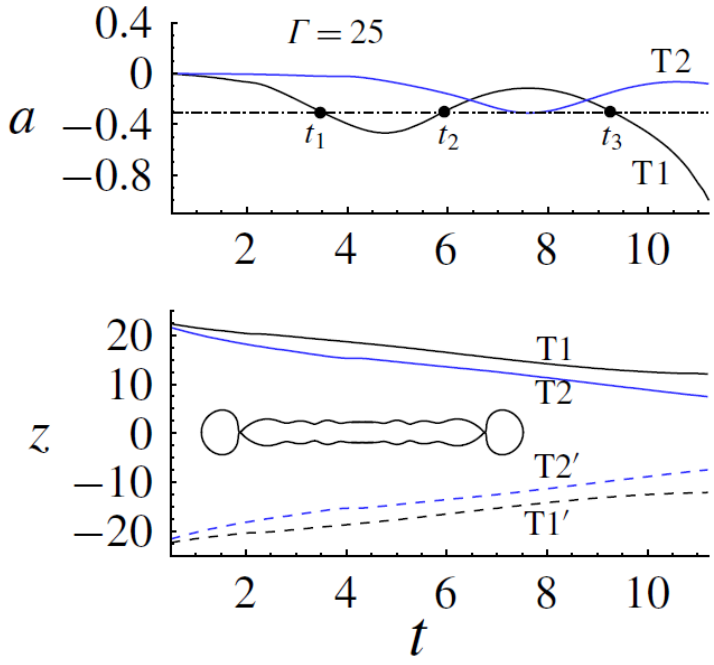

Figure 3.22: *Amplitudes (upper panel) and axial positions (lower panel) of wave troughs on a capillary retracting filament with* $Oh = 0.01$ *and* $\Gamma = 25$. *The three dots denote the instants when the neck amplitude T1 crosses the threshold* $a = -0.305$*: in fact, a linearly superposed amplitude due to the collision of T1 and T1' would lead to the breakup of the filament* ($b = a_{T_1} + a_{T_{1'}} = -0.61$). *The inset represents the numerical interface denoting the filament fate.*

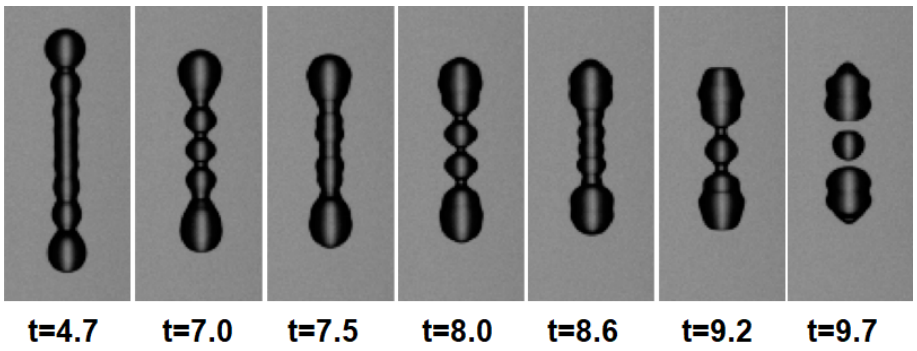

Figure 3.23: *Capillary retracting filament with* $Oh = 0.006$ *and* $\Gamma = 15$.

By decreasing the filament aspect ratio Γ, the detachment of the two ends occurs closer and closer to the central section of the filament ($z = 0$). The wave-interaction regime upper boundary is marked by $\Gamma_{cu} \simeq 13.4$ (see the phase diagram in figure 3.21): in this case, the neck T1 amplitude reaches the singularity

($a = -1$) exactly at $z = 0$.

In general, wave troughs closer to the middle section $z = 0$ interact earlier. However, their amplitudes are typically quite weak and their superposition may not be sufficiently large to cause a "fatal" necking and breakup. Moreover, the wave-amplitude variation in time is nonlinear and non-monotonic. As a result, in the wave-interaction regime, the superposing troughs which cause the filament breakup are generally not known *a priori*. Furthermore, the filament fate and its pinch-off dynamics might be not monotonically dependent on the initial aspect ratio Γ.

In figure 3.22 the instants t_1, t_2 and t_3 (when T1 amplitude crosses $a = -0.305$) are marked: this is a critical threshold where the T1 + T1' collision would produce a linearly superposed amplitude $b = a_{T_1} + a_{T_{1'}} = -0.61$ leading to breakup. Observing the (numerically derived) time evolution of T1 amplitude, we can state that if the neck T1 reaches the central section $z = 0$ at $t_1 \leq t \leq t_2$ or $t \geq t_3$, the T1 + T1' collision will be "fatal" as the superposed trough ($|b| = \left|a_{T_1} + a_{T_{1'}}\right| \geq 0.61$) will break the filament from the middle due to capillary instability. According to the present model, the capillary waves travel along the filament surface at a constant speed. Thus, the time needed by a trough to reach the central section $z = 0$ can be easily calculated and only depends on the filament length. Results shown in figures 3.24-3.28 are obtained by mapping the waves evolving on the filament with $\Gamma = 25$ onto shorter filaments. Based on these observations, we conclude that the wave-interaction regime contains two Γ-ranges in which middle-breakup occurs. Experiments and numerical simulations plotted in figure 3.21 confirm this conclusion.

Figure 3.22 also suggests that a narrow Γ window exists in which filaments will undergo through a middle-breakup because of the superposition T2 + T2' at the middle section $z = 0$: in fact, we notice that in a very small time range located around $t = 7.5$ (dimensionless computational time), the amplitude of the trough T2 is less than the critical threshold -0.305.

Such scenario is proposed in the following figure 3.24. A retracting filament with initial aspect ratio $\Gamma = 13$ breaks in the middle due to the T2 + T2' collision occurring at $t = 7.44$ (according to numerical simulations). This fatal interaction occurs at $z = 0$ before any other potential wave collision (i.e. T1 + T2', T1 + T1'). The agreement between the numerical simulation and the experiment is qualitatively very good. The time shift of the breakup instant is due to the slightly different Ohnesorge number and the already discussed discrepancies between numerical and experimental initial conditions.

Analogous considerations hold for all the following examples. In the numerical plots, t_1, t_2 and t_3 instants are always highlighted as vertical solid lines, the insets are interfaces representing the filament fate, the circular and square

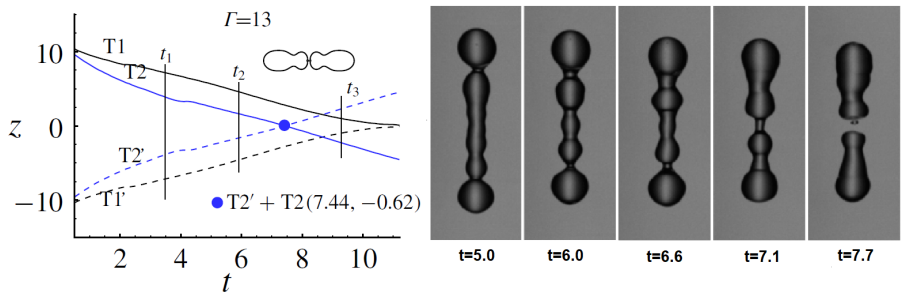

Figure 3.24: *On the left, axial positions of wave troughs on a capillary retracting filament with* $Oh = 0.01$ *and* $\Gamma = 13$ *in terms of time. Here,* t_1*,* t_2 *and* t_3 *are labelled as vertical solid lines; the circular symbol marks the collisions between T2 and T2', and the two numbers in the legend are the collision instant and the resulting linearly superposed amplitude, respectively; the inset represents the filament fate: middle-breakup in two shorter filaments. On the right, experimental images of the capillary retraction of a liquid filament with* $Oh = 0.005$ *and* $\Gamma = 13$*.*

symbols represent troughs' superpositions, and the legend shows the collision instant (dimensionless computational time) and the resulting linearly superposed amplitude, respectively.

Figure 3.25 reports the capillary retraction of a liquid filament with initial aspect ratio $\Gamma = 12$. As expected, the wave "meeting" T2 + T2' occurs earlier than in the filament of figure 3.24 due to its smaller length. However, at the collision instant the superposed trough is shallower: its amplitude is lower than the critical threshold, thus no breakup is observed. Additionally, the following superposed troughs T1 + T2' and T1' + T2 are not deep enough to produce the filament breakup. In this case, the T1 + T1' collision is fatal: in fact, it happens soon after t_3 (precisely at $t = 9.28$). It generates a thinning neck which rapidly leads to the middle breakup of the filament in two drops. In this case, the wave superposition model correctly predicts the fate of the filament which is shown in the numerical inset. The matching with the experimental images is qualitatively very good.

It is interesting to notice that the T2 + T2' superposition, if deep enough, splits the filament into two shorter cylindrical filaments (figure 3.24), whereas the fatal T1 + T1' collision fragments the filament into two spherical drops (figure 3.25).

The neck superposition T1 + T1' happens earlier as the initial aspect ratio Γ of the liquid filament is decreased. Looking at the temporal evolution of the trough T1 amplitude shown in figure 3.22, we can state that when T1 reaches the central section $z = 0$ at $t_2 < t < t_3$, it will be too weak to break the filament: in fact, the linearly superposed amplitude $|b| = \left|a_{T_1} + a_{T_{1'}}\right|$ arising from

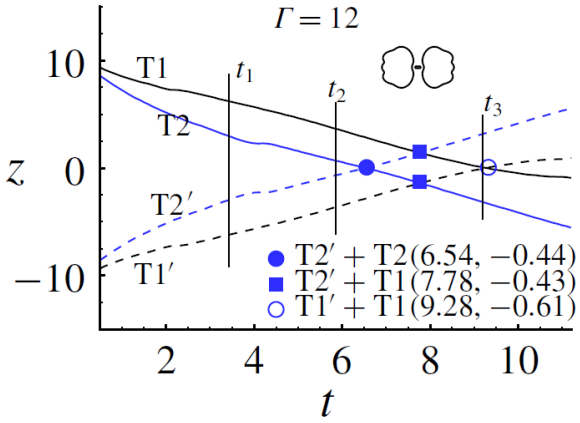

(a) Numerical simulation

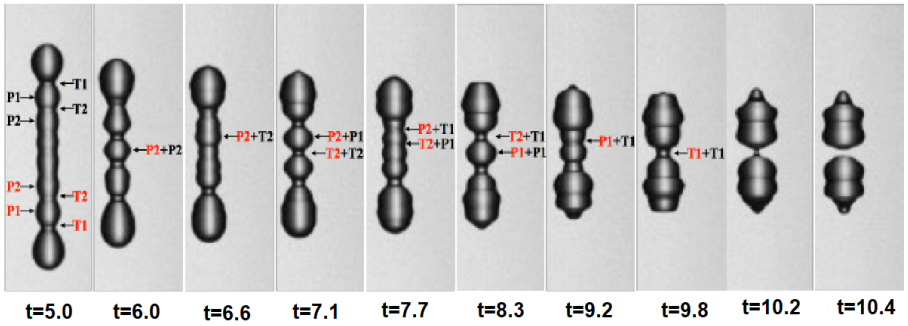

(b) Experiment

Figure 3.25: *(a) Axial positions of wave troughs on a capillary retracting filament with* $Oh = 0.01$ *and* $\Gamma = 12$ *in terms of time. (b) Experimental images of the capillary retraction of a liquid filament with* $Oh = 0.006$ *and* $\Gamma = 12$.

the collision T1 + T1' is smaller than the critical threshold 0.61. Figure 3.26 represents an example of this scenario: the initial aspect ratio of the filament is $\Gamma = 10$ in the numerical simulation and $\Gamma = 10.5$ in the experiment. Within the retraction time, no wave collision is strong enough to lead to breakup, thus the filament recoils into a single drop. This case lies in the no-breakup region of the wave-interaction regime.

The critical aspect ratio Γ_{c1} separating the middle-breakup and no-breakup fates in the upper part of the wave-interaction regime is marked by the upper dashed line in figure 3.21. It corresponds to the filament length in which the neck T1 reaches the middle section $z = 0$ exactly at the instant t_3. In our Oh range of interest, $\Gamma_{c1} \simeq 11.8$.

By decreasing the initial aspect ratio Γ, we find filaments whose trough T1 reach the middle section at an instant between t_1 and t_2. In such cases, the T1 +

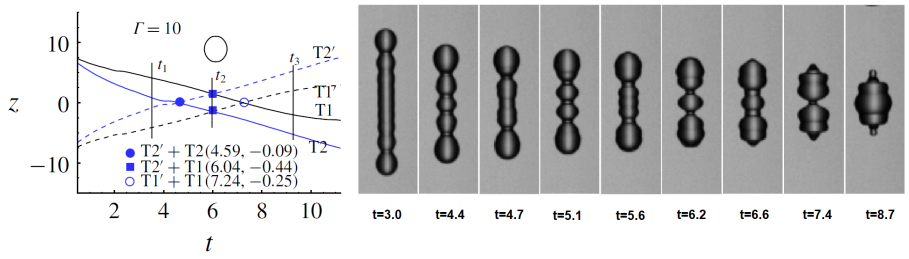

Figure 3.26: *On the left, axial positions of wave troughs on a capillary retracting filament with* $Oh = 0.01$ *and* $\Gamma = 10$ *in terms of time. On the right, experimental images of the capillary retraction of a liquid filament with* $Oh = 0.006$ *and* $\Gamma = 10.5$.

T1' wave interaction produces a neck which is deep enough to cause the filament middle-breakup ($|b| = |a_{T_1} + a_{T_{1'}}| \geq 0.61$). An example is provided in figure 3.27: the filament simulated in the numerical simulation has $\Gamma = 6$, whereas the initial aspect ratio of the filament experimentally analysed is $\Gamma = 6.5$. This case lies in the lower middle-breakup region of the wave-interaction regime.

The critical aspect ratio Γ_{c2} that divides the no-breakup and middle-breakup regions in the lower part of the wave-interaction regime is represented by the lower dashed line in the phase diagram of figure 3.21. It corresponds to the filament length where T1 reaches $z = 0$ at t_2. In the present Oh window, $\Gamma_{c2} \simeq 8.2$.

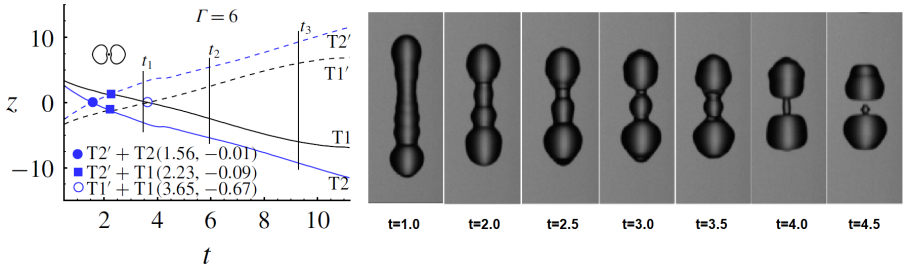

Figure 3.27: *On the left, axial positions of wave troughs on a capillary retracting filament with* $Oh = 0.01$ *and* $\Gamma = 6$ *in terms of time. On the right, experimental images of the capillary retraction of a liquid filament with* $Oh = 0.005$ *and* $\Gamma = 6.5$.

Finally, we report the retraction dynamics of short filaments in which the troughs are still weak within the retraction time. In particular, the neck T1 reaches the middle section $z = 0$ before t_1, and no wave collision is sufficiently large to generate breakup. Thus, the filament is stable and collapses into one drop. Figure 3.28 shows the case of a retracting filament with initial aspect ratio $\Gamma = 5$ in the numerical simulation and $\Gamma = 5.5$ in the experiment. This

example falls in the short-filament regime of the phase diagram shown in figure 3.21.

The boundary between the wave-interaction and short-filament regimes (the lower black solid line in figure 3.21) corresponds to the critical aspect ratio Γ_{cl} where the filament neck T1 reaches the middle plane $z = 0$ at the instant t_1; for $0.001 \leq Oh \leq 0.01$, $\Gamma_{cl} \simeq 5.8$.

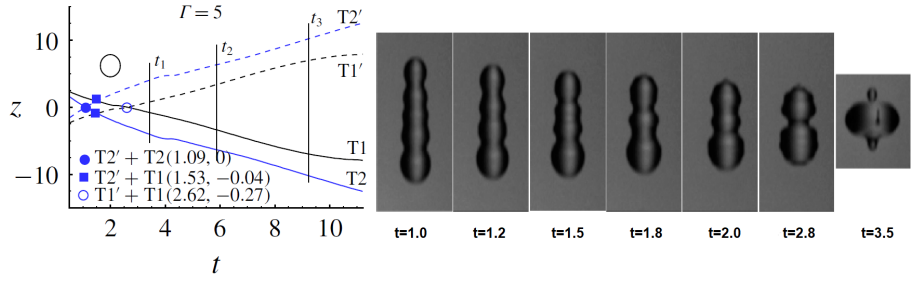

Figure 3.28: *On the left, axial positions of wave troughs on a capillary retracting filament with* $Oh = 0.01$ *and* $\Gamma = 5$ *in terms of time. On the right, experimental images of the capillary retraction of a liquid filament with* $Oh = 0.005$ *and* $\Gamma = 5.5$.

Now we provide a clarification on the singular case of the filament with $Oh = 0.003$ and initial aspect ratio $\Gamma = 18$ highlighted in the phase diagram of figure 3.11. This filament undergoes the middle-breakup mode: it splits into two shorter filaments from its central section although it lies in the end-pinching regime (longer and shorter filaments both break through end-pinching). The collision between the troughs T3 and T3' is responsible for this filament fate. In fact, they reach the middle section $z = 0$ before the neck T1 fully develops end-pinching, and they generate a trough whose amplitude is deeper than the critical threshold, leading to the filament breaking up from the middle. On a slightly shorter filament, the T3 + T3' interaction occurs earlier and it is not strong enough to produce breakup since their superposed amplitude does not reach the critical value. However, the filament is sufficiently long for its neck T1 to fully develop and reach the singularity (end-pinching). On the other hand, a slightly longer filament allows T1 to attain $a = -1$ before the troughs T3 and T3' can meet each other. Therefore, the filament breaks through the classical end-pinching mechanism.

It is interesting to notice that this case is the only one among all the performed simulations and experiments for which the trough T3 dynamics does affect and determine the filament fate. Apart from this exception, we can conclude that our simplistic model (which only considers T1 and T2 paths) is able to detect all the observed filaments' behaviors in the analysed portion of the

$Oh - \Gamma$ phase diagram. Thus, it can be used to define all the different regions of the phase space.

The main assumption of our simple model is that in case of collision between two troughs forming a neck whose linearly superimposed amplitude is deeper than a critical threshold, the filament will break at the neck section through the Rayleigh-Plateau instability mode. We analyse this scenario in detail: figure 3.29 shows the shape of the filament of figure 3.27 and its pressure field at $t = 3.65$ (dimensionless computational time), the instant at which the troughs T1 and T1' collide at the middle plane $z = 0$. The filament fate is middle-breakup due to the capillary instability produced by this wave interaction. It is worth to note that the capillary pressure is positive at the neck section: the azimuthal-curvature radius is positive and smaller than the axial-curvature one, which is negative due to the outer curvature center (see equation 2.2). The resulting pressure gradient pushes liquid away from the neck, eventually causing the filament breakup. In fact, without the trough collision, the Laplace pressure would be negative at T1 section since the azimuthal-curvature radius would be larger than the axial one.

Analogous considerations apply to the filaments analysed in figures 3.24 and 3.25: the trough collision (i.e. T2 + T2' or T1 + T1') is responsible for the pressure increase which leads to the necking and the middle-breakup dynamics.

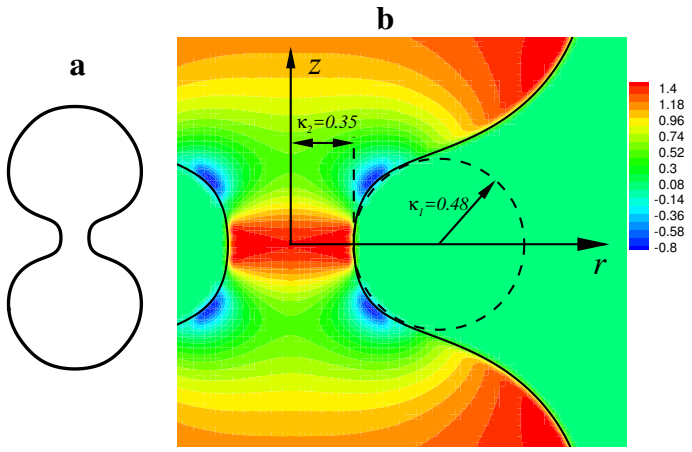

Figure 3.29: *(a) Shape of a recoiling filament with* $Oh = 0.01$ *and initial aspect ratio* $\Gamma = 6$ *at the instant of the troughs T1 + T1' collision. (b) Zoom of the neck section and pressure contours.* κ_1 *and* κ_2 *are the axial and azimuthal curvature radii, respectively [1].*

3.5.3 Limitations of the model

Although the capillary wave superposition model has been proved to be usually effective in predicting the retracting filament fate, it also presents some limitations. For instance, figure 3.21 shows that it fails to determine the fate of liquid filaments just above the lower boundary of the end-pinching regime. In fact, the capillary wave superposition model predicts end-pinching whereas numerical simulations and available experiments produce no-breakup or middle-breakup for the majority of the tested Ohnesorge numbers Oh. This discrepancy is due to a fundamental assumption: according to the presented model, capillary waves pass each other unchanged after the collision, unless the superposed trough amplitude b would be "fatal", forming a thin neck which leads to breakup within the meeting time t_m. This hypothesis does not faithfully reproduce the real physics: in fact, in such filaments the neck T1 collides with the peak P1' shortly before end-pinching. This interaction reopens the neck and escapes end-pinching, leading to no-breakup or middle-breakup behaviors.

Another important limitation of the model regards its own definition: it is not well-defined. In fact, it depends on numerical simulations of non-interacting waves at each Ohnesorge number Oh. Filaments' fates are predicted by the model in the wave-interaction regime simply by mapping waves trajectories previously obtained for long filaments onto shorter ones and considering their collisions.

The main difficulty in building a complete, independent, and self-contained predictive model lies in the complex physics of capillary waves. In fact, the oscillation in time of the waves' amplitudes is complicated, and modelling their dynamics results to be non-trivial. In this regard, previous studies have investigated and analytically described the propagation of capillary waves: for instance, self-similar solutions were derived for retracting liquid wedges [70] and cones [71].

Finally, our work focused on the almost inviscid regime only. In fact, the capabilities of the capillary wave superposition model have not been tested on significantly viscous filaments.

3.6 Conclusions

In brief, the proposed model can explain the fates of retracting liquid filaments in the low-viscosity region of the phase space $Oh - \Gamma$. The diagram is divided into three main regimes.

Sufficiently long filaments breakup through end-pinching since the necks have enough time and space to fully develop and reach the singularity (pinch-off).

Short filaments are stable and do not break because of the short retraction time: troughs are too weak and not developed enough within this period.

The dynamics of intermediate-length filaments is governed by capillary waves interactions. The retraction time is too short for the necks to fully develop end-pinching, but breakup can still occur as a result of capillary waves superposition. A filament breaks into two droplets or two filaments depending on the nature of the "fatal" colliding troughs and their meeting instant. Since the waves' amplitudes oscillate in time, the intermediate-Γ window of filaments is characterized by an alternation between no-breakup and middle-breakup modes.

The main novelties of the present piece of work are the fate-alternating transitional regime and the middle-breakup mechanism in retracting liquid filaments, which prove the importance of capillary waves superposition. This phenomenon may be exploited in several practical applications as a new mean to control the integrity and breakup of liquid filaments in a wide range of lengths. For instance, the novel middle-breakup dynamics may be used to produce equal-sized small droplets. Ink-jet printing is one of the industrial technologies that can benefit from this study to improve its current strategies. However, this analysis may be also applicable to other techniques, such as biological and medical systems based on rapid droplet spreading [72].

The next chapter is focused on the mathematical modeling of the capillary recoiling dynamics of liquid filaments: the analysis provides a formal description of the space-time evolution of the fluid interface.

Chapter 4

Shape of a recoiling liquid filament

In this chapter, we study the capillary retraction of a Newtonian semi-infinite liquid filament through analytical and numerical methods. The state-of-the-art on this classic problem is mainly composed of numerical analysis and experiments. In this work we adopt an alternative approach: we develop analytical arguments in order to obtain a quasi-analytical asymptotic expression of the fluid interface.

In particular, we corroborate numerical results with a theoretical model which uses the well-known Eggers one-dimensional (1D) approximation for a free-surface slender cylindrical flow [73]. We study the 1D-model equations through asymptotic analysis to derive an expansion of the filament profile for long times, once a steady state is reached after a transient regime. Three distinct regions with different characteristic length and time scales are identified in the retraction domain: a growing spherical rim, a steady filament section and an intermediate matching zone.

These solutions are then matched together in the whole fluid domain to obtain a global expression. We show that liquid filaments naturally develop travelling capillary waves along their surface and a neck behind the blob. The waves' asymptotic wavelength, decay length, and the minimum neck size are analysed in terms of the Ohnesorge number. Finally, our results are compared with previous studies from the literature [8] and numerical simulations in Basilisk [15] obtaining a good agreement. This analysis provides a full picture of the recoiling process going beyond the classic result of the velocity of retraction found by Taylor and Culick.

4.1 Introduction

As explained in previous chapters, a liquid filament free in the air retracts by the action of surface tension. This is a classical scenario which has been widely analysed in the literature through theoretical, numerical and experimental approaches (see [47], [48], [49], [9], [8], [10], [50]). This phenomenon presents a key scientific interest which is linked to both fundamental research and applications: in fact, fluid retraction dynamics occurs in many engineering and industrial problems such as atomisation, spraying, inkjet printing, and microfluidics.

However, the first significant studies on this topic were performed by Taylor [44] and Culick [45], who focused on the capillary retraction of a thin planar fluid sheet. Following basic physics principles, i.e. mass and momentum conservation, they found that the fluid free edge accumulates mass from the film as it retracts, and a growing rim with a circular section is formed. The rim recedes at a retraction speed that tends to a constant value, the *Taylor-Culick speed*. This velocity is independent of the fluid viscosity as it results from a balance between inertial and capillary forces.

In the case of a cylindrical filament with radius R, the liquid is collected at the receding tip in a growing spherical blob. Mass and momentum balance applied to a domain enclosing the rim yields the Taylor-Culick speed (see figure 4.1). The external forces acting on the domain are produced by the pulling surface tension σ of the fluid ($F_\sigma = 2\pi\sigma R$) and the pushing filament inner pressure ($F_p = -\frac{\sigma}{R}\cdot\pi R^2 = -\pi\sigma R$). These forces originate a momentum increase of the rim, and this leads to a constant retraction speed.

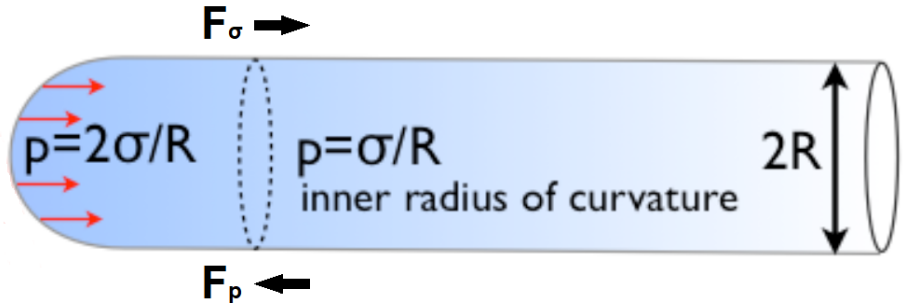

Figure 4.1: *Scheme of a cylindrical liquid filament with radius R retracting by the action of the surface tension σ.*

The mass accumulated in the spherical blob is $m_b(t) = \rho\pi R^2 z_b(t)$, where $z_b(t)$ is the axial coordinate denoting the position of the blob in time, and ρ the fluid density. The momentum equation for the blob is:

$$\frac{\mathrm{d}}{\mathrm{d}t}\left(m_b(t)\frac{\mathrm{d}}{\mathrm{d}t}z_b(t)\right) = F_\sigma + F_p = \pi R\sigma$$

Replacing the rim mass expression in the last equation, we get:

$$\frac{\mathrm{d}^2}{\mathrm{d}t^2}(z_b^2(t)) = \frac{2\sigma}{\rho R}$$

We can integrate twice the last equation imposing the initial conditions $z_b(t = 0) = 0$ and $\frac{\mathrm{d}}{\mathrm{d}t}(z_b(t)) \mid_{t=0}$ finite. This yelds: $z_b(t) = \sqrt{\frac{\sigma}{\rho R}}t$. Consequently, the blob retracts at a constant velocity, the Taylor-Culick speed:

$$c = \sqrt{\frac{\sigma}{\rho R}}. \tag{4.1}$$

As shown by numerical and experimental studies [10], in the long time limit the system dynamics is mostly represented by the blob growth. In a good approximation, the rim keeps a spherical shape which slowly grows in time. The time evolution of its radius $R_b(t)$ can be derived through a basic mass conservation argument. Under these assumptions, the rim mass balance equation is the following:

$$\rho\pi R^2 c = \frac{\mathrm{d}}{\mathrm{d}t}\left(\rho\frac{4}{3}\pi R_b^3(t)\right) \tag{4.2}$$

Integrating this equation with the initial condition $R_b(t = 0) = R$ leads to the time power law of the blob radius (where $t_c = \sqrt{\frac{\rho R^3}{\sigma}}$ is the capillary time):

$$R_b(t) = R\left(1 + \frac{3}{4}\frac{t}{t_c}\right)^{1/3} \Rightarrow R_b(t) \propto t^{1/3}. \tag{4.3}$$

However, subsequent detailed studies by Savva & Bush [13] have shown through numerical simulations and experiments that the retraction velocity converges to the Taylor-Culick value after an initial unsteady state. Hence, the "Taylor-Culick regime" is only a quasi-stationary asymptotic limit. Indeed, this prediction is derived from very simple arguments: mass and momentum balance applied at a global scale (net force acting on the growing blob). Moreover, this classical model does not take into account the fluid viscosity.

Nevertheless, Brenner & Gueyffier in 1999 [14] and Savva & Bush in 2009 [13] showed that the filament dynamics is heavily influenced by the liquid viscosity μ. In particular, their experiments and numerical simulations proved that the viscosity determines the transient-state characteristic time, the interface stability, and the filament profile.

For planar thin sheets, Brenner & Gueyffier (1999) [14] have reported that highly viscous retracting fluids do not originate any rim: in this case a constant

thickening of the film is observed during the retraction. On the contrary, when viscosity is low enough and capillarity dominates the dynamics, a thin neck is formed between the circular rim and the film, whose height remains unperturbed [74].

As it will be shown in the next section, the problem is governed by a single dimensionless parameter, the Ohnesorge number $Oh = \frac{\mu}{\sqrt{\rho\sigma R}}$, which represents the ratio of viscous and capillary forces. Examples of the behaviour of the retracting film for different Oh are shown in figure 4.2.

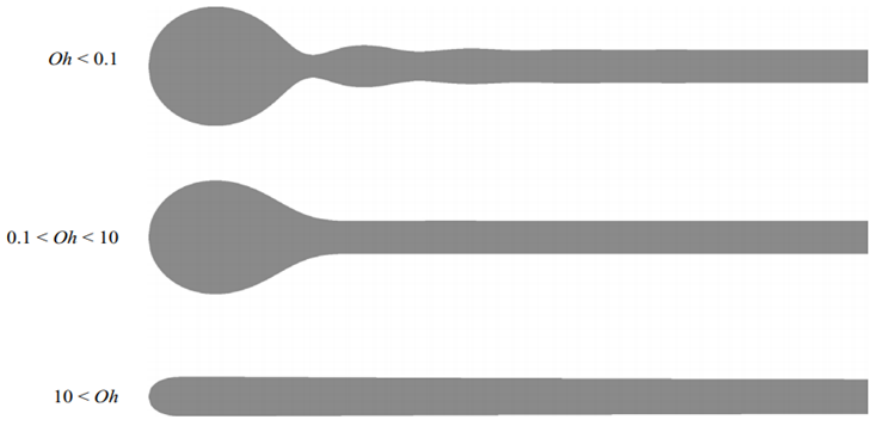

Figure 4.2: *Taken from [13]. Three distinct regimes for a capillary retracting viscous sheet obtained by Brenner & Gueyffier (1999) [14]. As Oh increases, the capillary ripples, the neck and the rim disappear because of the dissipative action of viscosity.*

These observations prove that the traditional model, resulting from Taylor and Culick arguments, of a spherical growing rim next to a constant radius filament cannot accurately describe the real retraction dynamics.

In this chapter, we study the filament interface evolution in the long-time limit, i.e. when the blob radius R_b is much larger than the filament radius R, using a local asymptotic analysis. In section 4.2, we present a set of two one-dimensional equations for a free-surface slender liquid filament under the lubrication approximation. We use this model to analyse the filament dynamics in its quasi-steady state. In section 4.3, we show that the long-time asymptotic solution is separated into three regions that have different length and time scales: a steady cylinder far from the rim, a receding blob, and an intermediate matching zone. In section 4.4, following a formalism analogous to the one used by Gordillo *et al.* (2011) [74] for a planar liquid film, the three different solutions are "matched" together to provide a unique asymptotic matching solution of the evolving filament shape. Travelling capillary waves and the neck connecting the

blob and the filament (see figure 4.3), which can be seen under some conditions, are analysed in terms of the Ohnesorge number. These results are important as they provide a full and formal description of the Taylor-Culick regime.

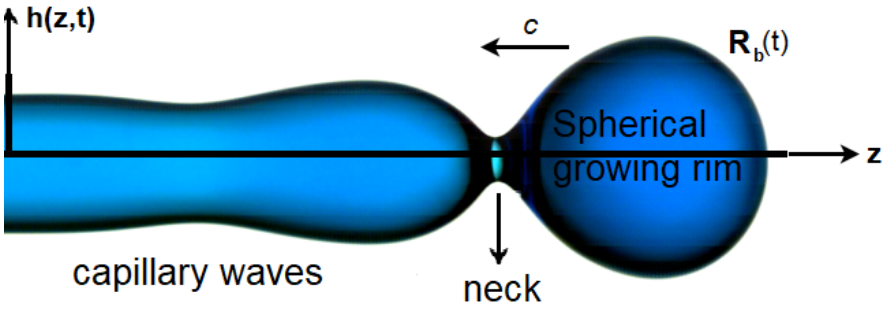

Figure 4.3: *Scheme of a capillary retracting liquid filament in the Taylor-Culick regime. The spherical rim recedes at a constant velocity* $c = \sqrt{\frac{\sigma}{\rho R}}$ *and its radius* R_b *grows in time. Under some conditions, capillary waves travel along the filament surface and a neck is formed between the blob and the cylindrical region.*

4.2 Dynamics of a capillary retracting liquid filament

In this section, we consider an incompressible viscous liquid axisymmetric body surrounded by an inert ambient gas with negligible density and viscosity. Under this hypothesis the boundaries of the liquid can be considered as free surfaces. The filament, initially at rest, is a semi-infinite cylinder aligned to the z-axis (see figure 4.3) with a hemispherical cap whose radius R is the same as the one of the cylindrical section. The thickness of the filament is large enough to apply continuum mechanics theory. The dynamics of the liquid body is governed by the incompressible Navier-Stokes equations (mass and momentum conservation laws):

$$\nabla \cdot \mathbf{u} = 0 \tag{4.4}$$

$$\frac{\partial \mathbf{u}}{\partial t} + \mathbf{u} \cdot \nabla \mathbf{u} = -\frac{\nabla p}{\rho} + \nu \nabla^2 \mathbf{u} + \frac{\sigma}{\rho} \kappa \delta_s \mathbf{n}, \tag{4.5}$$

where $\mathbf{u} = u_r \mathbf{e_r} + u_z \mathbf{e_z}$ represents the velocity field (the azimuthal component is assumed to be null), p the pressure field, ν the kinematic viscosity and ρ the density of the liquid, σ the liquid-gas surface tension coefficient; the effect of

gravity is not considered here. Surface tension forces are represented through a Dirac delta function δ_s at the gas-liquid interface; κ is the local mean curvature of the interface, and $\mathbf{n}$ denotes the local normal direction.

Following the same approach of Eggers & Dupont (1994) [73] and Popinet & Antkowiak (2011) [75], we write the full scalar equations of motion for an incompressible viscous fluid in cylindrical coordinates: these are continuity and momentum conservation along axial and radial directions (the flow is assumed axisymmetric, thus invariant along the azimuthal direction).

$$\partial_r u_r + \frac{u_r}{r} + \partial_z u_z = 0 \tag{4.6}$$

$$\partial_t u_z + u_r \partial_r u_z + u_z \partial_z u_z = -\frac{1}{\rho}\partial_z p + \nu \left(\partial_{rr} u_z + \partial_{zz} u_z + \frac{1}{r}\partial_r u_z \right) \tag{4.7}$$

$$\partial_t u_r + u_r \partial_r u_r + u_z \partial_z u_r = -\frac{1}{\rho}\partial_r p + \nu \left(\partial_{rr} u_r + \partial_{zz} u_r + \frac{1}{r}\partial_r u_r - \frac{u_r}{r^2} \right) \tag{4.8}$$

We need to add the proper boundary conditions on the gas-liquid interface in order to close the system. These are the free surface boundary conditions.

First, the kinematic boundary condition is given by $\frac{\mathrm{d}F}{\mathrm{d}t} = 0$, where the gas-liquid interface is described by $F(\mathbf{x}, t) = 0$. In the slender jet limit (radial length scale much smaller than axial dimensions), the interface can be defined as $F(\mathbf{x}, t) = h(z, t) - r = 0$. Under this assumption, the kinematic boundary condition is:

$$\frac{\mathrm{d}F}{\mathrm{d}t} = \partial_t h - u_r + u_z \partial_z h = 0 \text{ at } r = h. \tag{4.9}$$

The interfacial stresses conditions are given by $\mathbf{n} \cdot \boldsymbol{\tau} \cdot \mathbf{n} = \sigma\kappa$ and $\mathbf{n} \cdot \boldsymbol{\tau} \cdot \mathbf{t} = 0$, where the surface tension σ is assumed to be constant across the whole fluid domain; the mean curvature of the interface κ is known from differential geometry [76] for a body of revolution, $\kappa = \frac{\partial_{zz} h}{(1+(\partial_z h)^2)^{3/2}} - \frac{1}{h\sqrt{1+(\partial_z h)^2}}$; $\boldsymbol{\tau} = \begin{bmatrix} \tau_{rr} & \tau_{rz} \\ \tau_{rz} & \tau_{zz} \end{bmatrix}$ is the fluid stress tensor, and $\boldsymbol{n}$ and $\boldsymbol{t}$ are the unit normal and tangent vectors respectively. In the slender jet approximation [75]: $\mathbf{n} = \frac{1}{\sqrt{1+\partial_z h^2}} \binom{1}{-\partial_z h}$, $\mathbf{t} = \frac{1}{\sqrt{1+\partial_z h^2}} \binom{\partial_z h}{1}$.

The normal stress condition represents the pressure discontinuity due to surface tension at the interface (Young-Laplace law). With these assumptions, it is expressed by:

$$-p+\frac{2\mu}{1+(\partial_z h)^2}[\partial_r u_r-\partial_z h(\partial_r u_z+\partial_z u_r)+(\partial_z h)^2\partial_z u_z]=\sigma\kappa \text{ at } r=h. \quad (4.10)$$

The tangential stress condition expresses the zero shear stress at the interface. It is given by:

$$\frac{\mu}{1+(\partial_z h)^2}[2\partial_r u_r\partial_z h+(\partial_r u_z+\partial_z u_r)(1-(\partial_z h)^2)-2\partial_z h\partial_z u_z]=0 \text{ at } r=h. \quad (4.11)$$

Finally, we have the axis symmetry condition in the velocity field:

$$\partial_r u_z = u_r = 0 \text{ at } r=0. \quad (4.12)$$

The full dynamics of the axisymmetric problem is described by a set of seven coupled equations: 4.6 - 4.12. Following classic dimensional analysis, these equations are made dimensionless through the following scaling: $z, r, h \sim R$; $t \sim \frac{R^2}{\nu}$; $u_z, u_r \sim \frac{\nu}{R}$; $p \sim \frac{\rho\nu^2}{R^2}$. This process leads to a system of non-dimensional nonlinear partial differential equations:

$$\partial_r u_r+\frac{u_r}{r}+\partial_z u_z=0 \quad (4.13)$$

$$\partial_t u_z+u_r\partial_r u_z+u_z\partial_z u_z=-\partial_z p+\partial_{rr}u_z+\partial_{zz}u_z+\frac{1}{r}\partial_r u_z \quad (4.14)$$

$$\partial_t u_r+u_r\partial_r u_r+u_z\partial_z u_r=-\partial_r p+\partial_{rr}u_r+\partial_{zz}u_r+\frac{1}{r}\partial_r u_r-\frac{u_r}{r^2} \quad (4.15)$$

$$\partial_t h-u_r+u_z\partial_z h=0 \text{ at } r=1 \quad (4.16)$$

$$\begin{aligned}&-p+\frac{2}{1+(\partial_z h)^2}[\partial_r u_r-\partial_z h(\partial_r u_z+\partial_z u_r)+(\partial_z h)^2\partial_z u_z]=\\&=\mathrm{Oh}^{-2}\left(\frac{\partial_{zz}h}{(1+(\partial_z h)^2)^{3/2}}-\frac{1}{h\sqrt{1+(\partial_z h)^2}}\right) \text{ at } r=1\end{aligned} \quad (4.17)$$

$$\frac{1}{1+(\partial_z h)^2}[2\partial_r u_r \partial_z h + (\partial_r u_z + \partial_z u_r)(1-(\partial_z h)^2) - 2\partial_z h \partial_z u_z] = 0 \text{ at } r = 1 \tag{4.18}$$

$$\partial_r u_z = u_r = 0 \text{ at } r = 0. \tag{4.19}$$

It is remarkable that the phenomenon dynamics is governed by one single dimensionless parameter, the Ohnesorge number: $\text{Oh} = \frac{\mu}{\sqrt{\rho\sigma R}}$. Here, this represents the ratio between viscous and surface tension forces in the characteristic length R of the cylindrical filament.

From this point, the axial component of the velocity u_z will be denoted as u, whereas the radial velocity u_r will be called v: $\mathbf{u} = v\mathbf{e_r} + u\mathbf{e_z}$.

We are interested in the system reaction to small perturbations. For this purpose, we impose small perturbations to a semi-infinite cylinder of radius 1 at rest. Mathematically this corresponds to the following non-dimensional equations ($\epsilon \ll 1$ and u_1, v_1, p_1 and h_1 are the non dimensional perturbations imposed to the axial velocity, radial velocity, pressure and filament radius, respectively; p_0 is the dimensionless inner pressure in the cylinder):

$$u(z,r,t) = \epsilon u_1(z,r,t)$$

$$v(z,r,t) = \epsilon v_1(z,r,t)$$

$$p(z,r,t) = p_0 + \epsilon p_1(z,r,t)$$

$$h(z,t) = 1 + \epsilon h_1(z,t)$$

By substituting these expressions in the continuity and Navier-Stokes equations 4.13 - 4.15 and linearising, we obtain the following set of equations for the flow perturbations:

$$\frac{\partial v_1}{\partial r} + \frac{v_1}{r} + \frac{\partial u_1}{\partial z} = 0 \tag{4.20}$$

$$\frac{\partial u_1}{\partial t} = -\frac{\partial p_1}{\partial z} + \frac{\partial^2 u_1}{\partial r^2} + \frac{\partial^2 u_1}{\partial z^2} + \frac{1}{r}\frac{\partial u_1}{\partial r} \tag{4.21}$$

$$\frac{\partial v_1}{\partial t} = -\frac{\partial p_1}{\partial r} + \frac{\partial^2 v_1}{\partial r^2} + \frac{\partial^2 v_1}{\partial z^2} + \frac{1}{r}\frac{\partial v_1}{\partial r} - \frac{v_1}{r^2}, \tag{4.22}$$

with the following boundary conditions (corresponding to equations 4.16 - 4.19):

$$\frac{\partial h_1}{\partial t} - v_1 = 0 \text{ at } r = 1 \tag{4.23}$$

$$\frac{\partial u_1}{\partial r} + \frac{\partial v_1}{\partial z} = 0 \text{ at } r = 1 \tag{4.24}$$

$$p_0 = \mathrm{Oh}^{-2} \text{ and } -p_1 + 2\frac{\partial v_1}{\partial r} = \mathrm{Oh}^{-2}\frac{\partial^2 h_1}{\partial z^2} \text{ at } r = 1 \tag{4.25}$$

$$\frac{\partial u_1}{\partial r} = v_1 = 0 \text{ at } r = 0. \tag{4.26}$$

Introducing the definition of the velocity potential $\phi(z, r, t)$ and the stream function $\psi(z, r, t)$, the velocity field is $\vec{u} = -\nabla\phi + \nabla \times (\psi\hat{\theta})$. Therefore, we can write the two components of the velocity perturbation as $u_1 = -\frac{\partial \phi_1}{\partial z} + \frac{\partial \psi_1}{\partial r} + \frac{\psi_1}{r}$ and $v_1 = -\frac{\partial \phi_1}{\partial r} - \frac{\partial \psi_1}{\partial z}$. According to this notation, the set of continuity and Navier-Stokes equations become:

$$\frac{\partial \phi_1}{\partial t} = p_1 \tag{4.27}$$

$$\frac{\partial \psi_1}{\partial t} = \nabla^2 \psi_1 \tag{4.28}$$

$$\nabla^2 \phi_1 = 0 \tag{4.29}$$

This system of equations, together with the set of boundary conditions 4.23-4.26, can be solved through the classical path followed by Rayleigh in 1892. This process leads to the complete linearised dispersion relation of a cylinder of viscous liquid under capillary force, corresponding to equation (30) in [34]. This equation is quite complex, its mathematical derivation not trivial, so the complete form of the dispersion relation is not often used. A typical alternative approach is to analyse only the asymptotic solutions of this equation for inviscid or infinitely viscous fluids. Only Chandrasekhar [77] studied the stability of a viscous cylindrical jet deriving a full dispersion relation in 1961. It can be proved that this is equivalent to Rayleigh's equation. As shown recently by Pekker [78], this dispersion relation can be simplified into a less complex form which can be easily tackled numerically. We refer to this form (equivalent to Rayleigh and Chandrasekhar equations) as the complete dispersion relation for an axisymmetric viscous liquid jet under capillary force:

$$(1-\kappa^2)i\kappa\frac{J_1(i\kappa)}{J_0(i\kappa)}\cdot\frac{\tilde{\kappa}^2-\kappa^2}{\tilde{\kappa}^2+\kappa^2}=$$
$$=(\omega t_c)^2-i\kappa^2\omega t_c\mathrm{Oh}\left(1-\frac{J_2(i\kappa)}{J_0(i\kappa)}-\frac{2\kappa\tilde{\kappa}}{\tilde{\kappa}^2+\kappa^2}\cdot\frac{J_1(i\kappa)}{J_1(i\tilde{\kappa})}\cdot\frac{J_0(i\tilde{\kappa})-J_2(i\tilde{\kappa})}{J_0(i\kappa)}\right). \tag{4.30}$$

Here, $\kappa=\frac{2\pi R}{\lambda}$ is the dimensionless wavenumber of the varicose perturbation on the liquid cylinder (λ being the corresponding wavelength and R the unperturbed jet radius), ω the radial frequency (growth rate), $\mathrm{Oh}=\frac{\mu}{\sqrt{\rho\sigma R}}$ the Ohnesorge number (μ, ρ and σ being the viscosity, density and surface tension of the fluid, respectively), $t_c=\sqrt{\frac{\rho R^3}{\sigma}}$ the capillary time, $\tilde{\kappa}^2=\kappa^2\left(1+i\frac{\omega t_c}{\mathrm{Oh}\kappa^2}\right)$, and J_0, J_1 and J_2 are the Bessel functions of zeroth, first and second order, respectively.

4.2.1 Lubrication model

Following the same process of Eggers & Dupont (1994) [73], we can apply a lubrication approximation (thin column of fluid relative to its longitudinal size) to describe the system dynamics: axial variations are considered negligible with respect to the radial ones, as done also for a thin 2D fluid film by Erneux & Davis (1993) [79] for instance.

The lubrication theory presents the important advantage of simplifying the mathematics of the problem keeping capturing its dominant nonlinear effects. In fact, the complete Navier-Stokes system is reduced to a set of equations much simpler than the original initial-value problem. However, these are still quite complex because of their non-linearity: it is still not possible to derive analytical solutions.

In the limit of wavelengths much larger than the filament's radius R, the full problem is reduced to a 1D model, i.e. a set of coupled nonlinear partial differential equations in which each function depends on only one space-variable, the axial coordinate z, apart from the time t. In particular, the equations are the local mass conservation in the fluid cylinder and the local momentum balance along the axial direction z. They are written in terms of two scalar fields: the local radius of the filament $h(z,t)$ and the axial velocity of the flow $u(z,t)$:

$$\partial_t h+u\partial_z h+\frac{1}{2}h\partial_z u=0 \tag{4.31}$$

$$\partial_t u+u\partial_z u=\frac{3\nu}{h^2}\partial_z(h^2\partial_z u)+\frac{\sigma}{\rho}\partial_z\kappa, \tag{4.32}$$

where $\kappa = \frac{\partial_{zz}h}{(1+(\partial_z h)^2)^{3/2}} - \frac{1}{h(1+(\partial_z h)^2)^{1/2}}$. These equations can be reduced to a more compact conservative-flux form:

$$\partial_t(h^2) + \partial_z(h^2 u) = 0 \tag{4.33}$$

$$\partial_t(h^2 u) + \partial_z(h^2 u^2) = \partial_z \left[3\nu h^2 \partial_z u + \frac{\sigma}{\rho} h \left(\frac{h\partial_{zz}h + (\partial_z h)^2 + 1}{(1+(\partial_z h)^2)^{3/2}} \right) \right] \tag{4.34}$$

It should be noted that the full non-linear expression for the capillary term has been included as suggested by Eggers [38]. Equations 4.33 and 4.34 can be made non-dimensional through the following scaling: $z, h \sim R$; $u \sim \sqrt{\frac{\sigma}{\rho R}}$; $t \sim \sqrt{\frac{\rho R^3}{\sigma}}$.

$$\partial_t(h^2) + \partial_z(h^2 u) = 0 \tag{4.35}$$

$$\partial_t(h^2 u) + \partial_z(h^2 u^2) = \partial_z \left[3\mathrm{Oh} \cdot h^2 \partial_z u + h \left(\frac{h\partial_{zz}h + (\partial_z h)^2 + 1}{(1+(\partial_z h)^2)^{3/2}} \right) \right], \tag{4.36}$$

where $\mathrm{Oh} = \frac{\mu}{\sqrt{\rho\sigma R}}$ is the Ohnesorge number. The 1D equations 4.35 and 4.36 are valid in any inertial reference system, so in a fixed reference frame or in a frame moving at a constant speed. In order to set proper boundary conditions, we choose to adopt the Taylor-Culick velocity comoving frame (in the negative z direction). We are interested in the asymptotic expansion of the filament for long times: in this steady state, the Taylor-Culick regime, the rim recedes at a constant speed whose value is the Taylor-Culick velocity $c = \sqrt{\frac{\sigma}{\rho R}}$ (see [44], [45], [47], [13], [10]). In such a limit and in this frame, the center of mass of the rim is at rest and the cylindrical region far from the tip is geometrically unperturbed and advances at a unity influx velocity (in non-dimensional units). These considerations translate into a Dirichlet boundary condition for $z \to -\infty$ (fluid domain far from the tip):

$$\begin{cases} h(z,t) = 1 \\ u(z,t) = 1 \end{cases} \text{ at } z = -\infty. \tag{4.37}$$

At the receding tip $z = z_0(t)$ we need to impose the kinematic condition and geometrical symmetry. This yields the following Cauchy boundary condition:

$$\begin{cases} h(z,t) = 0 \\ \partial_z h(z,t) = -\infty \\ u(z,t) = \partial_t z_0 \end{cases} \text{ at } z = z_0(t). \tag{4.38}$$

4.3 Asymptotic analysis: local solutions

The aim of this section is to derive a long-time asymptotic expression of a semi-infinite filament profile from the lubrication equations 4.35 and 4.36. After a transient state, the retracting filament reaches such a steady regime, in which the rim length scale is much larger than the unperturbed cylinder radius ($R_b(t) \gg R$) and its retracting velocity reaches the Taylor-Culick speed $c = \sqrt{\frac{\sigma}{\rho R}}$. In this infinite-time limit, time derivatives are negligible with respect to spatial ones, which lead the dynamics: the dominant order of $h(z,t)$ and $u(z,t)$ is supposed to be only space-dependent.

The fluid domain presents different zones with distinct natural length scales: a steady filament section, a growing spherical rim, and an intermediate matching region. The different solutions are matched together in space to derive a unique function representing the whole domain solution at the leading order.

4.3.1 Steady filament

The steady region far away from the blob is supposed to be unperturbed during the rim retraction. We assume the following form for the filament dimensionless radius and the axial velocity:

$$h_f(z,t) = h_f^{(0)}(z) + h_f^{(1)}(z,t) + \dots, \tag{4.39}$$

$$u_f(z,t) = u_f^{(0)}(z) + u_f^{(1)}(z,t) + \dots, \tag{4.40}$$

where $h_f^{(1)}(z,t)$ and $u_f^{(1)}(z,t)$ are assumed small higher-order corrections that vanish as $t \to \infty$ with respect to the dominant terms $h_f^{(0)}(z)$ and $u_f^{(0)}(z)$. By replacing these expressions in the set of equations 4.35 and 4.36, we obtain at the leading order:

$$\partial_z\left(h^2 u\right) = 0, \tag{4.41}$$

$$\partial_z\left(h^2 u^2\right) = \partial_z\left(3\mathrm{Oh}\, h^2 \partial_z u + h\left[\frac{1+(\partial_z h)^2 + h\partial_{zz}h}{\sqrt{1+(\partial_z h)^2}^3}\right]\right), \tag{4.42}$$

where $h \equiv h_f^{(0)}(z)$ and $u \equiv u_f^{(0)}(z)$ for simplicity of notation. By integrating equation 4.41 between $z = -\infty$ and z taking into account the boundary conditions 4.37, we obtain a relation between u and h: $u = h^{-2}$. This expression is then substituted in equation 4.42. Integration of the latter between $z = -\infty$ and z leads to the following second-order ordinary differential equation in $h(z)$:

$$\frac{1+6\mathrm{Oh}\cdot h\partial_z h}{h^3}=\frac{1+(\partial_z h)^2+h\partial_{zz}h}{\sqrt{1+(\partial_z h)^2}^3}. \tag{4.43}$$

The ODE 4.43 can only be integrated numerically (in the present work, numerical integration of this kind of equations is performed implicitly through the software Maple$^{\mathrm{TM}}$). However, some of its properties can be studied analytically. First, as expected, it is invariant under translations in the z-axis: if $h(z)$ is a solution, also $h(z-z_0)$ is a solution $\forall z_0$. Second, numerical solutions obtained by varying the initial conditions ($h(z_0)$ and $\partial_z h\mid_{z=z_0}$, once $z_0=0$ and $\mathrm{Oh}=0.1$ have been set) are shown in figure 4.4, which represents the phase plot of the ODE 4.43. It is evident that two different families of solutions exist: both of them group curves that present a singularity as they diverge at finite z values. The first group are interfaces with a positive infinite slope; the second present a negative infinite slope. The fact that these divergent solutions appear is natural: boundary conditions 4.37 imply a net flux of mass into the domain, thus finite functions would not comply mass conservation. In fact, in the asymptotic steady state, finite solutions of equations 4.35 and 4.36 cannot exist and be well-defined in the whole domain.

From figure 4.4 it is essential to note that there exists only a single curve which does not present any singularity at finite z, but it only diverges for $z\to\infty$. We call this solution "separatrix" since it separates the two different families of singular functions. The separatrix is extremely important as it is the only theoretical solution that complies mass conservation at the long-time asymptotic limit (it diverges for $z\to\infty$, thus it corresponds to an infinite mass rim) and it is well-posed in all the domain. For this reason, in the steady limit, the separatrix should fit the physical filament profile.

We follow a simple argument in order to determine the analytic expansion of the separatrix around $z\to\infty$, the one to be matched to the growing blob. Its leading order can be found by taking into account its divergence for $z\to\infty$. At this limit, $\partial_z h\gg 1$ is a dominant term in equation 4.43, i.e. we can neglect lower orders. This yields a simple balance between the viscous and the surface-tension terms:

$$6\mathrm{Oh}\frac{\partial_z h}{h^2}=\frac{h\partial_{zz}h+(\partial_z h)^2}{(\partial_z h)^3}$$

Multiplying both sides by $\frac{1}{h^3}$, we get:

$$6\mathrm{Oh}\frac{\partial_z h}{h^5}=\frac{\partial_z(h\partial_z h)}{(h\partial_z h)^3}$$

The last equation can be integrated in z yielding:

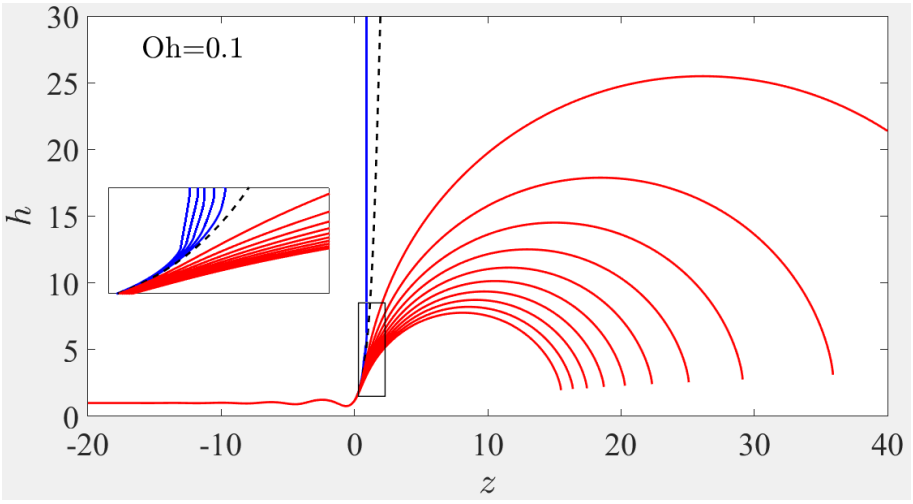

Figure 4.4: *The two families of singular solutions of equation 4.43 are obtained through numerical integration by choosing different initial conditions (here, $z_0 = 0$ and $Oh = 0.1$). Both families develop derivative singularities for finite z but different sign diverging slopes: the upper left family (blue curves) for positive and the lower right family (red curves) for negative. The separatrix (dashed black curve) is the unique function that can be defined in the whole domain.*

$$-\frac{3}{2}\mathrm{Oh}\cdot h^{-4} = -\frac{1}{2}(h\partial_z h)^{-2} + K,$$

where K is a constant of integration. From numerical integration of equation 4.43 and referring to the condition of divergence only at $z \to \infty$, it can be shown that the separatrix corresponds to the case $K = 0$. In fact, for $K \neq 0$, singular solutions are obtained (depending on the sign of K, the two different families arise). Setting $K = 0$ and after some basic algebra steps, the last expression yields:

$$\frac{\partial_z h}{h} = \frac{1}{\sqrt{3\mathrm{Oh}}}$$

This equation is then integrated in z, leading to:

$$h = e^{\frac{z-z_0}{\sqrt{3\mathrm{Oh}}}},$$

where z_0 is a translational invariance constant. As seen, the filament interface $h(z)$ has an exponential behavior. Its expression can be expanded around $z \to \infty$. We assume the form $h(z) = h_0(z) + Bh_1(z)$, where $h_0(z) = e^{\frac{z-z_0}{\sqrt{3\mathrm{Oh}}}}$ is the leading order expression derived through the above argument and $Bh_1(z)$ is a second order correction (B being a constant coefficient). By plugging this expression in equation 4.43 and linearising, we obtain $h_1(z) = e^{-\frac{z-z_0}{\sqrt{3\mathrm{Oh}}}}$. Therefore,

the separatrix expansion around $z \to \infty$ up to the second order is:

$$\lim_{z\to\infty} h_f^{(0)}(z) = e^{\frac{z-z_0}{\sqrt{3\mathrm{Oh}}}} + Be^{-\frac{z-z_0}{\sqrt{3\mathrm{Oh}}}}.$$

It should be noted that the solution convergence is fast as the second order correction, $\mathcal{O}(e^{-z})$, is much smaller than the leading order, $\mathcal{O}(e^{z})$: $h_1(z)/h_0(z) = \mathcal{O}(e^{-2z})$. For this reason, we do not explore any further correction terms. By combining the expression $h(z) = e^{\frac{z-z_0}{\sqrt{3\mathrm{Oh}}}} + Be^{-\frac{z-z_0}{\sqrt{3\mathrm{Oh}}}}$ with the ODE 4.43 and linearising, the value of the coefficient B is derived: $B = \frac{1}{12\sqrt{3\mathrm{Oh}}} + \frac{1}{2}\mathrm{Oh}$. Thus, the analytic expansion of the separatrix $h_f^{(0)}(z)$ around $z \to \infty$ is:

$$\lim_{z\to\infty} h_f^{(0)}(z) = e^{\frac{z-z_0}{\sqrt{3\mathrm{Oh}}}} + \left(\frac{1}{12\sqrt{3\mathrm{Oh}}} + \frac{1}{2}\mathrm{Oh}\right) e^{-\frac{z-z_0}{\sqrt{3\mathrm{Oh}}}} \tag{4.44}$$

A set of these solutions, obtained through numerical integration of equation 4.43 at different Ohnesorge numbers, is shown in figure 4.5. Depending on the *Oh* value, this region is either featured by decaying ripples (capillary waves) or a smooth spatial decay. These features are further analysed in section 4.4.2.

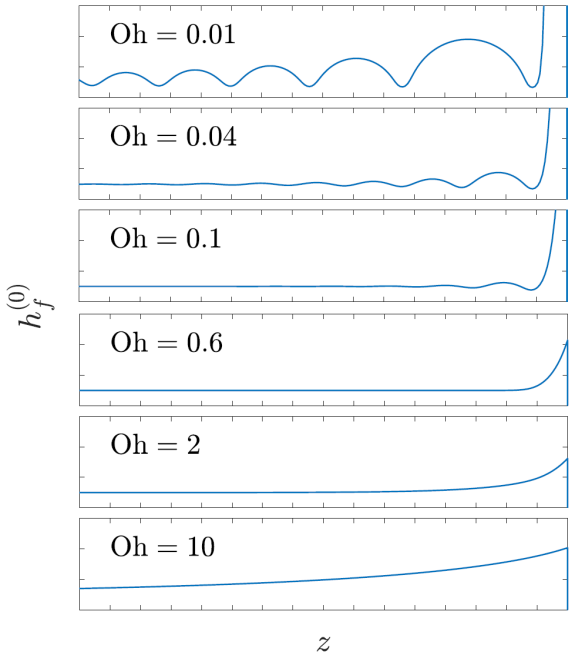

Figure 4.5: *Numerical solutions for the profile of the steady filament region via equation 4.43 with $z_0 = 0$ at different Ohnesorge numbers. The distance between ticks is 2R. As Oh grows, solutions show slow decaying ripples ($Oh = 0.01$), fast decaying ripples ($Oh = 0.1$), fast smooth decay ($Oh = 0.6$) and slow smooth decay ($Oh = 10.0$). As explained in section 4.4.2, oscillations appear for $Oh < Oh^* = 3^{-\frac{1}{2}}$. At the $z \to \infty$ limit, the solution shows the exponential behaviour of equation 4.44, with steeper growths for small Oh numbers.*

4.3.2 Growing blob

The blob region has a different natural length scale, its radius $R_b(t)$ which depends on time and scales as $t^{1/3}$ (see section 4.1). In the steady regime, $R_b(t) \gg 1$. Additionally, the solution in this region should fit the constant mass influx quantity $h^2u = 1$. Consequently, we choose the following quasi self-similar ansatz:

$$h_b(z,t) = R_b\left[h_b^{(0)}(\zeta) + h_b^{(1)}(\zeta,t) + \ldots\right], \tag{4.45}$$

$$u_b(z,t) = R_b^{-2}\left[u_b^{(0)}(\zeta) + u_b^{(1)}(\zeta,t) + \ldots\right], \tag{4.46}$$

where the variable ζ is set as $\zeta \equiv R_b^{-1}z$. Also in this case, $h_b^{(1)}(\zeta,t)$ and $u_b^{(1)}(\zeta,t)$ are supposed small higher-order corrections in t of the leading order terms, and the equations in the physical variables z and t are invariant with respect to any Galilean transformation. By replacing these forms in equations 4.35 and 4.36, we obtain at the leading order:

$$2R_b^2\dot{R}_b h^2 - 2R_b^2\dot{R}_b\zeta h\partial_\zeta h + \partial_\zeta\left(h^2u\right) = 0, \tag{4.47}$$

$$\partial_\zeta\left(\frac{1+(\partial_\zeta h)^2 + h\partial_{\zeta\zeta}h}{\sqrt{1+(\partial_\zeta h)^2}^3}\right) = 0, \tag{4.48}$$

where $\dot{R}_b \equiv \partial_t R_b$, $h \equiv h_b^{(0)}(\zeta)$ and $u \equiv u_b^{(0)}(\zeta)$. Equations 4.47 and 4.48 are uncoupled. Equation 4.47 (mass conservation) depends on the term $R_b^2\dot{R}_b$: it is well-posed and has physical solution only if $R_b^2\dot{R}_b = \mathcal{O}(1)$. Equation 4.48 (momentum balance along the axial direction) can be trivially solved by the mathematical identity $\int h\partial_\zeta\kappa \mathrm{d}\zeta = \frac{1+(\partial_\zeta h)^2+h\partial_{\zeta\zeta}h}{\sqrt{1+(\partial_\zeta h)^2}^3}$ [74]:

$$h\partial_\zeta\kappa = 0 \Rightarrow \partial_\zeta\kappa = 0 \Rightarrow \kappa = \Theta,$$

where Θ is a constant. Hence, the solution $h(\zeta)$ has a constant curvature, i.e. it is a circle (a sphere in the 3D axisymmetric configuration). In self-similar variables, setting the radius as 1 and the origin at the left tip of the semicircle (i.e. the center at $(1,0)$), the solution is given by:

$$h(\zeta) = \sqrt{2\zeta - \zeta^2}. \tag{4.49}$$

By replacing this solution in equation 4.47, and imposing a null flux $h^2u = 0$ at the right tip ($\zeta = 2$), it yields a condition for the time-dependent blob radius $R_b(t)$, i.e. $R_b^2\dot{R}_b = 1/4$. Importantly, this condition is identical to the classical

Taylor-Culick argument (i.e. mass conservation) that balances the growth of the blob volume and the volume of fluid collected from the filament (equation 4.2), providing the exact power law for $R_b(t)$ (equation 4.3). Hence, in the long-time asymptotic limit, the radius of the blob grows as $R_b(t) = \left(1 + \frac{3}{4}t\right)^{1/3}$. In fact, this result is in agreement with the condition $R_b^2 \dot{R}_b = 1/4$ ($\mathcal{O}(1)$), which naturally implies $R_b \propto t^{1/3}$.

In terms of the physical variables z and t, the blob shape is:

$$h_b^{(0)}(z,t) = \sqrt{2R_b(t)\, z - z^2}, \tag{4.50}$$

where $h_b^{(0)}(z,t) \equiv R_b h_b^0(\zeta)$. This function models the growing blob dynamics and it has a spherical shape. It is defined in the domain $0 \leq z \leq 2R_b(t)$. However, it is singular at the left limit, for $z \to 0$: here, it does not match the physical solution, where it should connect to the steady filament region. The blob analytic expansion around $z \to 0$ is given by:

$$\lim_{z \to 0^+} h_b^{(0)}(z,t) = \alpha t^{1/6} z^{1/2} + \mathcal{O}\left(t^{-1/6} z^{3/2}\right). \tag{4.51}$$

The constant α can be found by imposing the mass influx into the blob $h^2 u = 1$ as a boundary condition at $z = 0$. Straightforward calculations lead to $\alpha = 6^{1/6}$.

Finally, we remark that the blob dynamics, in the asymptotic limit, is completely independent from viscosity, as evidenced by the momentum equation 4.48. Physically, the enlargement of the spatial scales in the growing blob slows the flow into a quasi-steady state that leads to the rise of surface tension as the unique dominant force.

4.3.3 Intermediate matching zone

It should be noted that the steady filament and the growing blob solutions obtained in the previous sections are analytically different. Hence, it is necessary to introduce an intermediate zone which can match the two leading-order expansions assuring the continuity of a unique solution valid in the whole domain. At the leading order, the profile of this intermediate region has to fit both the steady filament solution ($h \propto \mathrm{e}^{\frac{z}{\sqrt{3\mathrm{Oh}}}}$) for $z \to -\infty$, and the blob shape ($h \propto t^{1/6} z^{1/2}$) for $z \to \infty$. Provided that the flux $h^2 u = 1$ is conserved across the region, we set a self-similar ansatz of this form: $h(z,t) = t^a f\left(\frac{z}{t^b}\right)$. The matching conditions $a - \frac{1}{2}b = \frac{1}{6}$ and $b = 0$ lead to $a = \frac{1}{6}$. Therefore, the self-similar scaling which fulfils these requirements is the following:

$$h_m(z,t) = t^{1/6}\left[h_m^{(0)}(\xi) + h_m^{(1)}(\xi,t) + \ldots\right], \tag{4.52}$$

$$u_m(z,t) = t^{-1/3}\left[u_m^{(0)}(\xi) + u_m^{(1)}(\xi,t) + \ldots\right], \tag{4.53}$$

where $\xi \equiv z$ is merely a spatial variable, and $h_m^{(1)}(\xi,t)$ and $u_m^{(1)}(\xi,t)$ are small higher-order corrections in t of the leading order terms $h_m^{(0)}(\xi)$ and $u_m^{(0)}(\xi)$. Combining these expressions with the lubrication model (equations 4.35 and 4.36), we obtain at the leading order:

$$\partial_\xi\left(h^2 u\right) = 0, \tag{4.54}$$

$$\partial_\xi\left[h\left(\frac{\left(\partial_\xi h^2\right) + h\partial_{\xi\xi}h}{\left(\partial_\xi h\right)^3}\right)\right] + 3\mathrm{Oh}\partial_\xi\left(h^2\partial_\xi u\right) = 0, \tag{4.55}$$

where $h \equiv h_m^{(0)}(\xi)$ and $u \equiv u_m^{(0)}(\xi)$. Equation 4.54 can easily be integrated by taking the flux boundary condition $h^2 u \mid_{\xi=-\infty} = 1$ arising from the matching with the steady-filament region. This yields $u = h^{-2}$, which is then plugged into equation 4.55 to obtain the following ODE in $h(\xi)$:

$$6\mathrm{Oh}\left(\partial_\xi h\right)^4 = h^2\left[\left(\partial_\xi h\right)^2 + h\partial_{\xi\xi}h\right]. \tag{4.56}$$

This ordinary differential equation is numerically integrated imposing a matching boundary condition with the growing blob region, i.e. $h \propto \xi^{1/2}$ at $\xi \to \infty$ (the constant of integration is zero). The result is then integrated once again, yielding the solution in an implicit form:

$$h(\xi) = \alpha\left(\frac{3}{4}\mathrm{Oh}\right)^{1/4} H\left(\Xi \equiv \frac{2\xi}{\sqrt{3\mathrm{Oh}}}\right), \tag{4.57}$$

where α is a constant and H is given implicitly by the function Ξ:

$$\Xi = \sqrt{H^4+1} - \arctan\left(\frac{1}{\sqrt{H^4+1}}\right).$$

By expanding the obtained function 4.57 into its two corresponding limits, we obtain:

$$\lim_{z\to-\infty} h_m^{(0)}(z,t) = qt^{1/6}\mathrm{e}^{\frac{z}{\sqrt{3\mathrm{Oh}}}} + \mathcal{O}\left(t^{1/6}\mathrm{e}^{\frac{5z}{\sqrt{3\mathrm{Oh}}}}\right), \tag{4.58}$$

$$\lim_{z\to+\infty} h_m^{(0)}(z,t) = \alpha t^{1/6} z^{1/2} + \mathcal{O}\left(t^{1/6} z^{-3/2}\right), \tag{4.59}$$

where $h_m^{(0)}(z,t) \equiv t^{1/6} h_m^0(\xi)$ and $q \equiv \alpha \left(3\mathrm{e}^{-2}\mathrm{Oh}\right)^{1/4}$. The expansions have already been written in terms of the original physical variables z and t.

We point out that the intermediate matching region arises from a balance between viscous and capillary forces, as shown by equation 4.55. Nonetheless, as the filament becomes thicker, the capillary force overcomes viscosity leading to a viscosity-independent behaviour, suitable to be matched with the blob.

4.4 The evolving shape of a filament

4.4.1 Asymptotic matching solution

By matching the intermediate region expansions, equations 4.58 and 4.59, with the steady-filament and blob solutions, equations 4.44 and 4.51, the coefficients α and z_0 are set: $\alpha = 6^{1/6}$ and $z_0 = -\sqrt{3\mathrm{Oh}} \ln\left(qt^{1/6}\right)$. It is important to notice that the slow dependence of z_0 on time only modifies higher-order equations for the steady-filament profile $h_f(z,t)$, leaving the leading-order equations 4.41 and 4.42 unaffected.

Hence, the leading-order solution for a capillary retracting filament profile that satisfies the lubrication model (equations 4.35 and 4.36) with the proper boundary conditions (equations 4.37 and 4.38) is:

$$h^{(0)}(z,t) = h_f^{(0)}(z) + t^{1/6} h_m^{(0)}(z) + t^{1/3} h_b^{(0)}\left(zt^{-1/3}\right) - qt^{1/6}\mathrm{e}^{\frac{z}{\sqrt{3\mathrm{Oh}}}} - \alpha t^{1/6} z^{1/2}. \tag{4.60}$$

Figure 4.6 shows an example of the profile solution 4.60 for a given time, $t = t_* = 20$ (in dimensionless units); local solutions and asymptotic matched limits are also included.

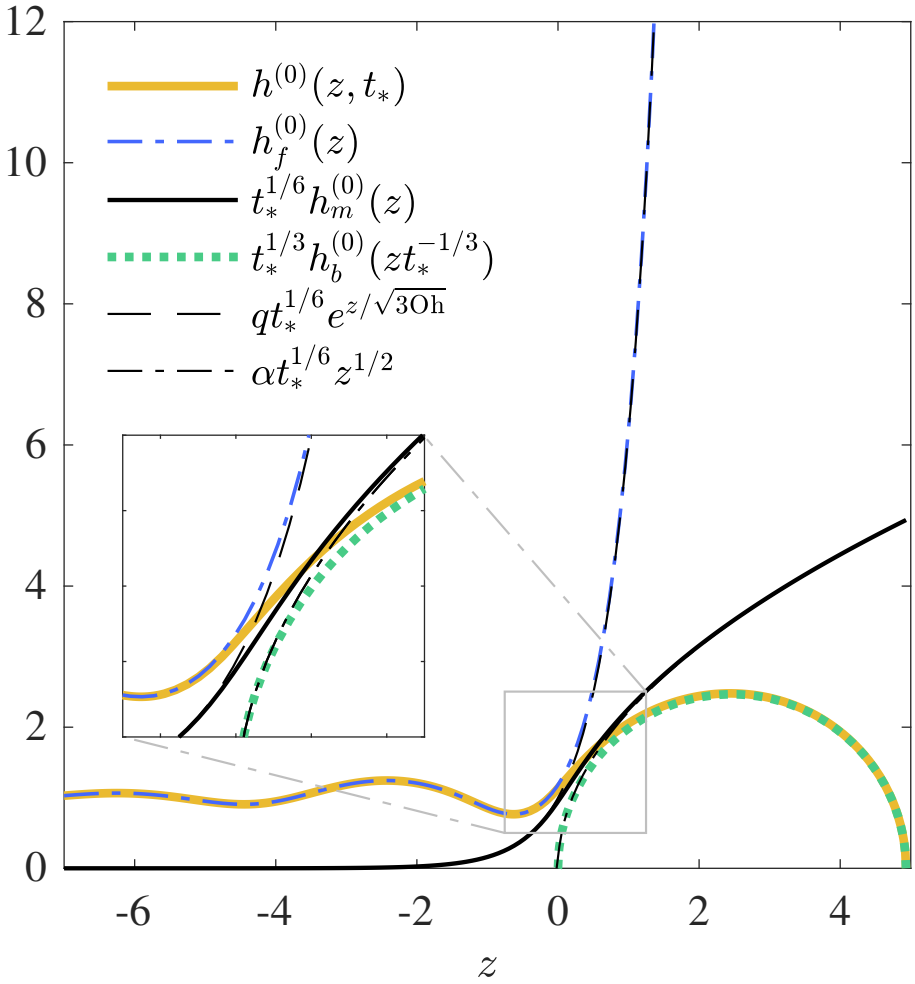

Figure 4.6: *Asymptotic matching solution (yellow line) for a capillary retracting filament with* $Oh = 0.1$ *at* $t = t_* = 20$ *in dimensionless units. Local solutions of the steady filament, the intermediate and circular blob regions, and the asymptotic tails beyond the matched regions are also shown.*

Temporal evolution of some filament profiles with different Ohnesorge numbers, based on the solution of equation 4.60, are depicted in figure 4.7.

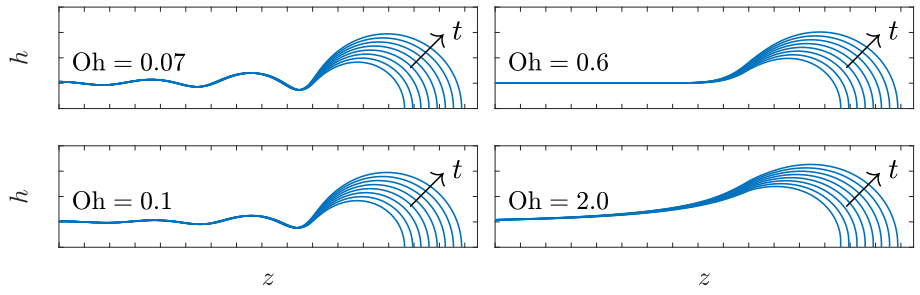

Figure 4.7: *Temporal evolution of filament profiles with different Ohnesorge numbers ($Oh = 0.07$, $Oh = 0.1$, $Oh = 0.6$ and $Oh = 2.0$) in a Taylor-Culick velocity frame of reference. Curves are obtained following the asymptotic matching approach of equation 4.60. Here, the tick distance is equal to R.*

So far, we have focused on the filament profile $h(z,t)$. However, leading-order expressions for the velocity $u(z,t)$ can be derived under the same framework arising from the lubrication model (equations 4.35 and 4.36): in particular, as previously shown, the velocity field in the steady filament and intermediate regions is $u = h^{-2}$, while it can be easily derived from equation 4.47 in the blob zone. Consequently, the leading-order expression for the pressure field inside the filament can be directly obtained via the formalism of Eggers & Dupont (p_0 of equation (13) in [73]). Figure 4.8 is a 3D plot of three recoiling filaments with different Ohnesorge numbers at $t = 33.8$ (in dimensionless units): velocity profiles are represented by black solid lines, whereas the pressure field is shown as a colour scheme.

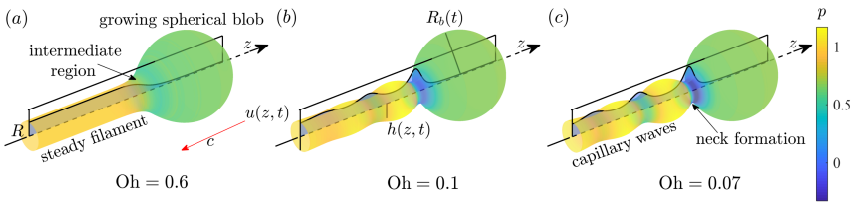

Figure 4.8: *Capillary retracting filaments at $t = 33.8$ with (a) $Oh = 0.6$, (b) $Oh = 0.1$, and (c) $Oh = 0.07$. The time t is scaled by the capillary time $t_c = \sqrt{\rho R^3/\sigma}$. Asymptotic solutions of the filament profile, $h(z,t)$, are obtained through the lubrication model (equations 4.35 and 4.36). Velocity profiles $u(z,t)$ (black solid lines) and pressure p (colour scheme) are also displayed.*

4.4.2 Capillary waves: wavelength and decay length

The recoiling filament solution features travelling capillary waves that escape from the growing blob at the Taylor-Culick velocity. Hence, in the Taylor-Culick comoving frame of reference, the capillary waves are steady and the filament profile far away from the receding tip can be approximated by $h_f^{(0)}(z) \approx 1 + \epsilon e^{-\mathrm{i}kz}$, with $\epsilon \ll 1$. Combining this expression with the ODE obtained in the steady-filament section (equation 4.43) and linearising, leads to the following capillary wavenumber:

$$k = 3\mathrm{iOh} \pm \sqrt{3 - 9\mathrm{Oh}^2}. \tag{4.61}$$

Depending on the Ohnesorge value, the capillary wavenumber k can be complex or purely imaginary. The critical threshold is $\mathrm{Oh}^* = 3^{-\frac{1}{2}} \approx 0.577$. For $\mathrm{Oh} \geq \mathrm{Oh}^*$, the wavenumber k is strictly imaginary and thus the filament profile is stable and features a monotonic exponential decay as $z \to -\infty$. In contrast, for $\mathrm{Oh} < \mathrm{Oh}^*$, k has also a real component and the filament develops the well-known spatial oscillations (capillary waves) modulated by the exponential decay.

It is interesting to analyse the wavelength of these capillary ripples, which is a function of the real part of k. In particular, it is given (in dimensionless units) by: $\lambda = \frac{2\pi}{\Re(k)}$. Thus, at the inviscid limit, the asymptotic dimensionless wavelength of the capillary waves takes the value:

$$\lim_{\mathrm{Oh}\to 0} \lambda = \frac{2\pi}{\sqrt{3}} \approx 3.63. \tag{4.62}$$

The linear analysis also reveals the spatial decay length as a function of the imaginary part of k: in dimensionless units, $\ell = \frac{1}{\Im(k)}$. Thus, the decay length scales as $(3\mathrm{Oh})^{-1}$ at the inviscid limit, and as $(2\mathrm{Oh})$ for $\mathrm{Oh} \to \infty$.

We point out that these results come from a linearised lubrication approximation. Additionally, we consider the linear dispersion relation of the full Navier-Stokes equations from the work of Rayleigh [34] and analyse waves whose phase velocity, ω/k, is equal to the Taylor-Culick speed given in equation 4.1. This is equivalent to impose $\omega t_c = \kappa$ in equation 4.30 and solve it numerically, finding the complex roots κ; then, the wavelength λ and decay length ℓ are derived from the obtained capillary wavenumber as previously explained. Figure 4.9 shows the wavelength and decay length as functions of the Ohnesorge number, arising from both the lubrication approximation (solid lines) and the dispersion relation derived from the full Navier-Stokes equations (dashed lines). The qualitative agreement between the lubrication model and the full Navier-Stokes equations (both models are linearised) is remarkably good, show-

ing similar thresholds and asymptotic limits. Furthermore, the agreement is quantitatively excellent for Oh > 1.

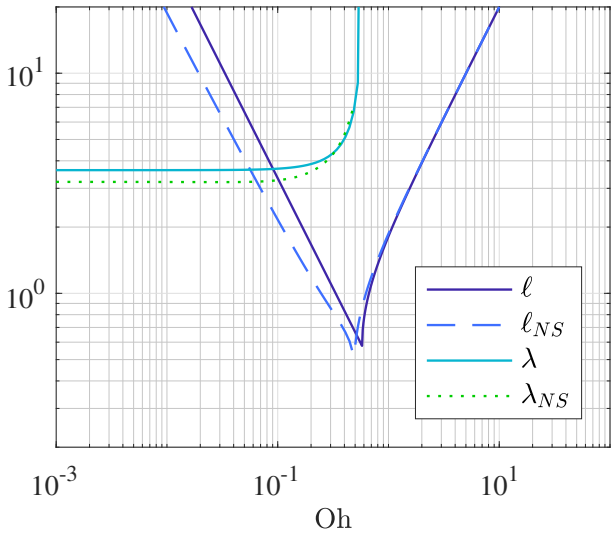

Figure 4.9: *Wavelength λ and decay length ℓ as functions of the Ohnesorge number Oh. The asymptotic solutions of lubrication equations are shown as solid lines, whereas the solutions obtained from linearisation of full Navier-Stokes equations are shown as dashed lines.*

4.4.3 Neck thickness

A direct consequence of the existence of the spatial oscillations (capillary waves) on the filament profile is the appearance of the *neck*, i.e. a finite global minimum of the function $h(z)$, $h_{\min}$, right behind the blob (see figure 4.10).

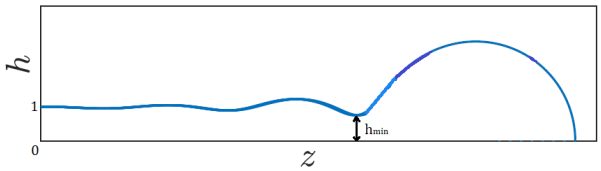

Figure 4.10: *Appearance of the neck, h_{min}, behind the blob.*

Figure 4.11 shows the filament neck thickness $h_{\min}$ as a function of the Ohnesorge number. This result is derived by identifying the function value at the global minimum of the solution of equation 4.43, obtained through numerical integration, for different Ohnesorge numbers. The plot shows that at the zero Ohnesorge limit, $h_{\min}$ converges to a finite value.

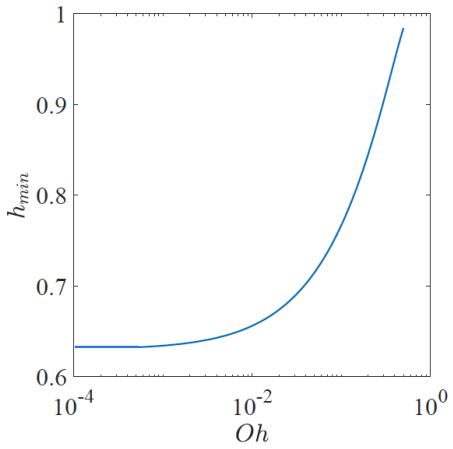

Figure 4.11: *Neck thickness h_{min} as a function of the Ohnesorge number Oh.*

We focus our attention on the inviscid limit. By setting $Oh = 0$ in equation 4.43, we obtain:

$$\frac{1}{h^3} = \frac{1 + (\partial_z h)^2 + h\partial_{zz} h}{\sqrt{1 + (\partial_z h)^2}^3}$$

Multiplying both sides by $\frac{\partial_z h}{h^2}$, it yields:

$$\frac{\partial_z h}{h^5} = \frac{\partial_z h + (\partial_z h)^3 + h\partial_z h\partial_{zz} h}{h^2\sqrt{1 + (\partial_z h)^2}^3}$$

Integrating the last equation along z using the boundary condition $h \to \infty$ as $z \to \infty$, the result yields:

$$4h^3 = \sqrt{1 + (\partial_z h)^2}.$$

Since we are interested in the neck, which is a stationary point of $h(z)$, we set $\partial_z h = 0$. Thus, we obtain an equation for the neck, $4h_{min}^3 = 1$, whose solution is:

$$\lim_{\mathrm{Oh}\to 0} h_{min} = 4^{-\frac{1}{3}} \approx 0.63. \tag{4.63}$$

The obtained value correctly matches the result shown in figure 4.11.

It is important to note that the long-time asymptotic expansion of the filament profile does not display any critical Ohnesorge value at which $h_{\min} \to 0$ (i.e. breakup), which is contrary to what is seen in nature and numerical simulations. Indeed, this suggests that filament pinch-off occurs through a dynamic instability during the transient unsteady state, which cannot be captured by our asymptotic steady model.

4.5 Validation

We validate our theoretical model through comparison with numerical simulations. Numerical integration of the set of full 3D axisymmetric incompressible Navier-Stokes equations 4.4 and 4.5 is performed for both phases using the flow solver Basilisk [15] [11] [12]. This solver uses adaptive mesh refinement based on octree decomposition and interface tracking with the volume of fluid (VoF) method. The combination of both techniques allows efficient computation of complex interfacial flows [80]. The mesh refinement is controlled by the interface velocity and the vorticity field: this way, a good resolution is kept both around the interface and in the high-vorticity region. The initial configuration is shown in figure 4.12: it consists of a rectangular domain containing a semi-infinite free liquid cylinder of radius R surrounded by a passive gas (air). The simulations are executed in a comoving frame of reference receding at the Taylor-Culick speed. Dirichlet boundary conditions for the velocity field are set on the left boundary, while outlet conditions are imposed on the other sides of the domain. All variables are non-dimensionalised with respect to the filament radius R and the liquid properties. We consider a water filament retracting in the air by setting the density and viscosity ratios to $\rho_L/\rho_G = 820$ and $\mu_L/\mu_G = 55$, respectively.

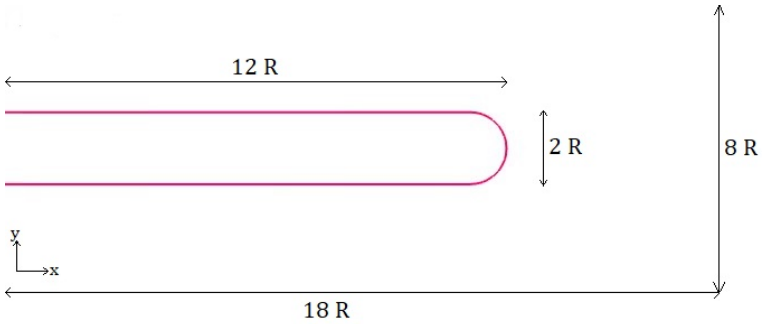

Figure 4.12: *Spatial domain and initial configuration of the numerical simulation performed by the flow solver Basilisk [15]. The recoiling filament has radius R and initial length $12R$. The domain consists of a rectangular box $18R \times 8R$.*

Simulations are run up to the asymptotic steady state in which the filament profile behind the blob remains quasi-stationary (Taylor-Culick regime). In fact, the simulation time is set as $t_{end} = 200t_v$, where $t_v = \frac{\mu R}{\sigma}$ is the characteristic viscous time scale, in order to overpass the transient regime [13]. Recoiling filaments are simulated at several Oh values lying in the range $0.1 \leq \text{Oh} \leq 2.0$. For $\text{Oh} > \text{Oh}^*$, the spatial decay length behind the blob is estimated by using an exponential fitting. For $\text{Oh} \leq \text{Oh}^*$, the wavelength of the capillary ripples, the

decay length and the neck thickness are derived from the profile local maxima and minima behind the blob.

As an example, the following figures show the results obtained through the Basilisk numerical simulation related to the case Oh = 0.1. In figure 4.13 the filament profile is depicted for different instants. Figure 4.14 shows the filament profile at $t = 20t_c$, i.e. t_{end} of the simulation: the data of interest (wavelength, decay length and neck thickness) can be "manually" measured from this plot.

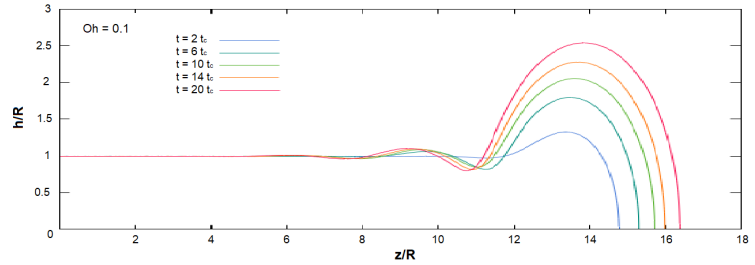

Figure 4.13: *Basilisk simulation, Oh = 0.1: temporal evolution of the filament profile (time is made dimensionless by the capillary time).*

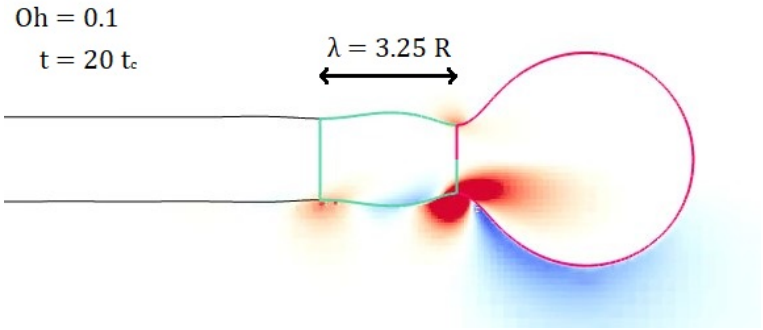

Figure 4.14: *Basilisk simulation, Oh = 0.1: filament profile at $t = 20t_c$. The wavelength of the capillary ripples escaping the blob can be measured as the horizontal distance between the neck section and the next local minimum. In this case, $\lambda = 3.25R$. Additionally, the vorticity field is shown as a colour scheme.*

Figures 4.15-4.17 show the wavelength of the capillary waves, the spatial decay length and the neck thickness in terms of time (in dimensionless units). These functions are automatically computed by the flow solver. In fact, the curves converge to stable values within $t_{end} = 20t_c$. This assures that the simulation has reached the asymptotic steady state, i.e. the Taylor-Culick regime. In this particular case, Oh = 0.1, the results obtained by the numerical simulation are $\lambda \approx 3.25R$, $\ell \approx 2R$, and $h_{\min} \approx 0.85R$, which are well in agreement with our predictions discussed in the previous section.

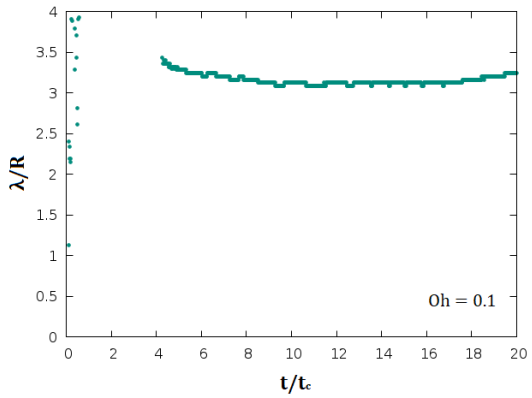

Figure 4.15: *Basilisk simulation, Oh = 0.1: dimensionless wavelength as a function of dimensionless time.*

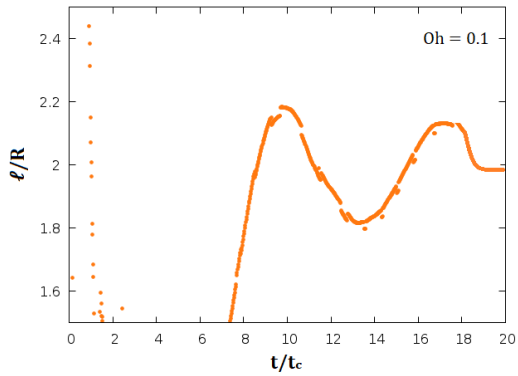

Figure 4.16: *Basilisk simulation, Oh = 0.1: dimensionless decay length as a function of dimensionless time.*

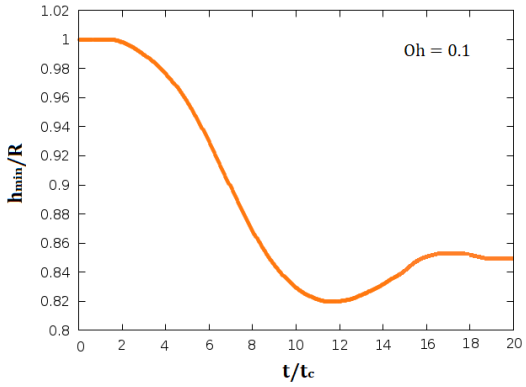

Figure 4.17: *Basilisk simulation, Oh = 0.1: dimensionless neck thickness as a function of dimensionless time.*

Additionally, we provide a comparison between our theoretical results and existing data in the literature. In particular, we consider the work of Notz & Basaran [8] in which simulations of long liquid filaments were performed at Oh = 0.001, 0.01, 0.1, and 1.0. Capillary waves were observed for all the cases except for Oh = 1.0, implying that the critical threshold lies in the range of $0.1 < \mathrm{Oh}^* < 1.0$, which is consistent with our value of $\mathrm{Oh}^* \approx 0.577$. The filament profiles from Notz & Basaran [8] are examined by image analysis and shown in figure 4.18. The measured capillary wavelengths range from $2.8R$ to $3.1R$. In fact, $\lambda = (2.96 \pm 0.15)R$ for Oh = 0.001, which is of the same order as our predicted inviscid value $\lambda_{\mathrm{Oh}=0} \approx 3.6R$.

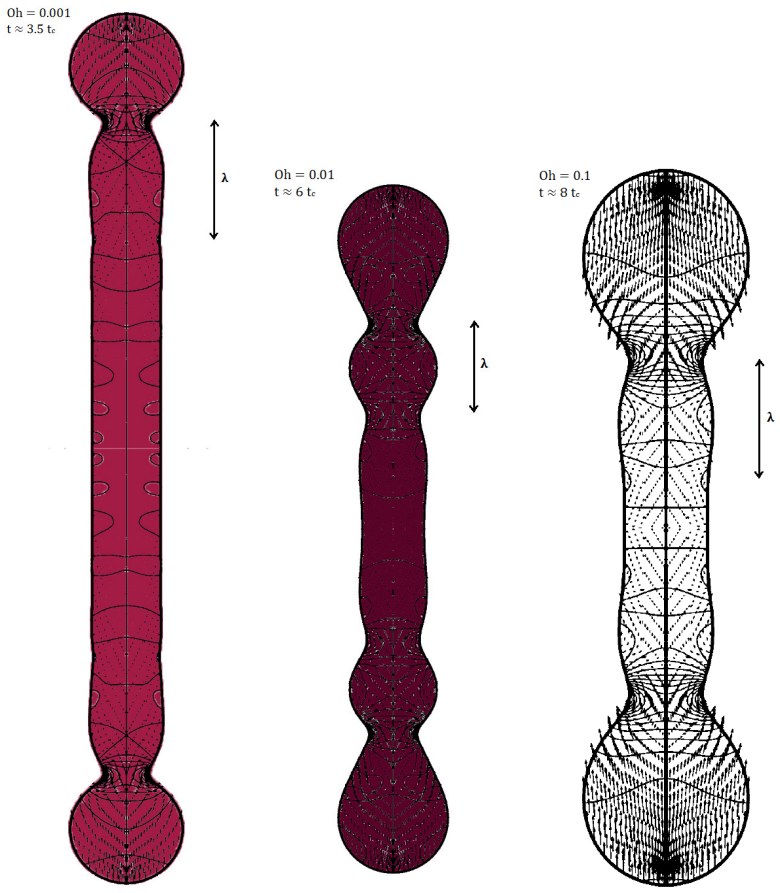

(a) $Oh = 0.001$ (b) $Oh = 0.01$ (c) $Oh = 0.1$

Figure 4.18: *Recoiling filaments with (a) $Oh = 0.001$, (b) $Oh = 0.01$, (c) $Oh = 0.1$. The profiles arise from numerical simulations by Notz & Basaran (2004) and correspond to figures 18-20 of their article [8]. The figures are examined through image analysis to provide a measurement of the travelling capillary ripples' wavelength, λ.*

Finally, all the validation results are collapsed in a single plot, i.e. figure 4.19. The diagram shows a good quantitative agreement with our asymptotic model.

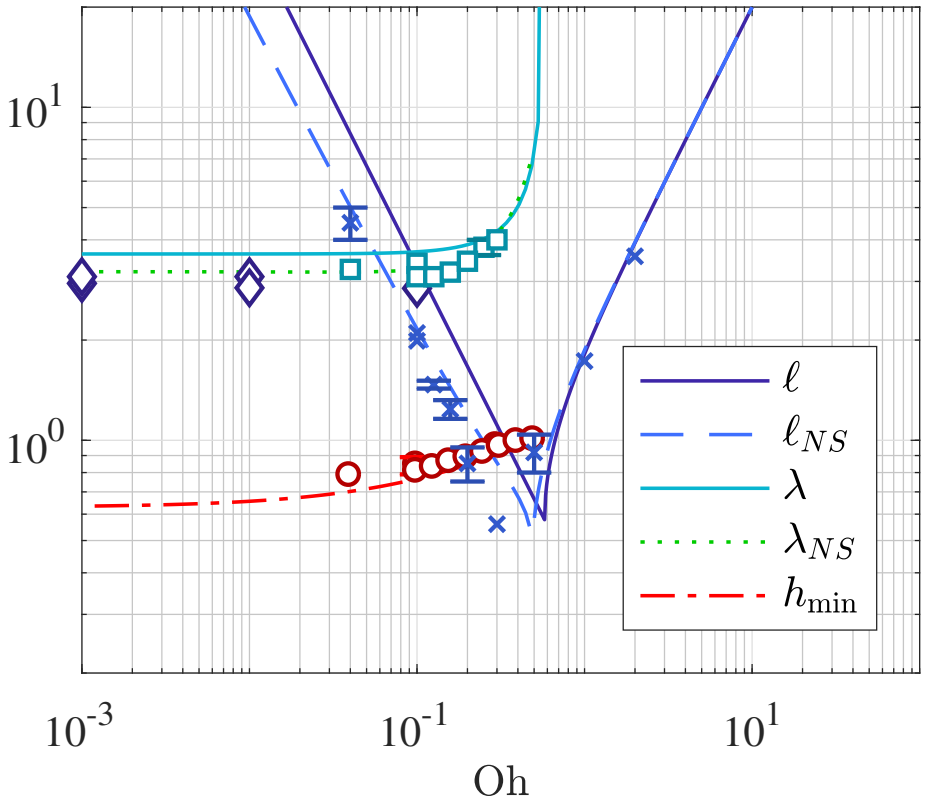

Figure 4.19: *Wavelength λ, decay length ℓ, and neck thickness $h_{\min}$ of the asymptotic solutions of lubrication equations as functions of the Ohnesorge number Oh (solid lines). Additionally, the wavelength and decay length obtained from linearisation of full Navier-Stokes equations are shown as dashed lines. Numerical results are shown for comparison: wavelengths from Notz & Basaran (2004) [8] ($\diamond$) and Basilisk [15] ($\square$), decay lengths from Basilisk ($\times$), and neck thickness from Basilisk ($\circ$). Error bars are not shown where these are smaller than the symbol size.*

4.6 Conclusions

In this chapter, we have derived a first-order asymptotic expansion for a semi-infinite Newtonian liquid filament recoiling by the action of surface tension. Our analysis identifies three distinct regions with different characteristic length and time scales: a steady filament section, an expanding spherical blob, and an intermediate *matching* zone.

Importantly, we have shown that, below a critical Ohnesorge number, $Oh^* \approx 0.577$, capillary waves naturally emerge along the surface of the filament and a neck is formed behind the blob. We have analysed the asymptotic wavelength of the capillary ripples, the spatial decay length along the filament, and the neck thickness as functions of the Ohnesorge number Oh. We analytically prove that, at the inviscid limit, the wavelength of the capillary waves is approximately 3.6 times the filament's radius. Our findings are found to be in agreement with numerical results obtained through the flow solver Basilisk [15] and those corresponding to the seminal work of Notz & Basaran [8].

Although the present work provides only a leading-order solution for the filament profile, higher-order corrections for the local filament radius and the velocity and pressure fields can be calculated too, following the scheme presented by Gordillo *et al.* (2011) [74] for a 2D fluid sheet and the slender cylindrical flow model of Eggers & Dupont (1994) [73]. Finally, we point out that obtaining such a quasi-analytical solution for an axisymmetric body opens the way to a full 3D linear stability analysis of recoiling liquid filaments, since an accurate base-state shape can now be considered.

Chapter 5

Overall conclusions and further work

5.1 Summary of contributions

In this thesis, we have investigated the dynamics of capillary retracting liquid filaments through a comprehensive approach involving experimental, analytical and numerical modeling. The main results are summarised in this section.

First, we have developed a method to practically produce free axisymmetric liquid filaments using a continuous liquid-jet system driven by a liquid pump (chapter 2). The experimental rig consists of a cylindrical chamber from which the fluid is jetted through a nozzle. The chamber is mechanically coupled with an electromagnetic actuator through an elastic membrane. An oscillating pressure modulation controlled by a function generator induces Rayleigh-Plateau instability on the jet surface, leading to the breakup into a train of droplets: filaments are formed between them. By controlling the liquid properties and the modulation parameters, desired symmetric filaments can be obtained. Their capillary retraction is then analysed through a high-speed imaging system.

Secondly, we have detected and analysed a transitional regime in the $Oh - \Gamma$ diagram for quasi-inviscid retracting filaments (chapter 3). Our results show that the breakup/no-breakup border in the phase diagram is not net as classically proposed in the literature. In this critical regime, the filament fates alternate and their behaviors are more complex than the state-of-the-art theories based only on the end-pinching mechanism. Here, we developed a wave-interaction model that effectively describes these complex behaviors. Our numerical and theoretical models are validated against experiments.

The last major achievement of this thesis is the analytical solution for the

profile of a Newtonian recoiling filament (chapter 4). Our derivation is based on a lubrication approximation and is performed through a local asymptotic analysis of a long-time steady regime. We show that the retraction domain is composed of three distinct regions with different characteristic length and time scales: a growing spherical blob, a steady cylindrical region and an intermediate matching zone. Our analytical model proves that, below a critical Ohnesorge number, the filament interface features travelling capillary waves escaping the blob at the Taylor-Culick speed and a neck connecting the steady region with the expanding spherical rim. The waves' asymptotic wavelength, the spatial decay length behind the blob, and the neck size have been analysed in terms of the Ohnesorge number. Our results have been validated against the full 3D linearised Navier-Stokes equations, numerical simulations performed by the flow solver Basilisk, and previous studies from the literature, obtaining a good agreement. This achievement is extremely important as it provides a full and formal picture of the surface tension-driven retraction of liquids, going beyond the classic Taylor-Culick analysis based on global mass and momentum conservation that yields a constant retraction speed.

5.2 Further work

Despite our achievements, the field of liquid jets is still extremely open and offers many ideas in terms of future work to be developed.

From the experimental perspective, we have come across many open questions: how can we define the dependence of the liquid jet instability on the electrical modulation? What is the correlation between the modulation parameters and the pinch-off dynamics? How can we characterize and control waveforms to obtain the desired breakup conditions (i.e. simultaneous and symmetric pinch-off at both ends of the droplets) and optimize the droplets/filaments production? How is the breakup length related to the modulation electrical signal? About the latter, previous experimental studies have shown a particular trend called "reversal": although theories predict the breakup length to decrease monotonically with the modulation amplitude, it shows a minimum stationary point and oscillations. It would be interesting to deeply and formally analyse the underlying physics in order to build a robust and reliable model. This can be corroborated and validated against a parametric study arising from experimental data.

The capillary wave superposition model presented in chapter 3 has some limitations that can be improved. First, it applies the principle of linear superposition to finite-amplitude waves (not complying mass conservation) to explain the non-linear dynamics of breakup. Though this criterion is effective in predicting the filament fate, it does not accurately reproduce the physics of the

phenomenon. Furthermore, the present model neglects the effect of the initial shape of the filament for providing just a qualitative comparison of the retraction dynamics between experiments and numerical simulations. However, the necking and the wave generation processes are certainly affected by the filament initial shape. Thus, a quantitative study on this effect would be necessary. Moreover, our model cannot predict the wave-amplitudes oscillation in time by itself. Finally, it is limited to low-viscosity liquids: it would be interesting to test its capabilities on viscous and/or non-Newtonian fluids. In summary, the task to be tackled in the future would be to make the capillary wave superposition model more accurate, complete, and self-contained.

The asymptotic analysis presented in chapter 4 provides with many interesting goals to be achieved in the fundamental perspective. First of all, the obtained analytic expansion for the recoiling filament profile opens the way to a complete 3D stability analysis of the solution in space and time. Additionally, it is remarkable that the long-time asymptotic quasi-steady solution obtained through our model does not include the filament breakup, which occurs in nature through capillary instability in a transient regime. It would be interesting to analytically investigate the connection to the pinch-off dynamics including the time-dependence of the solution. Furthermore, the capillary retraction of liquid filaments can be studied through an energy approach. During the retraction, the fluid surface energy is not fully converted into the kinetic form: part of it is dissipated through "capillary radiation". The energy radiated by the travelling waves acts as an actual drag, braking the receding blob. The next goal would be to calculate the further orders of the solution provided by our asymptotic model. This would allow to quantify the velocity correction with respect to the classic Taylor-Culick retraction speed and estimate the energy dissipation rate due to the capillary ripples.

Finally, we point out that the whole work presented in this thesis is focused on Newtonian liquids. In contrast, the majority of fluids found in nature and used in industrial, medical or biological applications include viscoelastic materials, granular flows, colloids, surfactant solutions, polymers, mixtures. Consequently, extending our study to fluids characterized by a more complex rheology would be a fundamental step forward in terms of practical and commercial interests.

Bibliography

[1] F Wang, FP Contò, N Naz, JR Castrejón-Pita, AA Castrejón-Pita, CG Bailey, W Wang, JJ Feng, and Y Sui. A fate-alternating transitional regime in contracting liquid filaments. *Journal of Fluid Mechanics*, 860:640–653, 2019.

[2] Francesco Paolo Contò, Fan Wang, José Rafael Castrejón-Pita, Yi Sui, and Alfonso Arturo Castrejón-Pita. A fate-alternating transitional regime in contracting liquid filaments. *Bulletin of the American Physical Society*, 2018.

[3] Francesco Paolo Contò, Juan F. Marín, Arnaud Antkowiak, J. Rafael Castrejón Pita, and Leonardo Gordillo. Shape of a recoiling liquid filament, 2019.

[4] Jens Eggers and Emmanuel Villermaux. Physics of liquid jets. *Reports on progress in physics*, 71(3):036601, 2008.

[5] Graham D Martin, Stephen D Hoath, and Ian M Hutchings. Inkjet printing-the physics of manipulating liquid jets and drops. In *Journal of Physics: Conference Series*, volume 105, page 012001. IOP Publishing, 2008.

[6] Kye Si Kwon, Lisong Yang, Graham D Martin, Rafael Castrejón-Garcia, Alfonso A Castrejón-Pita, and J Rafael Castrejón-Pita. Visualization and measurement. *Fundamentals of Inkjet Printing: The Science of Inkjet and Droplets*, 2015.

[7] Alfonso A Castrejón-Pita, JR Castrejon-Pita, and IM Hutchings. Breakup of liquid filaments. *Physical review letters*, 108(7):074506, 2012.

[8] Patrick K Notz and Osman A Basaran. Dynamics and breakup of a contracting liquid filament. *Journal of Fluid Mechanics*, 512:223–256, 2004.

[9] RMSM Schulkes. The contraction of liquid filaments. *Journal of Fluid Mechanics*, 309:277–300, 1996.

[10] Jérôme Hoepffner and Gounséti Paré. Recoil of a liquid filament: escape from pinch-off through creation of a vortex ring. *Journal of Fluid Mechanics*, 734:183, 2013.

[11] Stéphane Popinet. Gerris: a tree-based adaptive solver for the incompressible euler equations in complex geometries. *Journal of Computational Physics*, 190(2):572–600, 2003.

[12] Stéphane Popinet. An accurate adaptive solver for surface-tension-driven interfacial flows. *Journal of Computational Physics*, 228(16):5838–5866, 2009.

[13] Nikos Savva and John WM Bush. Viscous sheet retraction. *Journal of Fluid Mechanics*, 626:211–240, 2009.

[14] Michael P Brenner and Denis Gueyffier. On the bursting of viscous films. *Physics of Fluids*, 11(3):737–739, 1999.

[15] Basilisk flow solver. `http://basilisk.fr`.

[16] James Rayford Nix and Wladyslaw J Swiatecki. Studies in the liquid-drop theory of nuclear fission. *Nuclear Physics*, 71(1):1–94, 1965.

[17] James Rayford Nix. Further studies in the liquid-drop theory on nuclear fission. *Nuclear Physics A*, 130(2):241–292, 1969.

[18] Michael B Eisen and Patrick O Brown. [12] dna arrays for analysis of gene expression. In *Methods in enzymology*, volume 303, pages 179–205. Elsevier, 1999.

[19] Catherine Rivet, Hyewon Lee, Alison Hirsch, Sharon Hamilton, and Hang Lu. Microfluidics for medical diagnostics and biosensors. *Chemical Engineering Science*, 66(7):1490–1507, 2011.

[20] CGL Furmidge. Studies at phase interfaces. i. the sliding of liquid drops on solid surfaces and a theory for spray retention. *Journal of colloid science*, 17(4):309–324, 1962.

[21] Donald J Hayes, David B Wallace, Donald J Verlee, and Kenneth R Houseman. Apparatus and process for reagent fluid dispensing and printing, October 31 1989. US Patent 4,877,745.

[22] Donald J Hayes, David B Wallace, and Christopher J Frederickson. Method and apparatus for making miniaturized diagnostic arrays, August 19 1997. US Patent 5,658,802.

[23] Anselm Sickinger and Johannes Konrad Balmer. Automated pipetting of small volumes, June 9 1998. US Patent 5,763,278.

[24] Heather M Shewan and Jason R Stokes. Review of techniques to manufacture micro-hydrogel particles for the food industry and their applications. *Journal of Food Engineering*, 119(4):781–792, 2013.

[25] Shin-Hyun Kim, Jin Woong Kim, Jun-Cheol Cho, and David A Weitz. Double-emulsion drops with ultra-thin shells for capsule templates. *Lab on a Chip*, 11(18):3162–3166, 2011.

[26] Osman A Basaran. Small-scale free surface flows with breakup: Drop formation and emerging applications. *AIChE Journal*, 48(9):1842–1848, 2002.

[27] L Da Vinci. 1508 the notebooks of leonardo da vinci ed and transl. *E MacCurdy (New York: George Brazillier) p*, 756.

[28] Edme Mariotte. *Traité du mouvement des eaux et des autres corps fluides*. C.-Jombert, 1718.

[29] Thomas Young. An essay on the cohesion of fluids. *Philosophical Transactions of the Royal Society of London*, 95:65–87, 1805.

[30] Pierre Simon marquis de Laplace. *Traité de mécanique céleste*, volume 4. Crapelet, 1825.

[31] F Savart. Treatise on constitution of the liquid flow jetted out through orifice of thin plate. In *Annales de Chimie*, volume 53, pages 337–386, 1833.

[32] Lord Rayleigh. On the instability of jets. *Proceedings of the London mathematical society*, 1(1):4–13, 1878.

[33] Lord Rayleigh. On the capillary phenomena of jets. *Proc. R. Soc. London*, 29(196-199):71–97, 1879.

[34] Lord Rayleigh. Xvi. on the instability of a cylinder of viscous liquid under capillary force. *The London, Edinburgh, and Dublin Philosophical Magazine and Journal of Science*, 34(207):145–154, 1892.

[35] J Plateau. In *Annual Review of Physical Chemistry*, volume 80, page 566, 1850.

[36] G Magnus. In *Annual Review of Physical Chemistry*, volume 106, page 1, 1859.

[37] P Lenard. In *Annual Review of Physical Chemistry*, volume 30, page 209, 1887.

[38] Jens Eggers. Universal pinching of 3d axisymmetric free-surface flow. *Phys. Rev. Lett.*, 71:3458–3460, Nov 1993.

[39] Jens Eggers and Marco Antonio Fontelos. *Singularities: formation, structure, and propagation*, volume 53. Cambridge University Press, 2015.

[40] Jens Eggers. Nonlinear dynamics and breakup of free-surface flows. *Rev. Mod. Phys.*, 69:865–930, Jul 1997.

[41] JR Castrejon-Pita, NF Morrison, OG Harlen, GD Martin, and IM Hutchings. Experiments and lagrangian simulations on the formation of droplets in continuous mode. *Physical Review E*, 83(1):016301, 2011.

[42] JR Castrejón-Pita, GD Martin, SD Hoath, and IM Hutchings. A simple large-scale droplet generator for studies of inkjet printing. *Review of Scientific Instruments*, 79(7):075108, 2008.

[43] FJ García, H González, JR Castrejón-Pita, and AA Castrejón-Pita. The breakup length of harmonically stimulated capillary jets. *Applied Physics Letters*, 105(9):094104, 2014.

[44] Geoffrey Ingram Taylor. The dynamics of thin sheets of fluid. iii. disintegration of fluid sheets. *Proceedings of the Royal Society of London. Series A. Mathematical and Physical Sciences*, 253(1274):313–321, 1959.

[45] FEC Culick. Comments on a ruptured soap film. *Journal of applied physics*, 31(6):1128–1129, 1960.

[46] SD Hoath, S Jung, and IM Hutchings. A simple criterion for filament breakup in drop-on-demand inkjet printing. *Physics of Fluids*, 25(2):021701, 2013.

[47] Joseph B Keller. Breaking of liquid films and threads. *The Physics of fluids*, 26(12):3451–3453, 1983.

[48] Howard A Stone, BJ Bentley, and LG Leal. An experimental study of transient effects in the breakup of viscous drops. *Journal of Fluid Mechanics*, 173:131–158, 1986.

[49] Howard A Stone and L Gary Leal. Relaxation and breakup of an initially extended drop in an otherwise quiescent fluid. *Journal of Fluid Mechanics*, 198:399–427, 1989.

[50] José Rafael Castrejón-Pita, Alfonso Arturo Castrejón-Pita, Sumeet Suresh Thete, Krishnaraj Sambath, Ian M Hutchings, John Hinch, John R Lister, and Osman A Basaran. Plethora of transitions during breakup of liquid filaments. *Proceedings of the National Academy of Sciences*, 112(15):4582–4587, 2015.

[51] Theo Driessen, Roger Jeurissen, Herman Wijshoff, Federico Toschi, and Detlef Lohse. Stability of viscous long liquid filaments. *Physics of fluids*, 25(6):062109, 2013.

[52] Joseph Plateau. *Statique expérimentale et théorique des liquides soumis aux seules forces moléculaires*, volume 2. Gauthier-Villars, 1873.

[53] Constantin Weber. Zum zerfall eines flüssigkeitsstrahles. *ZAMM-Journal of Applied Mathematics and Mechanics/Zeitschrift für Angewandte Mathematik und Mechanik*, 11(2):136–154, 1931.

[54] Albert Y Tong and Zhaoyuan Wang. Relaxation dynamics of a free elongated liquid ligament. *Physics of fluids*, 19(9):092101, 2007.

[55] Jong-Wook Ha and L Gary Leal. An experimental study of drop deformation and breakup in extensional flow at high capillary number. *Physics of fluids*, 13(6):1568–1576, 2001.

[56] Julien Beaucourt, Thierry Biben, Anne Leyrat, and Claude Verdier. Modeling breakup and relaxation of newtonian droplets using the advected phase-field approach. *Physical Review E*, 75(2):021405, 2007.

[57] Mark Sussman, Ann S Almgren, John B Bell, Phillip Colella, Louis H Howell, and Michael L Welcome. An adaptive level set approach for incompressible two-phase flows. *J. Comput. Phys.*, 148(1):81–124, January 1999.

[58] Giovanni Russo and Peter Smereka. A remark on computing distance functions. *Journal of Computational Physics*, 163(1):51–67, 2000.

[59] Peter DM Spelt. A level-set approach for simulations of flows with multiple moving contact lines with hysteresis. *Journal of Computational Physics*, 207(2):389–404, 2005.

[60] Hang Ding and Peter DM Spelt. Inertial effects in droplet spreading: a comparison between diffuse-interface and level-set simulations. *Journal of fluid mechanics*, 576:287–296, 2007.

[61] Yi Sui and Peter DM Spelt. Validation and modification of asymptotic analysis of slow and rapid droplet spreading by numerical simulation. *Journal of Fluid Mechanics*, 715:283–313, 2013.

[62] Yi Sui and Peter DM Spelt. Non-isothermal droplet spreading/dewetting and its reversal. *Journal of Fluid Mechanics*, 776:74–95, 2015.

[63] Xu-Dong Liu, Stanley Osher, and Tony Chan. Weighted essentially non-oscillatory schemes. *Journal of computational physics*, 115(1):200–212, 1994.

[64] Hang Ding, Peter DM Spelt, and Chang Shu. Diffuse interface model for incompressible two-phase flows with large density ratios. *Journal of Computational Physics*, 226(2):2078–2095, 2007.

[65] Alvin U Chen, Patrick K Notz, and Osman A Basaran. Computational and experimental analysis of pinch-off and scaling. *Physical review letters*, 88(17):174501, 2002.

[66] Wim van Hoeve, Stephan Gekle, Jacco H Snoeijer, Michel Versluis, Michael P Brenner, and Detlef Lohse. Breakup of diminutive rayleigh jets. *Physics of fluids*, 22(12):122003, 2010.

[67] Richard F. Day, E. John Hinch, and John R. Lister. Self-similar capillary pinchoff of an inviscid fluid. *Phys. Rev. Lett.*, 80:704–707, Jan 1998.

[68] Museok Song and Grétar Tryggvason. The formation of thick borders on an initially stationary fluid sheet. *Physics of Fluids*, 11(9):2487–2493, 1999.

[69] Joseph B Keller, Andrew King, and Lu Ting. Blob formation. *Physics of Fluids*, 7(1):226–228, 1995.

[70] Joseph B Keller and Michael J Miksis. Surface tension driven flows. *SIAM Journal on Applied Mathematics*, 43(2):268–277, 1983.

[71] Asimina Sierou and John R Lister. Self-similar recoil of inviscid drops. *Physics of Fluids*, 16(5):1379–1394, 2004.

[72] Hui Ding, EQ Li, FH Zhang, Yi Sui, Peter DM Spelt, and Sigurdur T Thoroddsen. Propagation of capillary waves and ejection of small droplets in rapid droplet spreading. *Journal of Fluid Mechanics*, 697:92–114, 2012.

[73] Jens Eggers and Todd F Dupont. Drop formation in a one-dimensional approximation of the navier–stokes equation. *Journal of fluid mechanics*, 262:205–221, 1994.

[74] Leonardo Gordillo, Gilou Agbaglah, Laurent Duchemin, and Christophe Josserand. Asymptotic behavior of a retracting two-dimensional fluid sheet. *Physics of Fluids*, 23(12):122101, 2011.

[75] Stephane Popinet and Arnaud Antkowiak. Lecture notes breakup of cylindrical jets singularities and self-similar solutions. 2011.

[76] Manfredo P Do Carmo. *Differential Geometry of Curves and Surfaces: Revised and Updated Second Edition*. Courier Dover Publications, 2016.

[77] Subrahmanyan Chandrasekhar. *Hydrodynamic and hydromagnetic stability*. Courier Corporation, 2013.

[78] L Pekker. On plateau-rayleigh instability of a cylinder of viscous liquid. *Journal of Imaging Science and Technology*, 62(4):40405–1, 2018.

[79] Thomas Erneux and Stephen H Davis. Nonlinear rupture of free films. *Physics of Fluids A: Fluid Dynamics*, 5(5):1117–1122, 1993.

[80] Gilou Agbaglah, Sébastien Delaux, Daniel Fuster, Jérôme Hoepffner, Christophe Josserand, Stéphane Popinet, Pascal Ray, Ruben Scardovelli, and Stéphane Zaleski. Parallel simulation of multiphase flows using octree adaptivity and the volume-of-fluid method. *Comptes Rendus Mecanique*, 339(2-3):194–207, 2011.